NiCuAg: An Electrocatalyst for Sustainable Transformations

Hannah Louise Alexandra Dickinson

Submitted in fulfilment of the requirements for the
Degree of Doctor of Philosophy

School of Chemistry

College of Science and Engineering

JULY 2024

To Rory, Jean, Patricia, and Brian,

"What you do makes a difference, and you have to decide what kind of difference you want to make."

- Dr Jane Goodall

Abstract

Climate change is the biggest global threat facing this generation. Atmospheric CO_2 levels have reached around 400 ppm which has led to increased global temperatures and rising sea levels, changes which affect not only human but also animal and plant life. Electrochemistry can be implemented as a useful technology to help combat this. Electrochemical CO_2 reduction aims to convert the excess atmospheric CO_2 into useful feedstock chemicals such as hydrocarbon fuels. Electrochemical hydrogen evolution aims to provide an alternative means of producing hydrogen that does emit CO_2, as well as allowing the storage of excess energy generated by existing renewable energy technologies. This thesis examines the development of metallic stacked catalysts for these sustainable transformations.

Chapter 1 provides context and a literature review of the recent developments in the field of bimetallic and trimetallic catalysts for electrochemical CO_2 reduction. The multiple simultaneous reaction pathways and resulting linear scaling relations are outlined; the current popular ways these can be overcome by catalyst modification are also given. The definitions of a series of common performance metrics are reported. Following this, the context and pioneering research developments for hydrogen evolution catalysts are discussed including the role of pH, possible mechanisms, and the development of activity volcano plots. In Chapter 2 the theory behind the experimental and analytical techniques used throughout this thesis are explained.

The development of a trimetallic catalyst, NiCuAg is detailed in Chapter 3. NiCuAg, NiCu and bare Ni are successfully synthesised, thoroughly characterised and tested under CO_2 reduction conditions. Chapter 4 takes forward the catalysts developed in Chapter 3 and explores their use as hydrogen evolution catalysts, at a variety of pH values. It also explores the development of NiCuPt, and NiPt, which expand upon the catalyst layering idea whilst introducing Pt, which is known for its hydrogen evolution ability.

Contents

List of Tables

List of Figures

Acknowledgements

I would firstly like to thank my supervisor, Professor Mark Symes for his help and guidance at every stage of the PhD process. From my initial application, through to project discussions, conference abstracts, paper drafts, and of course, many thesis edits, Mark has been able to offer invaluable knowledge, advice, and support. His continued confidence in me, even when mine was low has truly inspired me. Mark, I hope you continue to take big swings for big wins, and of course, maintain the fight against useless TLAs.

It goes without saying that none of this work would have been possible without the knowledge and technical support of the Joseph Black Building staff. Karen and Finlay at stores, thank you for being the glue that holds this place together. Andy, Claire, Jim, John, and Chris, thank you for all your training, support and maintenance of the various analytical equipment. A special thanks also goes to Kayla and her team in the KNC for their help with everything TEM related.

My appreciation also goes out to the Symes group as a whole. In particular at the beginning of my PhD, Calum, Thanasis, and Paddy who welcomed me despite it being the end stages of a pandemic; and towards the end, Zeliha, Fiona, and Shaun, who I'm sure were continually distracted by my reading out random thesis sections and discussions of sentence structure and grammar. Your friendship, and diverse skills have made this experience vastly more enjoyable.

I cannot forget to mention my flatmate for the majority of my time in Glasgow, Nick. I'm so grateful for our tea and gossiping sessions. Recharging over a cuppa whilst sharing the drama from our respective workplaces, and cooking dinner together was such a comfort to look forward to after a rough day in the lab.

Having moved to Glasgow in the midst of the pandemic, I will be forever thankful for the 2022 Burns Night Ceilidh, and the friends and fellow PhD students it allowed me to finally meet. Ross and Katy, thank you so much for inviting me into your group, and all the activities, quizzes and laughter that came along with it, oh and of course, for pushing Henry to dance with me.

Henry, thank you for your never ending encouragement, love, and confidence in me. You have truly made this experience easier being by my side.

Finally, I would like to thank my family for their love and support on my academic journey. Thank you for tolerating my moves further and further away from you, hopefully the next place will provide equally fun weekends away. Thank you for always being just a phone call away.

Declaration

I declare that, except where explicit reference is made to the contribution of others, this dissertation is the result of my own work and has not been submitted for any other degree at the University of Glasgow or any other institution

---

Hannah Louise Alexandra Dickinson

Abbreviations

BET - Brunauer-Emmett-Teller

CV - Cyclic Voltammogram

DFT - Density Functional Theory

DMSO - Dimethyl sulfoxide

ECSA - Electrochemically Active Surface Area

EDX - Energy Dispersive X-ray

EELS - Electron Energy Loss Spectroscopy

EXAFS - Extended X-ray Absorption Fine Structure

FE_x - Faradaic Efficiency for x

FID - Free Induction Decay

GC - Gas Chromatograph

GEMS - Geoanalytical Electron Microscopy and Spectroscopy

HAADF - High Angle Annular Dark Field

HER - Hydrogen Evolution Reaction

IPCC - Intergovernmental Panel on Climate Change

KNC - Kelvin Nanocharacterisation Centre

LSV - Linear Sweep Voltammetry

NGN - N-doped graphene

NHE - Normal Hydrogen Electrode

NIST - National Institute of Standards and Technology

NMR - Nuclear Magnetic Resonance

NOAA - National Oceanic and Atmospheric Administration

NW - Nanowires

OER - Oxygen Evolution Reaction

RHE - Reversible Hydrogen Electrode

SCE - Saturated Calomel Electrode

SEM - Scanning Electron Microscopy

SHE - Standard Hydrogen Electrode

STEM - Scanning Transmission Electron Microscopy

TCD - Thermal Conductivity Detector

TEM - Transmission Electron Microscopy

TOF - Turnover Frequency

UHR-SEM - Ultra High Resolution Scanning Electron Microscopy

XPS - X-ray Photoelectron Spectroscopy

XRD - X-ray Diffraction

ΔG^0 - Gibbs Free Energy Change

η - Overpotential

Chapter 1

Introduction

Includes work published as "Recent Progress in CO_2 Reduction Using Bimetallic Electrodes Containing Copper" H. L. A. Dickinson, M. D. Symes, Electrochemistry Communications, 2022, 135, 107212.

Abstract

Rising levels of carbon dioxide in the atmosphere and the increasing threat of the effects of climate change have precipitated considerable research efforts aimed at generating energy from renewable sources, such that consuming this energy does not lead to further increases in atmospheric CO_2. Simultaneously, atmospheric CO_2 and water represent useful feedstocks for the storage of renewably-generated energy. For CO_2 through electroreduction powered by renewables to give hydrocarbon fuels that when burned do not increase net CO_2 levels in the atmosphere; and for hydrogen through electrochemical water splitting as a means of storage to combat the intermittence of currently available renewable energies.

In order to bring such renewable-powered production of hydrocarbons from CO_2 to reality, improved electrocatalysts for carbon dioxide reduction are required. For example, Cu is the only single metal that demonstrates appreciable Faradaic efficiency for CO_2 reduction products that are reduced by more than two-electrons, but pure Cu is not an especially active or selective catalyst for this process. Hence there has been considerable interest in making bimetallic catalysts using Cu in combination with other metals in order to find systems that can reduce CO_2 to products such as methane, methanol, ethanol and beyond.

In this chapter, an overview of electrochemical CO_2 reduction and its performance metrics is presented alongside a review of the recent progress in CO_2 electroreduction catalysts using bimetallic and trimetallic cathodes composed of copper and various other metals in combination; a particular focus is given to studies which achieved reduction beyond two-electrons. The theory behind hydrogen evolution and its analysis is also discussed in conjunction with the examination of a series of pioneering catalyst discoveries.

1.1 Introduction

1.1.1 The Climate Crisis

Climate change, driven by increasing demand for energy worldwide and the subsequent increase in greenhouse gas emissions, maintains its place as one of society's biggest challenges.[1,2] As can be seen in Figure 1.1, the amount of CO_2 in the atmosphere have risen exponentially since the end of the industrial revolution (c. 1840). CO_2 levels remained stagnant at 280 ppm for hundreds of years before beginning to rise to the current yearly average of 419 ppm for 2023.[3] Supplementary to this increase in CO_2 there has been a change in atmospheric composition which is further reflected in rising sea levels, changes to the pH of sea water, and the rise of global temperatures. Thus it is not only human life, but plant and animal biodiversity which will be affected.

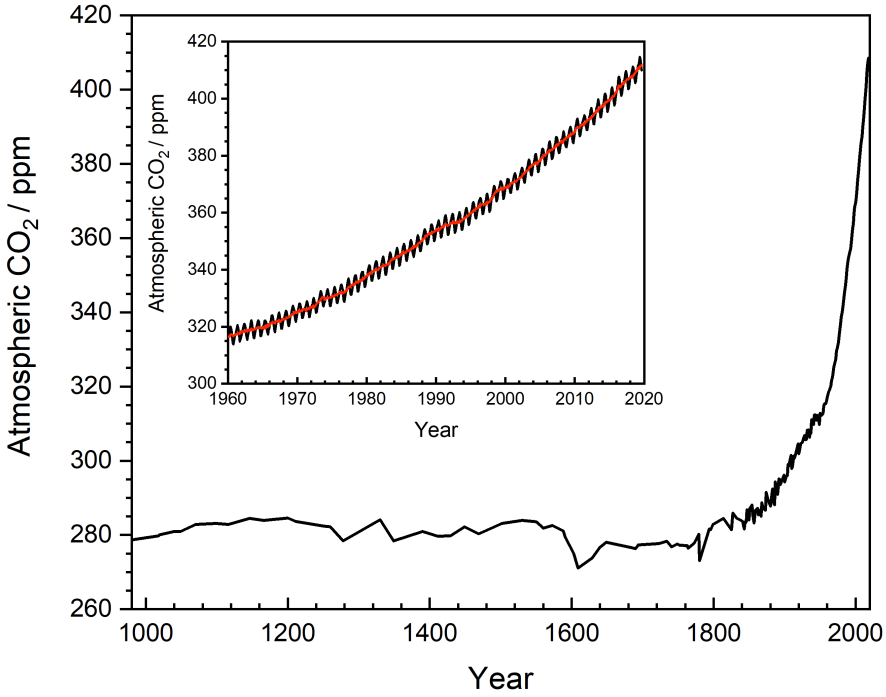

Figure 1.1: CO_2 emissions between 1000 and 2020, the inset shows the data between 1960 and 2020 in more detail. The black line (source data) shows monthly average carbon dioxide at NOAA's Mauna Loa Observatory on Hawai'i. The red line shows the annual trend.[4]

In recognition of the need for climate action, 196 parties agreed to the terms of the United Nations Paris Agreement.[5] Officially implemented from 4 November 2016, the parties agreed that climate change is a global threat and aimed to "limit the temperature increase to 1.5 °C above pre-industrial levels". Signatories strive to achieve this by re-balancing CO_2 emissions and consumption within the first half of this century. Despite this policy, the Intergovernmental Panel on Climate Change (IPCC), found that a global temperature increase of 1.5–2 °C is inevitable in the near term (2021–2040).[1] The IPCC modelled CO_2 emissions and found that at the current rate CO_2 levels would exceed 450 ppm in 2030 and could reach between 750 and 1300 ppm by 2100, without further intervention. As a consequence of this increase, global temperatures would rise significantly, thus to achieve a temperature increase of less than 2 °C compared to pre-industrial levels, atmospheric CO_2 cannot surpass 450 ppm.[1]

1.1.2 Strategies to Decrease CO_2 Emissions

Most current strategies to reduce carbon dioxide emissions fall into one of three categories: carbon sequestration, decarbonisation, or carbon recycling. Carbon sequestration is the capture and storage of CO_2. Sequestration is beneficial in that gigatonnes of CO_2 can be removed from the atmosphere, nonetheless storing carbon dioxide has no monetary value therefore without incentives it is not an economically viable technique.[6] Decarbonisation is the removal of carbon from energy production, or other CO_2 emitting processes. It focuses on the implementation of renewable energy sources such as wind, solar, and hydrogen power, however, it is not possible for all processes to be supplied by renewables. Transportation, for example, relies on liquid fuels and it is highly advantageous for it to remain that way.[7] Despite this, it is certain that decarbonising our current energy supply needs to be a key component of climate change mitigation, whilst carbon sequestration will likely play a smaller part.

Carbon recycling is the generation of more valuable carbon products from waste CO_2. Electrochemical CO_2 reduction has been put forward as a viable technique to produce desirable hydrocarbon fuels (for example, as a means of storing renewably-generated power) which can be consumed without increasing the overall amount of CO_2 in the atmosphere, as part of a closed carbon cycle.[8] Due to the increasingly pressing nature of climate change and the negative effects that come along with it, this has made CO_2 reduction a key research area, which has been exponentially gaining interest since the late 1990s.[9]

1.1.3 Electrochemical CO_2 Reduction

Electrochemical CO_2 reduction is a promising technique as it (1) often only requires ambient temperatures and pressures, (2) has the potential to be incorporated into existing renewable energy systems, and (3) the desired products can (in theory) be selected by changing parameters such as the applied potential and electrolyte.[10] Carbon can be electrochemically reduced from its most oxidised form, +4, in carbon dioxide, to a number of products, Equation 1.1.

$$x\mathrm{CO_2} + y\mathrm{H^+} + y\mathrm{e^-} \longrightarrow \mathrm{C}_x\mathrm{H}_y\mathrm{O}_z + n\mathrm{H_2O} \tag{1.1}$$

The chemically inert, linear CO_2 molecule has two very strong C=O double bonds (~750 kJ mol^{-1}) which would usually require harsh conditions such as high temperature or pressure to be broken. Yet, under electrochemical conditions high energy protons and electrons are able to break these bonds and reduce the carbon centre. A variety of products can be produced using electrochemical CO_2 reduction, some of which are listed in Table 1.1. The hydrogen evolution reaction (HER) is also shown, since this process is in constant competition with CO_2 reduction when protons are available. In a characteristic electrochemical CO_2 reduction cell, an aqueous electrolyte is used, thus water is often the proton

source. CO_2 is reduced at the cathode, the exact product selectivity and combination is determined by the nature of the electrocatalyst, and the oxygen evolution reaction (OER) normally occurs at the anode. Typically an inert material such as platinum or graphite is used as the anode.

Table 1.1: Standard electrochemical CO_2 and proton reduction potentials at 25 °C and 1 atm.[11]

Reaction	**E^0/ V vs. RHE**
$CO_2 + e^- \longrightarrow CO_2^{\bullet -}$	−1.48
$CO_2 + 2H^+ + 2e^- \longrightarrow CO + H_2O$	−0.10
$CO_2 + 2H^+ + 2e^- \longrightarrow HCOOH$	−0.19
$CO_2 + 4H^+ + 4e^- \longrightarrow HCHO + H_2O$	−0.06
$CO_2 + 6H^+ + 6e^- \longrightarrow CH_3OH + H_2O$	+0.03
$CO_2 + 8H^+ + 8e^- \longrightarrow CH_4 + 2H_2O$	+0.17
$2CO_2 + 12H^+ + 12e^- \longrightarrow C_2H_5OH + 3H_2O$	+0.09
$2CO_2 + 12H^+ + 12e^- \longrightarrow C_2H_4 + 4H_2O$	+0.08
$2CO_2 + 14H^+ + 14e^- \longrightarrow C_2H_6 + 4H_2O$	+0.14
$3CO_2 + 18H^+ + 18e^- \longrightarrow C_3H_7OH + 5H_2O$	+0.11
$2H^+ + 2e^- \longrightarrow H_2$	0.00

Despite the apparent advantages of electrochemical CO_2 reduction many obstacles still exist including the low solubility of CO_2 in aqueous electrolyte solutions at acidic/neutral pH. Current cathode materials also tend to produce a mixture of products rather than targeting a single species, and can deactivate quickly, making them industrially ineffective.

Single electron transfer to CO_2 produces an unfavourable anion radical, $CO_2^{\bullet -}$. This reaction is both thermodynamically and kinetically unfavourable due to the large re-arrangement of bonds required, from linear (180°) to a bent (138°) configuration.[12] The electrochemical potential of the single electron reduction is −1.48 V vs. RHE, however when a proton transfer occurs concurrently with the electron transfer, the electrochemical potential can be lowered. This co-movement of electrons and protons is termed a proton-coupled-electron transfer and allows high energy intermediates to be avoided.[13] In accordance with $\Delta G = -nFE^0$, reactions with a more positive E^0 are more thermodynamically favourable; thus in a purely thermodynamic sense reductions to C_{2+} products and

alcohols are more favourable, however, there is a large kinetic barrier to these reactions, with proton dissolution being a major contributor.[10] It has therefore been suggested that the ideal cathode material for C_{2+} products contains both electron and proton transfer sites.

Many categories of electrocatalysts for carbon dioxide reduction have been studied including: pure metals,[14] metal oxides,[15] metal–ligand complexes[16] and graphitic carbon nitrides.[17] The presence of catalytically-active d-electrons and/or vacant orbitals of transition metals can allow the absorption and desorption of CO_2 and its products; metals are often chosen based on their binding strength towards a given reaction intermediate. In a series of seminal papers by Hori *et al.* metals were separated into three groups based on their reduction products, Figure 1.2.[18–20]

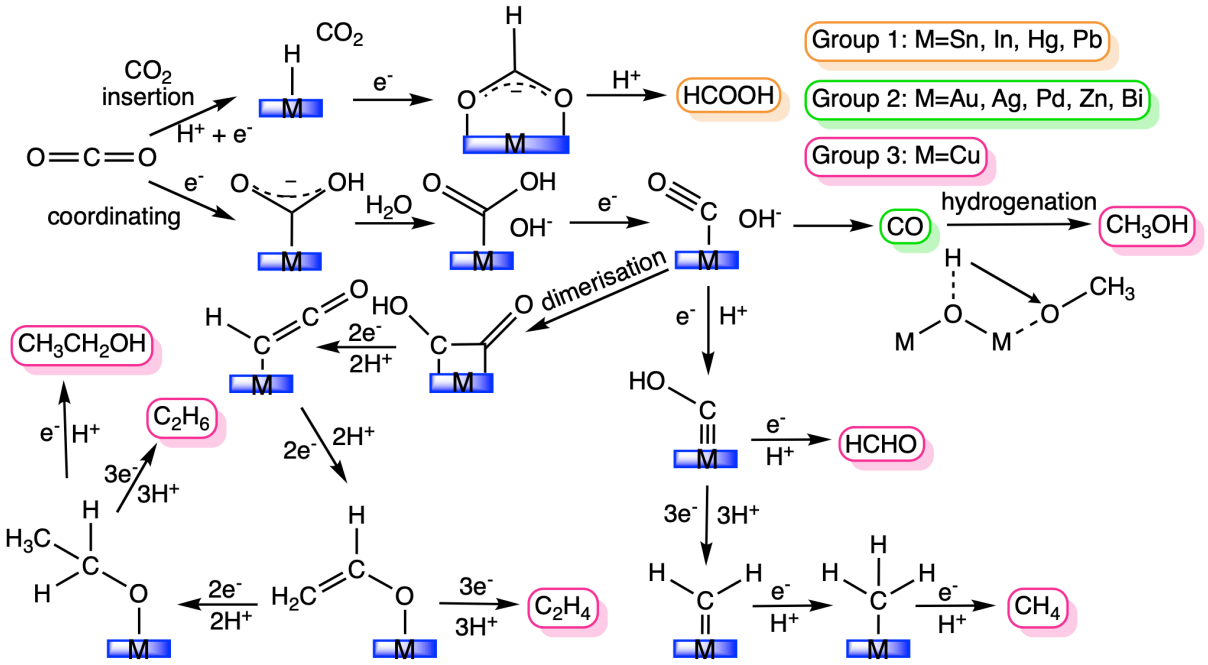

Figure 1.2: Schematic of some of the possible CO_2 reduction pathways on various pure metal electrodes.

The first group (Sn, In, Cd) does not bind $CO_2^{\bullet-}$ well, thus the radical anion is desorbed and proton transfer occurs predominantly producing $HCOO^-$. Metals which do coordinate $CO_2^{\bullet-}$, including Au and Ag, form the second group, producing CO as the major product. The *COOH intermediate (an asterisk indicates an adsorbed species) is bound more tightly on these metals so further electron and proton transfers can occur on the metal

surface, however their binding strength for *CO intermediates is much weaker, leading to the release of carbon monoxide as product. The final group only contains Cu since it can bind *CO intermediates strongly enough for further electron and proton transfers to occur, as well as dimerisation leading to C_{2+} products. Pure Cu is effectively a "Goldilocks" catalyst, it has a binding strength for *CO that is strong enough to allow further reaction but not so strong that active sites are essentially blocked. This agrees with the Sabatier principle which stipulates that optimum catalysts have intermediate adsorbate-catalyst bond strengths.[21]

CO_2 reduction proceeds via multiple, simultaneous pathways, where all the reaction intermediates relate to each other in an approximately linear fashion.[22] Since many reaction intermediates bind via the same central atom (C or O) decreasing the binding energy for one intermediate, decreases it for all those that bind through the same central atom.[23] This relation controls the activity for a given catalyst, the improvement in activity affects all reaction pathways thus the selectivity towards an individual product cannot be easily increased. To be selective for a single product these scaling relations must be broken; several methods have been put forward in an attempt to break these scaling relations, some of which are listed here:

- *Promoters*, can change adsorbate binding strengths through electronic and structural effects such as induced fields or geometric distribution.[22]
- *Tethering*, combines homogeneous and heterogeneous catalysis by tethering a ligand to the electrode material, thus only the target intermediate reacts with the ligand and is reduced further, while other intermediates are not, thus only a specific pathway is active.[24]
- *Ligand stabilisation*, can be used in homogeneous approaches so that only particular intermediates have the correct geometry to react further. The complex formed lowers the energy of certain intermediates relative to others breaking the scaling relation.[22]

- *Alloying*, can be be used in heterogeneous catalysis to tune the chemical environment adjacent to the particular binding sites. For example, if a metal with high oxygen affinity is used the stability of CHO* would be increased relative to CO*, allowing for more favourable C−O bond cleavage. Whilst the addition of metals with a high hydrogen affinity would aid proton transfer.[25]

Alongside breaking the scaling relations and moderating the production of hydrogen (and other less valuable carbon-containing products in favour of hydrocarbons), a number of other factors limit CO_2 reduction. Mass transfer of CO_2 to the cathode surface is often limited due to the low solubility of CO_2. This can be overcome by using a gas diffusion electrode, which generates a three-phase interface[21] so that CO_2 can directly interact with the electrode material. Thermodynamic and kinetic limitations, such as a minimum required cell voltage often depend on cell design.[26] It is important to note that developing an ideal electrocatalyst for hydrocarbons is only one hurdle, cell design, electrolyte choice and the anodic, oxygen evolution reaction, will also need to be optimised before CO_2 reduction is industrially viable. Often in electrochemistry these factors affect one another, therefore it is crucial that methodologies are rigorously described and standardised performance metrics are used. Some reactions benefit from being described by certain metrics, for example the Tafel slope is commonly reported for hydrogen evolution catalysts.

1.1.4 Electrochemical Performance Metrics

The following parameters are typically used when evaluating an electrocatalyst for CO_2 reduction or hydrogen evolution, it is important that they are reported so that appropriate comparisons can be made between different materials. It is worth noting that these parameters can not only depend on the electrocatalyst material but also factors such as, the electrolyte used, the reaction temperature, and the reaction cell type. Therefore, all cell parameters and reaction conditions should be reported alongside these metrics.

1.1.4.1 Current Density

The current density conveys the current normalised by the geometric area, or occasionally the mass, of an electrode. It is arguably more appropriate to normalise by the electrochemical surface are of the catalyst used, however this is often hard to measure. The current density indicates the rate of an electrochemical reaction, reflecting its performance; thus, it is an essential parameter to report.

1.1.4.2 Electrochemically Active Surface Area (ECSA)

The electrochemical surface area is particularly important for nanostructured materials, such as those with channels or pores, in these cases the ECSA would be significantly higher than the geometric area, thus the current density calculated with the geometric area would be an overestimate. The ECSA can be calculated using equation 1.2, where C_{DL} is the double layer capacitance, and C_S is the specific capacitance.[27]

$$\mathrm{ECSA} = \frac{C_{DL}}{C_S} \tag{1.2}$$

1.1.4.3 Overpotential and Onset Potential

Overpotential, η, is defined as the potential difference between the ideal, thermodynamically derived reduction potential of a reaction and the potential at which the reaction occurs experimentally, at a given current density. The experimentally observed potential at which the current density reaches $(-)1$ mA cm^{-2} is often termed the onset potential. For both hydrogen evolution and CO_2 reduction the onset potential will always be more

negative than the standard potential, thus the overpotential can be thought of as an activation energy, providing the energy for electrons to move through the solution to the electrode, for example. The best electrocatalysts will be able to lower this overpotential decreasing the amount of external energy required.

1.1.4.4 Tafel Analysis

Current density, i and overpotential, η can be related using the Tafel equation:

$$\eta = a + b\, log_{10}[\mathrm{i}] \tag{1.3}$$

Hence, a plot of the overpotential against the logarithm of the current density can be constructed. The Tafel slope, b, of the linear portion of the graph can then be used to determine the number of electrons transferred in the reaction, and to find the rate determining step.[28] Tafel slope analysis is only valid in systems under certain circumstances; the system must have no mass transport limitations and operate under Butler-Volmer kinetics. The best electrocatalysts for hydrogen evolution have a low Tafel slope value. More information on how the Tafel slope is derived and can be used to determine the reaction mechanism can be found in section 1.5.2.

1.1.4.5 Turnover Frequency (TOF)

Turnover frequency refers to the rate of an electrochemical reaction per active site, at a given potential. It is often used to compare different electrocatalysts as it describes the intrinsic activity regardless of the structure or geometric coating of the material.[29] However, TOF is typically very hard to calculate, as the true nature of the active sites are often unknown.

1.1.4.6 Faradaic Efficiency

Faradaic efficiency, FE_x expresses the selectivity for a particular product from a electrochemical reaction; it is calculated using equation 1.4, where a is the number of transferred electrons, n is the number of moles of desired product, x, F is Faraday's constant, and Q_{total} is the total charge passed.[28]

$$FE_x = \frac{a \times n \times F}{Q_{total}} \times 100 \tag{1.4}$$

1.1.4.7 Stability

Although not always easy to quantify numerically, it is important that the stability of an electrocatalyst is evaluated and recorded. There is no practical use for a 98% selective catalyst that degrades after one hour of usage. Electrocatalysts appropriate for industrial applications require sufficiently long-term stability to balance out their running and manufacture costs. Stability can be measured through repeated testing via cyclic voltammetry, or potentiostatic polarisation; understanding the degradation process of an electrocatalyst can also be informative for further optimisation.[29]

1.2 Modification of Electrocatalysts

The most effective catalysts for CO_2 reduction will be highly selective towards a single multi-carbon product at a low overpotential. They will also be stable over long periods of time and multiple catalytic cycles. Since this often isn't the case for most pure metals, a variety of methods for their improvement, and the development of other types of catalysts quickly followed Hori's initial discovery.

In 1991, Watanabe published an investigation into Cu–M alloys where M = Ag, Cd, Ni, Pb, Sn and Zn; this was the first reported study into alloys for electrochemical CO_2 reduction.[30] The most noteworthy alloy was that of copper and nickel (Cu/Ni 90:10), which suppressed CO production in favour of methanol at a peak Faradaic efficiency of 7% at −0.9 V vs. SHE. These results indicated a synergistic effect between Cu and Ni. This deviation from linear scaling relations has since been recognised as a combination of two effects: the electronic effect, which modifies the binding environment for intermediates, and the geometric effect, which changes the arrangement of the atoms at the active site.[31]

Consequently, a large variety of metals have been combined and investigated, whether in a multi-phase or alloyed arrangement, to elucidate a selective electrocatalyst for CO_2 reduction. There is currently particular focus on Cu–M bimetallics due to the unique ability of pure Cu to produce hydrocarbons. Generally, the selectivity of Cu–M alloys is modified by varying the nature of M. Although this is simple in theory, results can be mixed, especially since catalyst composition and metal arrangement both affect which reaction pathway dominates. This complexity continues to fascinate and tantalise many researchers. The use of copper and copper-based bimetallic catalysts for carbon dioxide electroreduction was reviewed by Su, Hwang and co-workers in 2018,[32] by Zhao *et al.* at the start of 2020,[11] and by Xiao and Zhang[33] and Fontecave and co-workers[34] specifically for CO_2 reduction to C_2 products. However, considerable progress in the field continues to be made. In this chapter, some papers in this area, that have emerged in the last four years will be reviewed. Even focusing on such recent works, it is impossible to be comprehensive hence the in-depth discussions will focus on reports of Cu-based catalysts, where carbon-based products that are more deeply reduced than two-electrons were obtained in significant Faradaic yield. A selection of recent, pertinent bimetallic and trimetallic catalysts, Cu-based or otherwise, can be found in Table 1.2.

Table 1.2: Summary of recently reported bimetallic and trimetallic catalysts for electrochemical CO_2 reduction

Electrode	**Synthesis Technique**	**Morphology**	**Electrolyte**	**Potential/ V_{RHE}**	**Carbon product(s)**	**FE/ %**	**Ref.**
Cu – Ag	Physical vapour deposition	Pyramid textured	0.2 M $KHCO_3$	−1.1	Methane	62	2021[35]
$Cu_{2.5}$ – Ag_1	Electrophoresis deposition of nanoparticles	Nanoparticles	0.1 M $KHCO_3$	−0.8	Methane (C_2 products)	20.6 (15.7)	2021[36]
Cu_9Ag_1	Galvanic replacement of Cu NWs	Nanowires	0.1 M $KHCO_3$	−1.17	Methane	72	2021[37]
$Cu(Ag\text{-}20)_{20}$	Dropcasted Cu_2O nanowires and Ag powder	Composite Cu and Ag powder	0.1 M $KHCO_3$	−1.1	Ethanol	16.5	2020[38]
3Au:1Cu	Modified Brust method	Nanoparticles	0.1 M $NaHCO_3$	−0.7	Formate	16	2021[39]

Continued on the next page

$AuCu_3$@Au	Oxidative etching of $Au_{20}Cu_{80}$	3D bicontinuous nanoporous structure	0.1 M $KHCO_3$	−0.6	CO	97.27	2020[40]
$CuAu_3$	Electro-deposition	Nanowire array	0.1 M $KHCO_3$	−0.5	Ethanol	48	2019[41]
Bi Cu	Co-electrodeposition	Tight moss-like micro-structure	0.5 M KOH / 0.5 M $KHCO_3$	−0.91	Formate	94.37	2021[42]
Cu Bi	Electro-deposition	Dendritic	0.5 M $KHCO_3$	−1.0	Formate	94.7± 2.8	2021[43]
Bi_3Cu_1	Green-cleaning method	Irregular granular fragments	0.5 M $KHCO_3$ (0.5 M KOH)	−0.75 (−0.81)	Formate	95.1 (95.75)	2022[44]
Cu-Co (14 % Co)	Electro-deposition	Small grain aggregates	0.1 M $KHCO_3$	−1.19	Methane	47.7	2019[45]

Continued on the next page

Cu-In	Electro-deposition	Dendritic	0.1 M $KHCO_3$	−0.85	Formate	87.4	2020[46]
CuIn/C	Co-reduction	Nanoparticles	0.1 M $KHCO_3$	−0.7	Syngas ratios change based on phase/structure	H_2= 39.8 CO= 24.3	2021[47]
$In_{1.5}Cu_{0.5}$	In-situ growth method	Nanoparticles	0.1 M $KHCO_3$	−1.2	Formate	90	2021[48]
Ni-Cu NW (0.82 % Ni)	Galvanic replacement of Cu NWs	Nanowires	0.1 M KOH	−0.77 (−0.97) [−0.88]	C_2H_5OH (C_2H_4) [C_{2+} products]	16 (24) [62]	2021[49]
Cu Ni (19 at.% Ni)	Oxide derived	Nanoparticles	0.05 M $KHCO_3$	−1.2	C_2 products	35	2020[50]
CuPd(100)	Thermal reduction treatment and in situ growth	Nanoparticles	0.1 M $KHCO_3$	−1.4	C_2 products	50.3 ±1.2	2021[51]

Continued on the next page

nd-PdCu-1 (70 % Pd, 30 % Cu)	Low-temp solution method	Nanodendrites	0.1 M $KHCO_3$	−0.3	Formate	99.4	2021[52]
$Cu_{50}Pd_{50}$	Co-precipitation	Nanosheets	1.0 M KOH	−0.65	CO	71 ± 3	2022[53]
Sn/Cu	Lithography, electroplating of Cu film, and electroless Sn coating	Cones	0.1 M $KHCO_3$	−0.6	CO	82.7	2021[54]
$Cu_{6.26}Sn_5$	Electrodeposition	Dendritic rice spike-like	0.1 M $KHCO_3$	−1.08	Formate	97.8 ± 2.4	2021[55]
Cu_1Sn_3	Co-electrodeposition	Triangular microblocks form a groove-protrusion structure	0.5 M $KHCO_3$	−0.8	Formate	91.38	2021[56]

Continued on the next page

Cu_3Sn (Cu_6Sn_5)	Hydrogen bubble template method, then electroreduction (Electro-deposition)	Dentritic	0.1 M $KHCO_3$	−1.0	Ethanol (Formate)	64 (60)	2022[57]
$CuZn_{20}$/NGN	Co-precipitation	Nanoparticles	0.1 M $KHCO_3$	−0.8	Ethanol (multi-carbon products)	34.25 (50.14)	2021[58]
Zn-Cu	Galvanic replacement	Cu nanoparticles on Zn foil	0.1 M $KHCO_3$	−0.96	CO	97	2021[59]
Cu-Zn	Atomic layer deposition	Phase separated nanowires	0.1 M $KHCO_3$	−1.0	CO	94	2022[60]

Continued on the next page

M−Cu M=Cd, {Sb, Pb, Zn}	Galvanic replacement reaction on sub-μm diameter copper rods	Nanofibers	0.5 M $NaHCO_3$	−1.05	Formate	70.5 {48.9, 58.7, 48.6}	2019[61]
$Zn_{0.87}Ag_{0.13}$	Electro-deposition then drop cast	Nanodendrite layer	1 M $KHCO_3$	−1.25 V_{NHE}	CO	98.0	2022[62]
$Zn/Ag_{0.18}$	Galvanic replacement	Nanosheets	1 M $KHCO_3$	−1.0	CO	∼70	2021[63]
AuNi	Atom-polymer hybridization	Nanoparticles	0.1 M $KHCO_3$	−0.98	CO	92	2021[64]
Ni_3Sn_4	Hydrothermal synthesis	Nanoparticles	0.1 M $KHCO_3$	−0.9	Formate	85.1 ±1.5	2021[65]

Continued on the next page

$Sn_{50}Pb_{50}$	Cathodic disintegration	Irregular shaped particles	0.5 M H_2SO_4 Anolyte, 0.5 M $KHCO_3$ Catholyte	-2.44 V_{SHE}	Formate	64	2020[66]
Sn_{95}-Co_5/Cu foam	Electro-deposition	Snow-like particles on foam	0.5 M $NaHCO_3$	−1.36	Formate	72.2	2020[67]
AuCuIn	Electrochemical deposition	Dense cauliflower-like spheres	0.5 M $KHCO_3$	−0.6	CO	91.4	2022[68]
$Au_1Ag_1Cu_5$	Multi-step seed mediated growth method	Asymmetric Nanostructures	0.1 M $KHCO_3$	−0.8	Ethanol	37.5	2022[69]

1.3 Bimetallic Electrodes Containing Cu

1.3.1 Copper-Silver Catalysts

In recent years, several Cu – Ag based mixed metal catalysts with high selectivity towards methane have been developed. Choi *et al.*[37] synthesised Cu – Ag interfaces on the surface of Cu nanowires. Silver was chosen as Cu and Ag are essentially immiscible, thus the catalyst would contain a mixture of Ag and Cu phases rather than an alloy phase. It was suggested that the creation and maximisation of these atomic Ag-Cu interfaces would benefit electrochemical CO_2 reduction towards products beyond CO. After synthesis of the nanowires by galvanic displacement, Figure 1.3, X-ray diffraction (XRD) confirmed that no alloyed CuAg phase was present and Energy Dispersive X-ray (EDX) mapping depicted a thin layer of Ag on the surface of the Cu nanowire. CO_2 reduction in a sealed H-cell revealed that the Cu_9Ag_1 catalyst displayed a Faradaic efficiency towards C_2H_4 of less than 21% across all potentials; however, the selectivity towards CH_4 was increased compared to pure Ag nanoparticles, which produced mainly CO, and pure Cu nanowires, whose highest reported Faradaic efficiencies were 55% ± 8% for CH_4 at -1.23 V_{RHE}, and 60% ± 4% for C_2H_4 at -1.06 V_{RHE}. Cu_9Ag_1 gave a maximum Faradaic efficiency for methane production of 72% at -1.17 V_{RHE}, decreasing to 66% ± 4% at -1.20 V_{RHE}. These are very high selectivities and Faradaic yields for methane; the next challenge would be to increase the relevant current densities (currently > 5 mA cm^{-2}) towards industrially relevant figures.

It is generally regarded that the reaction pathways towards CH_4 and C_2H_4 deviate after the formation of the *COH intermediate;[70] the addition of adsorbed hydrogen to this intermediate leads to CH_4 whilst coupling with CO leads the pathway towards C_2H_4, Figure 1.4. Preferential CO binding on Ag is confirmed by electrochemical CO_2 reduction

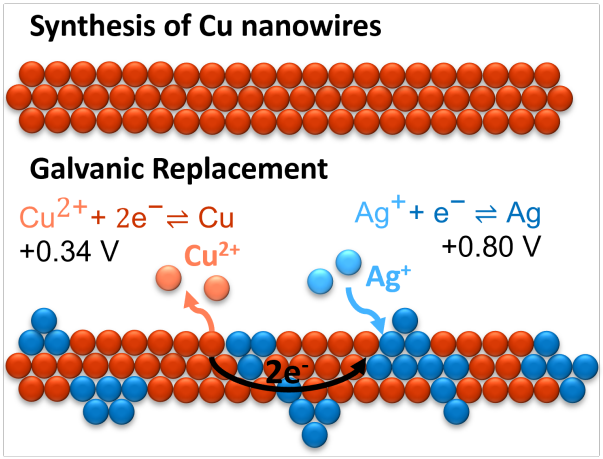

Figure 1.3: Schematic of the preparation of Cu–Ag nanowires by galvanic replacement, reproduced from[37] .

on Ag nanoparticles (Faradaic efficiency for CO >90% at all potentials). In contrast, Cu promotes high hydrogen coverage at voltages more negative than -0.8 V_{RHE}. Thus, a synergistic effect based on *CO at Ag sites and *H on Cu could lead to higher selectivity towards CH_4 production.

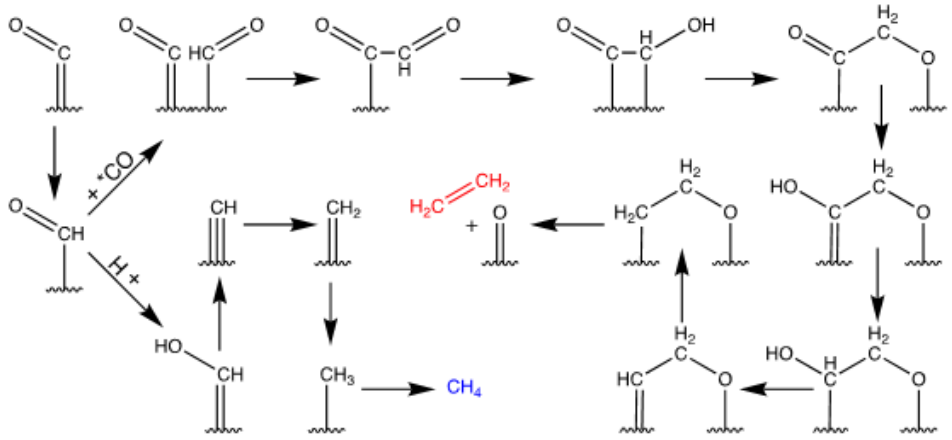

Figure 1.4: Schematic of the possible reaction pathways towards methane[70] and ethylene.[71]

Wu *et al.* exploited the immiscibility of Cu and Ag to develop mixed metal nanoparticles that were resistant to low-temperature catalyst sintering during electrochemical reduction.[36] As shown in Figure 1.5 nanostructured Cu electrocatalysts have poor stability and a decreased active surface area caused by a degradation phenomenon that is widely ascribed to the agglomeration or dissolution-redeposition of smaller nanoparticles into larger ones.[72]

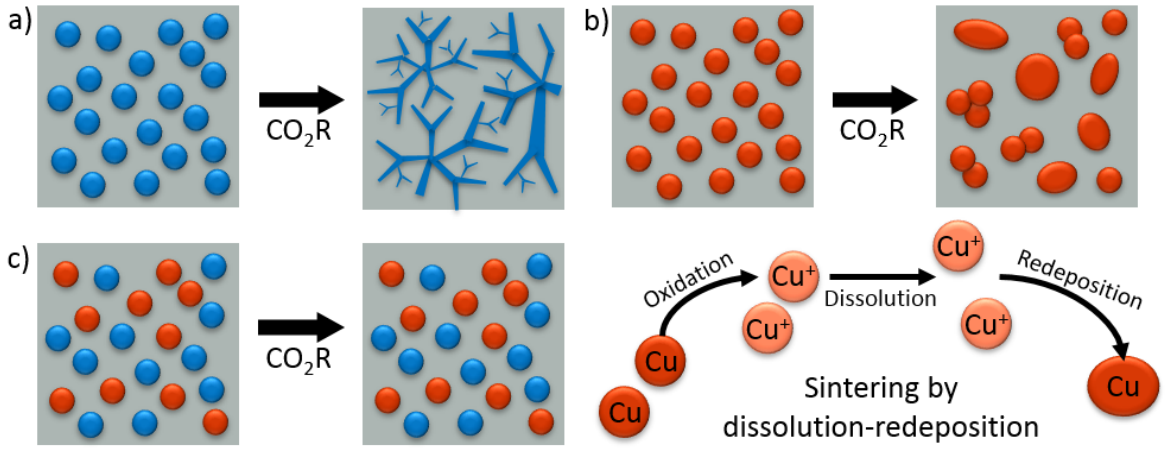

Figure 1.5: Schematic showing the structural changes that occur to a) Ag, b) Cu, and c) Ag – Cu nanoparticles under CO_2 reduction conditions. Figure adapted from[36] .

Mixed Cu – Ag nanoparticles were prepared using an electrophoretic deposition method. Following electroreduction at -0.8 V_{RHE} notable sintering was seen by Scanning Electron Microscope (SEM) imaging on the pure Cu nanoparticles, whereas upon the addition of Ag nanoparticles, sintering was significantly reduced. It was proposed that the immiscibility of the neighbouring Cu and Ag nanoparticles prevented dissolution and redeposition. Although sintering was reduced, electrochemical CO_2 reduction on $Cu_{2.5}$ – Ag_1 predominantly produced hydrogen. Initially, the highest Faradaic yield for a carbon-based product was 10.3 % at -0.8 V_{RHE} towards methane. However, after the synthesis of a series of more dense Cu – Ag catalysts, to further investigate the stabilisation caused by Ag, it was found that the selectivity of the nanoparticle electrodes could be easily adapted by shifting the Cu:Ag ratio. Dense $Cu_{2.5}$ – Ag_1 favoured methane production (FE_{CH4} 20.6 % at -0.8 V_{RHE}), whilst a Cu:Ag ratio of 1:1 produced an enhanced activity towards C_{2+} products (Faradaic efficiency of 15.7 % at -0.8 V_{RHE}), and Cu_1 – $Ag_{2.5}$ was the best ratio for CO production. Although these efficiencies are not the highest seen in recent years, the increased catalyst stability, due to being sinter-resistant, could prove vital for applications.

Ting *et al.*[38] achieved increased CO_2 reduction activity towards ethanol via a composite catalyst containing oxide-derived Cu nanowires and Ag particles. It was found that ethanol production increased with the amount of CO evolved from Ag sites. Thus, in excess *CO, Ag and Cu worked in tandem to access a reaction pathway towards ethanol at a Faradaic efficiency of 16.5 % at -1.1 V_{RHE}. This pathway utilised the coupling of *CO and *CH_x (x = 1, 2) at Cu–Ag boundaries which could then be reduced to ethanol.

1.3.2 Copper-Nickel Catalysts

Nickel is often considered to increase hydrogen evolution activity, binding *CO strongly and effectively poisoning the catalyst surface.[73] Furthermore, theoretical calculations have suggested that no advantage will be seen upon alloying Ni with Cu compared to the activity of pure Cu.[74] Despite this, it may be beneficial for an intermetallic catalyst to contain Ni as surface-bound or adjacent catalyst sites (which would agree with the results reported by Zhang *et al.*[49] – see below); it could provide the *H required for the production of C_{2+} products.

Oxide-derived Cu-Ni alloy nanoparticles were developed by Suzuki *et al.*[50] with an enhanced selectivity towards ethylene and ethanol. After the initial synthesis of the Cu–Ni nanoparticles it was found that a pre-electrolysis activation step was required for more desirable (non-CO and H_2) products to be favoured. Cu–Ni (19 at.% Ni) was found to show the best increase in the activity towards C_2 products, with a Faradaic yield for these species of 35 %. Subsequently, H_2 evolution was greatly decreased to a Faradaic efficiency of 9 %, compared to >80 % at 83 at.% Ni, the highest nickel content tested. Given the dramatic change in activity, the surface of the catalyst was examined by X-ray Photoelectron Spectroscopy (XPS), which found that a mixture of Cu, Ni, Cu–O and Ni–O phases were present. Suzuki *et al.* maintain that the mixture of these components could be intrinsic to the amplified activity.

Ni can become segregated within Cu–Ni alloys creating a nonuniform catalyst, thus Zhang *et al.*[49] developed a synthesis to deliberately create a highly dispersed Cu–Ni surface. Following their synthesis, Cu nanowires containing unsaturated sites were immersed in acetonitrile and $Ni(NO_3)_2$ for various time periods, 0.5–5 minutes. The introduction of nitrile ligands from acetonitrile lowered the reduction potential of Cu, allowing galvanic replacement by Ni to occur. CO_2 reduction was tested in a two-compartment H-cell using a CO_2-saturated 0.05 M $NaHCO_3$ solution as the electrolyte. CuNi (0.82 at.% Ni) produced the most significant results, displaying a Faradaic yield for hydrogen of only 17 % at -0.87 V_{RHE} and a Faradaic efficiency of 16 % for ethanol production at -0.77 V_{RHE}, whilst the highest efficiency for C_2H_4 was recorded as 24 % at -0.97 V_{RHE}. A volcano type relationship was observed when the amount of dispersed Ni was varied, Figure 1.6; a CuNi electrode with 0.13 at.% Ni displayed only slightly higher activity towards C_2 products than pure Cu nanowires, and a CuNi mixture with 1.3 at.% Ni mainly produced H_2 (with Faradaic yield $\geq$ 81 % at all potentials). Thus, the increased activity towards C_2 products was ascribed to the intrinsic catalytic properties facilitated by the presence of both Cu and Ni at specific ratios.

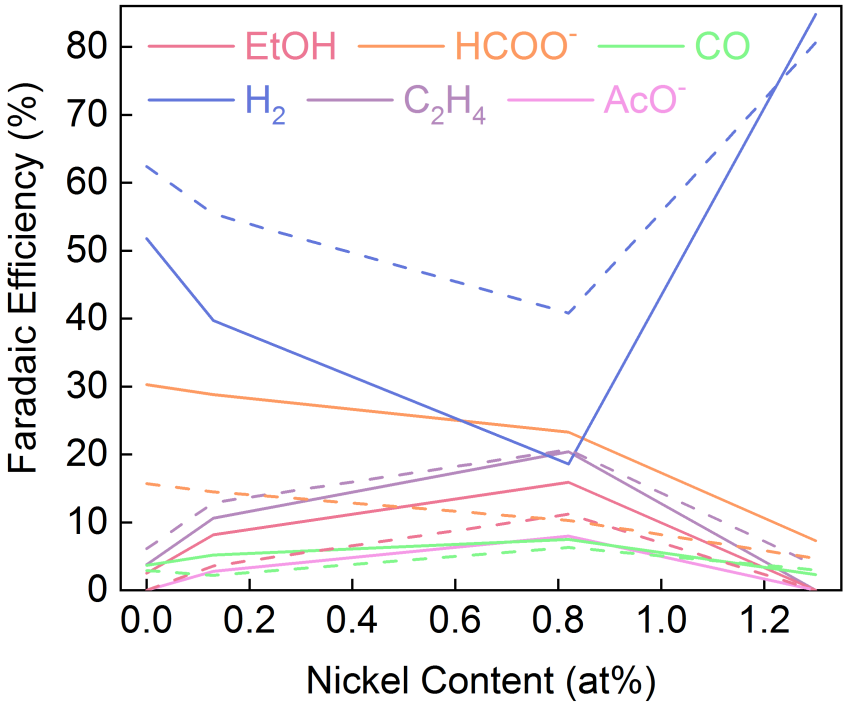

Figure 1.6: Faradaic Efficiency of Cu–Ni alloys with different Ni contents. The solid lines show the FE at -0.77 V_{RHE} and the dashed lines at -1.07 V_{RHE}. Data extracted and reproduced from[49] .

Further catalytic testing, in a flow-cell electrolyser in KOH electrolyte, allowed the activity of CuNi (0.82 at.% Ni) to be optimised, with a measured Faradaic efficiency towards C_{2+} products of 62 % at 0.88 V_{RHE}; similar increases in activity when using KOH in flow-cells have been reported before.[75] Whilst this CO_2 reduction activity is significant, further work is required to tune the selectivity towards specific C_2 products. DFT calculations were completed to learn more about the reaction pathways available on the CuNi catalyst. It was found that Ni decoration reduced the energy barriers for the first three reaction steps: the formation of $*CO_2$ from CO_2, $*CO_2$ to *COOH, and the subsequent *COOH to *CO step. The chemisorption of CO_2 was found to be the rate determining step. This work is significant in that it suggests that a bulk Cu−Ni alloy is not required in order to induce high activity for CO_2 reduction to C_{2+} products, but instead that decoration of only the surface is sufficient to endow the ability to perform such deep reductions.

1.3.3 Copper-Zinc Catalysts

Pure Zn has low HER activity, mainly producing CO, so it is expected that the combination of Cu and Zn will reduce levels of hydrogen evolution, in addition, ZnO is cheaper than the typical secondary metals that are combined with Cu for CO_2 electroreduction, thus costs are also reduced. The use of carbon-based supports has also been proposed to aid CO_2 adsorption and activation in CO_2 electroreduction.

Dongare *et al.*[58] used N-doped graphene as a catalyst support for ZnO and CuO-derived nanoparticles ($CuZn_x$/NGN). Catalysts with a Zn loading of less than 20 wt.% were evenly dispersed on the N-doped graphene; further Zn content led to agglomeration. Brunauer-Emmett-Teller (BET) analysis found the catalysts had a mesoporous structure which led to plentiful exposed active sites and high catalytic activity. Only liquid-phase product analysis was completed upon catalytic testing; the study focussed on the production of ethanol. On all catalysts, productivity towards ethanol increased with more negative potentials; $CuZn_{20}$/NGN showed the highest Faradaic yield for ethanol, 34 % at 0.8 V_{RHE}.

Dongare *et al.* suggested a mechanism towards ethanol on $CuZn_{20}$/NGN wherein CO is generated on Zn sites and passed on to neighbouring CuO sites for further reduction towards ethanol. It has been proposed that C – C coupling between hydrogenated C_1 species is more favourable than the combination of two *CO species.[76] Thus, a mechanism containing the coupling of $*CH_2$ with *CO was proposed, Figure 1.7. According to this mechanism, CO_2 is absorbed on Cu, Zn, and pyridinic-N sites, where proton-electron transfers occur to produce *CO. Then hydrogenation forms $*CH_2$ which can couple to the *COH generated at neighbouring sites to give $*CH_2COH$. A final hydrogenation step and release from the catalysis surface gives ethanol. However, this suggested mechanism does not reveal how each individual site, or the mixture of Cu and Zn sites is beneficial. Computational analysis based on this mechanism could be useful in this regard.

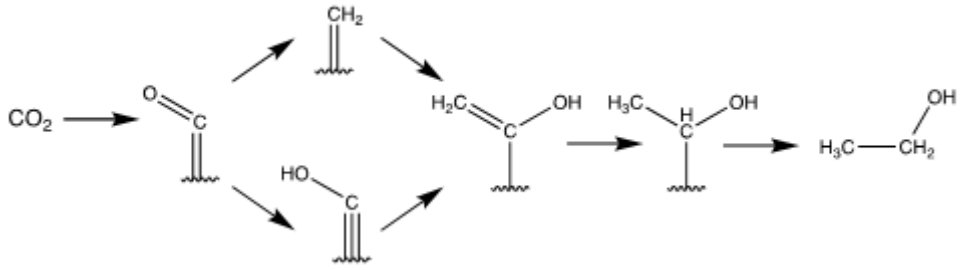

Figure 1.7: Schematic of the possible reaction pathway towards ethanol outlined by Dongare et al.

The activity difference between phase-separated and core-shell CuZn catalysts was investigated by Wan *et al.*[60] Interestingly, the differing structure distributions both produced high CO activity, however, the phase-separated sample exhibited a higher Faradaic efficiency of 94 % towards CO at -1.0 V_{RHE} compared to the core-shell sample (FE_{CO} = 82 % at -1.0 V_{RHE}). The stability of the phase-separated sample was also significant at beyond 15 hours.

DFT calculations were completed to probe the reasoning behind this difference in activity. It was found that for the pathway towards CO production, both structures gave the rate determining step as the formation of *COOH, a key intermediate in CO production. Thus enhanced *COOH adsorption would increase catalyst activity. After the adsorption of *COOH a difference in charge density was found between the different structures. Cu atoms showed an increased area of charge depletion, whilst Cu – C sites displayed charge accumulation indicating enhanced adsorption and a strong covalent bond. The adsorption free energy of *H on the core-shell catalyst was calculated to be lower than on the phase-separated CuZn, thus a higher HER activity on the core-shell structure could also contribute to its decreased desirable activity.

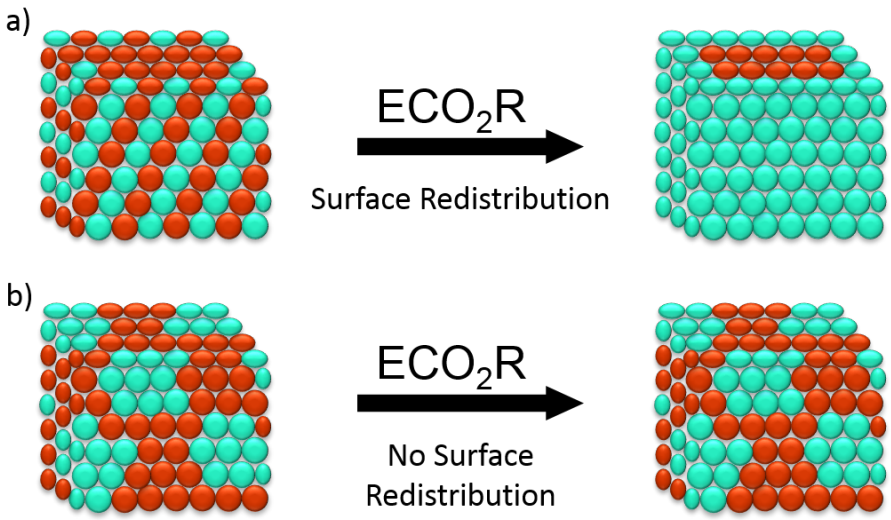

Figure 1.8: Schematic of surface redistribution for a) the core-shell (Cu/Cu – Zn) and b) the phase-separated CuZn sample, adapted from[60] . Cu (red), Zn (cyan).

After 20 minutes of electroreduction, morphology and elemental distribution analysis found that the core-shell catalyst experienced elemental redistribution, Figure 1.8. The Cu – Zn shell sites experience strain induced by *COOH adsorption; this creates a tension that pulls Zn out of the flat Cu – Zn mixture creating a reconstructed Zn layer on the surface. It is proposed that this precipitation of Zn leads to the instability of the core-shell CuZn catalyst, since no apparent change can be detected on the phase-separated sample. The Faradaic efficiency of the core-shell sample towards CO is approximately equivalent to that of 50 nm ZnO on carbon paper, therefore the redistribution of Zn removes any benefits observed due to the combination of Zn with Cu.

1.3.4 Copper-Tin Catalysts

The production of ethanol by electrochemical CO_2 reduction has been reported to be dependent on the surface coverage of *CO.[77] Entropy-based adsorption theory was first defined by Takeguchi[78] and states that random distributions within alloys can weaken *CO adsorption. Accordingly, a low entropy alloy would have increased *CO adsorption comparatively. Shang *et al.*[57] synthesised a low-entropy Cu−Sn catalyst with the aim to enhance *CO adsorption and favour ethanol production. Cu_3Sn was synthesised as a low entropy state and Cu_6Sn_5 as a high entropy comparison. Extended X-ray absorption fine structure (EXAFS) spectra displayed a lower amplitude signal for Cu_6Sn_5 indicating the presence of systemic chaos and therefore a higher entropy. Calculations using data from the Fourier-transform fitting of the EXAFS curves confirmed Cu_3Sn had a lower entropy (-5.961 J K^{-1} mol^{-1}) than Cu_6Sn_5 (-5.186 J K^{-1} mol^{-1}). All together this implies that *CO adsorption on Cu_3Sn will be enhanced which was then validated by temperature programmed CO desorption measurements.

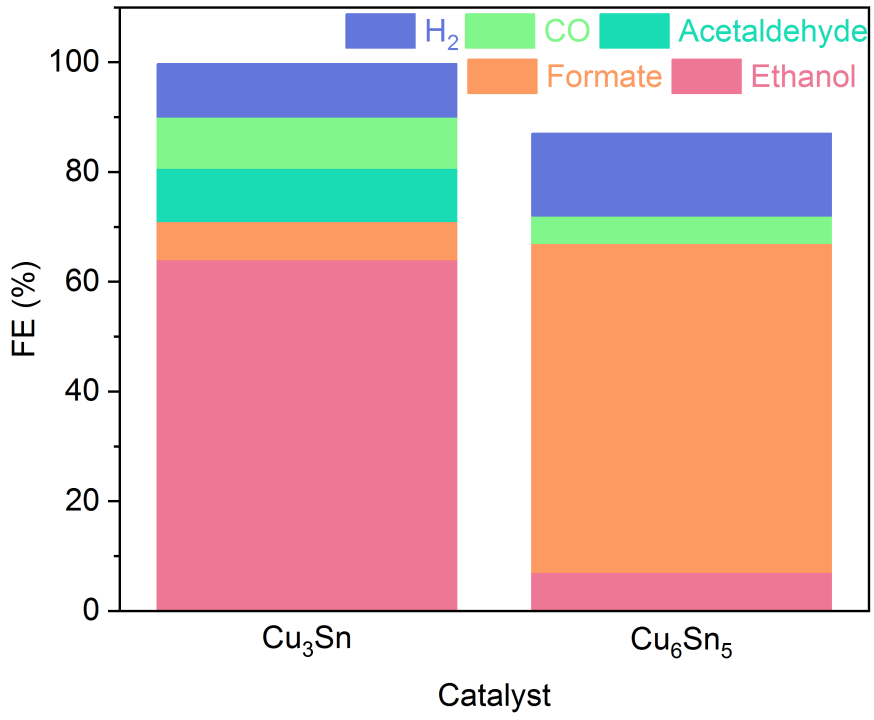

Figure 1.9: Faradaic efficiency of the main products of CO_2 reduction for Cu_3Sn compared to Cu_6Sn_5 at -1.0 V_{RHE} in 0.1 M $KHCO_3$. Data extracted and reproduced from[57] .

As can be seen in Figure 1.9, Cu_3Sn presented a much higher selectivity towards ethanol than Cu_6Sn_5 with a Faradaic efficiency of 64 % at -1.0 V_{RHE}. Cu_6Sn_5 displayed increased activity towards formate ($FE_{Formate}$ ≈60 % at at -1.0 V_{RHE}). Many complex pathways and intermediates can be found on Cu-based catalysts, therefore Shang *et al.* used DFT calculations to consider the binding energies of the key ethanol, formate, and CO intermediates. It was found that the energy difference between the ethanol intermediate (*CHCHOH) and that of ethylene (*CCH), which are thought to be in competition after dimerisation, on Cu_3Sn was 0.17 eV on Cu and 1.19 eV on Sn sites. This implies that the thermodynamically favourable pathway is towards ethanol on the low-entropy catalyst since *CHCHOH is stabilised. However, on Cu_6Sn_5 Cu sites favoured *CO and Sn sites *COOH thus, predominant CO and formate production is seen.

1.4 Trimetallic CO_2 Reduction Electrocatalysts

Trimetallic electrocatalysts for CO_2 reduction are beginning to gain traction; the addition of a third metal to an electrocatalyst alloy could further control the availability of active sites and target a specific reaction pathway and product. There are currently limited examples of published trimetallic catalysts despite the area of research having been suggested fairly often.

In 2013, Kyriacou *et al.*[79] developed a Cu−Sn−Pb electrode for the reduction of formic acid. They found that formic acid can be generated at Faradaic efficiencies close to 100 % on pure tin or lead electrodes, yet with their Cu−Sn−Pb catalyst the formic acid could be reduced to more valuable species such as methanol or ethanol. The reduction of formic acid using Cu(88)Sn(6)Pb(6) produced optimum current efficiencies for methanol, ethanol, and acetaldehyde at -0.8 V vs. Ag/AgCl, of 30.3 %, 37.6 %, and 17.1 %, respectively. Ethanol and acetaldehyde were shown, for the first time, to be products of formic acid reduction.

Berlinguette and colleagues[80] screened the compositional space of a Cu–Zn–Sn electrocatalyst. The catalyst was based on pre-existing alloys, such as bronze (Cu/Sn) and brass (Cu/Zn), and used earth-abundant metals only, to reduce cost. CO and HCOOH Faradaic efficiencies were measured across the compositional space at a potential of −0.7 V_{RHE}. The highest CO formation was seen for $Cu_{0.2}Zn_{0.4}Sn_{0.4}$, and it is presumed that a synergistic effect caused this, as the pure metals did not produce activities as high. The introduction of Sn appeared to suppress hydrogen evolution, and bimetallic alloys containing large amounts of Sn favoured HCOOH, in particular $Cu_{0.2}Sn_{0.8}$.

More recently, Zhu *et al.*[69] developed a AuAgCu heterostructure with the aim that the unique spatial arrangement would increase catalyst performance. A multi-step seed-mediated growth method was used, Figure 1.10, first Au nanobipyramids were synthesised and used as seeds for core encapsulation by Ag to give Au–Ag nanorods. A Cu overgrowth process then selectively deposited Cu on one side of the Au–Ag nanorods to form a AuAgCu nanostructure. CO_2 reduction testing in a H-type cell in CO_2-saturated 0.1 M $KHCO_3$ resulted in a Faradaic efficiency towards ethanol of 37.5 % at −0.8 V_{RHE}. Increasing the size of the distinct Cu domain, thought to be caused by the lattice mismatch between Ag and Cu, was found to increase activity towards ethanol, $Au_1Ag_1Cu_1$ did not produce ethanol at any potential measured, however the Faradaic efficiency previously mentioned was achieved by $Au_1Ag_1Cu_5$. Long term stability testing showed no significant changes to the current density produced after 18 hours.

Figure 1.10: Schematic of the synthesis of asymmetric Au (yellow)/Ag (blue)/Cu (red) nanostructures, adapted from[69] .

This enhanced C_2 product selectivity was assigned to the ability of Cu to promote C–C coupling and therefore the formation of C_2 products. Zhu proposed that since Au and Ag have lower O and H affinities than Cu, *CO binds relatively weakly and so is released once produced. This leads to an increased local concentration of CO which could spill over to

the Cu sites where C−C coupling can occur. The asymmetric spatial arrangement of the catalyst is crucial to this CO spill-over process. The tandem catalysis and electronic effects explored by Zhu are a promising development, proving that trimetallic catalysts could be developed further by controlling composition and morphology to enhance selectivity for desirable C_2 products.

Han *et al.* developed a trimetallic AuCuIn catalyst for CO_2 reduction to CO as a means to reduce cost.[68] Pure Au is a good catalyst for CO production as it favours *COOH binding, however, it is very expensive. AuCu was found to be the most common AuM alloy due to the synergistic binding effects resulting from its downshifted d-band center compared to pure Au. Han synthesised AuCu cathodes by electrodeposition on carbon paper. Dense cauliflower-like spheres were seen by field-emission SEM which produced a Faradaic efficiency towards CO of 80.7 % at -0.70 V_{RHE}. The effect of various third metals (AuCuM, M = Fe, Mo, In) was investigated by adding the appropriate metal salt to the deposition electrolyte. It was found that the addition of In increased the Faradaic efficiency towards CO and reduced the overpotential required, $FE_{CO} = 91.4$ % at -0.60 V_{RHE}. According to the results of a Tafel analysis, it was proposed that AuCuIn enables faster electron transfer than AuCu so $CO_2^{\bullet -}$ is better stabilised. The addition of In also suppresses the hydrogen evolution reaction, since its intrinsic Lewis acidity causes it to have limited reactivity with protons.

1.5 The Hydrogen Evolution Reaction

Since it's first reported discovery by Troostwijk and Deiman in 1789[81,82] the splitting of water by electrolysis into its constituent parts, oxygen and hydrogen, Equation 1.5, has become a key technology in the green energy transition.[83] The implementation of water electrolysis is thought to reduce worldwide reliance on fossil fuels and aid in the uptake of energy from renewable sources. As a result there appears to have been an increase in

sustainable government policies that promote renewable energy practises. Electrolysis can be employed to combat the intermittence of contemporary renewable energy sources; the hydrogen produced can serve not only as a means of energy storage, but also a fuel and clean hydrogen source for methanol and ammonia production.[84,85]

$$2H_2O \longrightarrow O_2 + 2H_2 \tag{1.5}$$

Water splitting is an endergonic reaction, $\Delta G^0 = +237$ kJ mol^{-1} at 298 K and 1 bar, thus is can be used to store energy as chemical bonds.[86] The minimum cell potential required to drive water splitting at room temperature is 1.23 V. This standard potential, E^0, can be calculated from the Gibbs free energy change, ΔG^0, according to Equation 1.6.

$$\Delta G^0 = -n \times F \times E^0 \tag{1.6}$$

where n is the number of electrons per mole of water in the half reactions, n = 2, and F is Faraday's constant. However, to reach appreciable rates of hydrogen production further energy is required. This is the overpotential and therefore, electrocatalysts are introduced to reduce this overpotential and provide lower activation energy pathways.

In a commercial electrolyser under acidic conditions hydrogen is produced at the cathode, Equation 1.7, and water is oxidised at the anode, Equation 1.8. Electrons travel through the external circuit, and protons travel through the membrane, separating the anode and cathode, to the cathode. At the cathode they combine via the hydrogen evolution reaction. The most common electrocatalyst for the cathode under acidic conditions is platinum, whilst IrO_2 and RuO_2 are commonly used as anode materials.

$$2H^+ + 2e^- \longrightarrow H_2 \tag{1.7}$$

$$2H_2O \longrightarrow O_2 + 4H^+ + 4e^- \tag{1.8}$$

Under basic conditions the oxygen evolution and hydrogen evolution are given by Equations 1.9 and 1.10, respectively. Transition metals, and their alloys and oxides are typically used as anodes and cathodes in this case.

$$4\,OH^- \longrightarrow 2\,H_2O + O_2 + 4\,e^- \tag{1.9}$$

$$2\,H_2O + 2\,e^- \longrightarrow H_2 + 2\,OH^- \tag{1.10}$$

1.5.1 The Role of pH in Hydrogen Evolution

The effect of pH on water electrolysis can be seen by examining the Nernst equation, Equation 1.11, for the anode and cathode reactions.

$$E = E^0 - \frac{RT}{nF} \ln Q \tag{1.11}$$

$$Q = \frac{[\mathrm{Red}]}{[\mathrm{Ox}]} \tag{1.12}$$

E is the reduction potential, E^0 is the standard potential, R is the universal gas constant, T is the temperature, n and F are the number of electrons per mole of reactant and Faraday's constant as above, and Q is the reaction quotient. Q defines the activity and can be determined from the concentration of the reduced and oxidised species, Equation 1.12. By inserting the values of the constants, the standard reaction conditions and converting the logarithm to base 10, Equation 1.13 is achieved.

$$E = E^0 - \frac{0.059}{n} \log Q \tag{1.13}$$

The reduction potential can therefore be correlated to the pH according to the following equations:

For the evolution of hydrogen, Equation 1.7, where $E^0 = 0$ V,

$$\begin{aligned} E &= E^0 - \frac{0.059}{-2}\log[H^+]^2 \\ &= 0 \text{ V} - 0.059 \times \text{pH} \end{aligned} \tag{1.14}$$

and for Equation 1.8, the oxygen evolution reaction where $E^0 = 1.23$ V,

$$\begin{aligned} E &= E^0 - \frac{0.059}{-4}\log[H^+]^4 \\ &= 1.23 \text{ V} - 0.059 \times \text{pH} \end{aligned} \tag{1.15}$$

thus for every 1 pH unit increase, the reduction potential of each half-reaction shifts by 59 mV.[87] Whilst this pH dependence would cancel out in a full electrolyser set-up, when investigating an individual half-reaction such as hydrogen evolution with a potentiostat, it is important to be able to compare performance regardless of pH. This is why potentials are defined in relation to the reversible hydrogen electrode, RHE, Equation 1.16.

$$E_{\text{RHE}} = E_{\text{NHE}} - 0.059 \times \text{pH} \tag{1.16}$$

The pH also affects the kinetics of the hydrogen evolution reaction. Typically hydrogen evolution is performed under extreme pH conditions. Highly conductive electrolytes are employed to decrease losses due to poor ion transport. Consequently, as two of the most conductive ions, H_3O^+ and OH^-, result in the use of highly acidic or basic conditions.[88] Generally electrical conductance varies as, H_2SO_4 > KOH > phosphate buffer solution; higher conductance suggests faster intrinsic kinetics due to increased ion migration rates,[89] resulting in higher current densities, for a given overpotential. The catalytic pathway of hydrogen evolution is pH-dependent, so the electrolyte choice may have an affect on the perceived performance of an electrocatalyst.

1.5.1.1 Acidic Mechanism

It is generally accepted that under acidic conditions hydrogen evolution at various metal surfaces occurs by one of two mechanisms each consisting of two elementary steps.[90,91] In both mechanisms the first step is the adsorption of H^+ on the catalyst surface to give H^*, an adsorbed hydrogen atom, Equation 1.17. Here * represents an active site at the catalyst surface. This mechanistic step is referred to as the Volmer step. Following adsorption, one of two steps can occur. The adsorbed hydrogen can combine with a proton to form H_2, Equation 1.18; this is termed the Heyrovsky step. Alternatively, two adsorbed hydrogen atoms can combine on the catalyst surface via the Tafel reaction, Equation 1.19. Regardless of whether the Volmer-Heyrovsky or Volmer-Tafel pathway is taken the mechanisms combine to give the overall acidic hydrogen evolution reaction as Equation 1.7.

$$H^+ + e^- \longrightarrow H^* \tag{1.17}$$

$$H^+ + H^* + e^- \longrightarrow H_2 \tag{1.18}$$

$$H^* + H^* \longrightarrow H_2 \tag{1.19}$$

The Sabatier principle suggests that intermediate metal-hydrogen binding is required to optimise hydrogen evolution kinetics. Trasatti was the first to plot metal-hydride formation energy against the exchange currents for hydrogen evolution of various metal catalysts; a clear volcano plot relationship could be seen.[92] The volcano plot has since been updated, following density functional theory calculations by Nørskov *et al.* that allowed the acidic hydrogen evolution activity to be plotted against hydrogen adsorption energy, Figure 1.11.[93] The superiority of Pt can be observed alongside the clear volcano paradigm which has led to the development of several other successful hydrogen evolution electrocatalysts.[94,95]

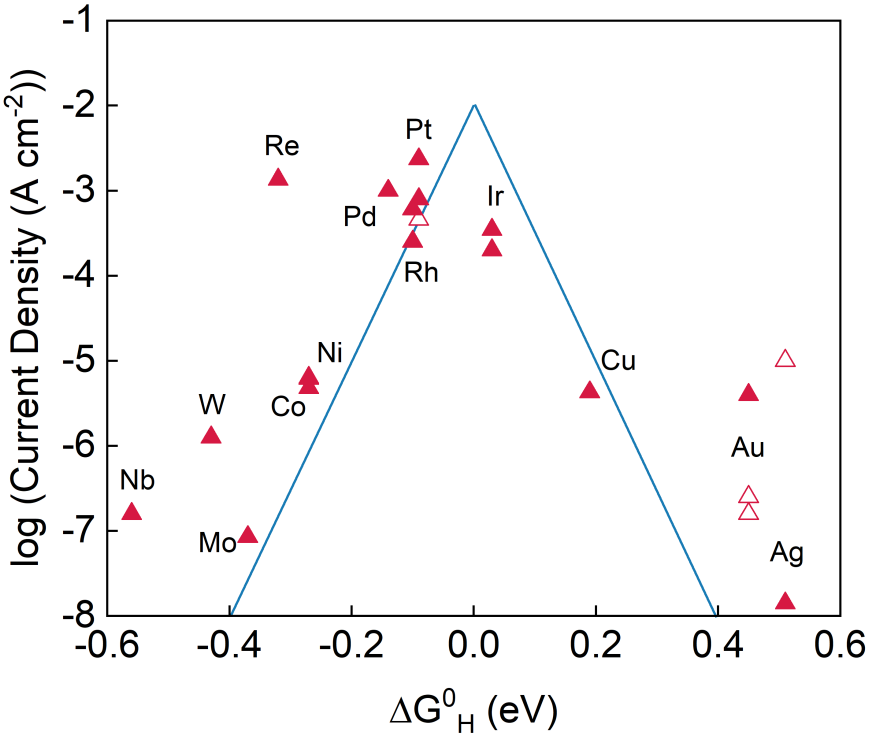

Figure 1.11: Volcano plot of the exchange current densities of a variety of pure metals (single crystals are shown as open triangles) as a function of the Gibbs free energy of adsorbed atomic hydrogen, as calculated by Nørskov et al.[93]

1.5.1.2 Alkaline Mechanism

In basic media the overall hydrogen evolution reaction is described by Equation 1.10. The proposed reactions steps are similar to those seen in acid except that the adsorbed hydrogen is formed from H_2O via dissociation.[96] Once again the mechanism begins with a discharge step, Equation 1.20, wherein a hydrogen atom becomes adsorbed at the metal surface. The Volmer step is then followed by either the Heyrovsky - Equation 1.21, or Tafel step - Equation 1.22.

$$H_2O + e^- \longrightarrow H^* + OH^- \tag{1.20}$$

$$H^* + H_2O + e^- \longrightarrow OH^- + H_2 \tag{1.21}$$

$$H^* + H^* \longrightarrow H_2 \tag{1.22}$$

Hydrogen evolution activity is typically lower in high pH electrolytes relative to low pH electrolytes.[96] It has been suggested that this is because the reaction is governed by both the interaction between H^* and the metal surface, and the dissociation of water.[97] In comparison to the volcano plot seen in acidic media, for alkaline media, only shifts in current density are observed for each metal catalyst.[98] This is because the M−H binding is calculated using the same DFT method regardless of the electrolyte.[99] Therefore, it is expected that in basic media, the ability of a catalyst to promote water dissociation would be beneficial, and could significantly affect the current density observed.

1.5.1.3 Neutral Mechanism

Discussion of the mechanism for hydrogen evolution under neutral conditions appears to be relatively rare. The mechanism is often assumed to be similar to that which occurs under alkaline conditions, dissociation and adsorption of a hydrogen atom, followed by either the Heyrovsky or Tafel step. However, due to the negligible presence of conductive ions, mass transport is limited and the evolution kinetics are often poor.[100] The reaction is further hampered by the rigid interfacial water layer which forms in neutral media, preventing the transport of ions to the electrode surface.[101]

Hence, at low η hydrogen evolution is sustained by the low concentration of available H^+ near the electrode surface. As the overpotential is increased, the surface H^+ is quickly expended and thus the reaction becomes diffusion controlled.[102] At high η, after a plateau in current, the main reactant switches to H_2O and the reduction current increases again.[102] This changeover occurs because direct hydrogen evolution from water is thermodynamically unfavourable at low overpotential, the reduction of H^+ or H_3O^+ is preferential.[103] Thus improvements to (near)neutral HER often focus on improving the kinetics of water dissociation and surface texturing to increase available active sites such as edges and corners.[104]

1.5.2 Mechanisms and Tafel plots

Experimentally, Tafel slopes are often used to determine the rate determining step and therefore possible mechanism of a given hydrogen evolution catalyst. The Tafel equation can be derived from the Butler-Volmer equation, Equation 1.23, which describes the steady state current density, i, in a well-stirred, low current solution, i.e. there are no mass transport effects.[105]

$$i = i_0 \left[\exp\left(-\frac{\alpha n F \eta}{RT} \right) - \exp\left(\frac{(1-\alpha) n F \eta}{RT} \right) \right] \tag{1.23}$$

i_0 is the exchange current density, α is the charge transfer coefficient, n is the number of electrons transferred, F is Faraday's constant, η is the overpotential, R is the gas constant, and T is the temperature. For large values of η the value of one of the expontentials becomes negligible. Thus for a large negative overpotenital, such as in hydrogen evolution, Equation 1.24 becomes true.

$$i = i_0 \left[\exp\left(-\frac{\alpha n F \eta}{RT} \right) \right] \tag{1.24}$$

Upon rearrangement and conversion from natural logarithms, Equation 1.25 is achieved, which follows the Tafel equation format as shown.

$$\begin{aligned} \eta &= \frac{2.303RT}{\alpha nF} log_{10}[i_0] - \frac{2.303RT}{\alpha nF} log_{10}[i] \\ &= a + b\, log_{10}[i] \end{aligned} \tag{1.25}$$

Therefore, the Tafel slope, b represents a series of constants, Equation 1.26

$$b = -\frac{2.303RT}{\alpha nF} \tag{1.26}$$

The charge transfer coefficient, α, is defined by Equation 1.27.[106,107]

$$\alpha = \frac{n_f}{\nu} + n_\Gamma \beta \tag{1.27}$$

where n_f is the number of electrons transferred prior to the rate determining step, ν, is the number of times the rate determining step must occur in the overall reaction, n_Γ, is the number of electrons transferred during the rate determining step, and β, is the symmetry factor, typically assumed to be a value close to 0.5.[106] Given Equation 1.27, each of the possible rate determining steps, Volmer, Heyrovsky, and Tafel can be used to determine a theoretical Tafel slope. The details for the calculation of which are shown in Table 1.3.

Table 1.3: Calculation of the charge transfer coefficient, α and therefore the theoretical Tafel slope, b, for each possible rate determining step. The acidic regime is shown here however the values calculated are equivalent under neutral or basic conditions.

Reaction Step	**Volmer**	**Heyrovsky**	**Tafel**
Equation	$H^+ + e^- \longrightarrow H^*$	$H^+ + H^* + e^- \longrightarrow H_2$	$H^* + H^* \longrightarrow H_2$
n_f	0	1	2
ν	1 or 2	1	1
n_Γ	1	1	0
β	0.5	0.5	0.5
α	0.5	1.5	2
b/ **mV dec**$^{-1}$	-118	-39	-29

This reveals the origin of the widely accepted Tafel slope values, 120, 40, and 30 mV dec^{-1} for the Volmer, Heyrovsky, and Tafel steps, respectively.[108] This allows the partial prediction of the reaction mechanism, given that if the Volmer step is established to be rate determining which secondary step occurs remains unknown.

1.5.3 Hydrogen Evolution Catalysts

Platinum is often considered as a benchmark catalyst towards hydrogen evolution.[88,109,110] This is no surprise given its position at the apex of many volcano plots, Figure 1.11. Commercially available 20 wt.% Pt on a carbon substrate, Pt/C, can be used as a comparison to newly developed catalysts. Data collected by Lv *et al.* showed Pt/C to have an overpotential of -29 mV at -10 mA cm^{-2} and -166 mV at -500 mA cm^{-2}, with a Tafel slope of 91.5 mV dec^{-1} in 0.1 M KOH.[111] This low overpotential was suggested to be the result of the intermediate M–H binding strength of Pt. However, increased scarcity and price has moved the research focus away from Pt and other platinum-group metals towards alternative transition metal and earth-abundant based catalysts.[112]

One method for finding new hydrogen evolution catalysts has been to use the volcano plots developed by Trasatti[92] and later Nørskov[93] as inspiration. Consequently, Lu and coworkers chose metals from opposing slopes of the volcano plot, Cu and Ti, both of which are poor hydrogen evolution catalysts when used alone.[95] Density function theory modelling proposed an adsorption site containing two Cu centres and one Ti centre would produce activity on par with Pt. This was experimentally verified by testing a range of CuTi alloys with a stoichiometric ratio of 1–9% Ti synthesised by arc-melting followed by melt-spinning. The maximum enhancement in activity was seen by the catalyst with a bulk stiochiometry of $Cu_{95}Ti_5$; in 0.1 M KOH the overpotential, although not explicitly listed, was shown graphically to be lower than the commercial Pt/C catalyst tested. The Tafel slope was 110 mV dec^{-1}, which was also consistent with the Pt/C catalyst.

Inspired by the volcano plots Hinnemann *et al.* used density functional theory to first confirm that a binding free energy for hydrogen close to zero is a valid criterion for a good hydrogen evolution catalyst.[94] Using this as a guide they were able to identify an inorganic analogue, MoS_2, from the hydrogen producing enzyme, nitrogenase. In particular the MoS_2 edge has a close resemblance to the active centre of nitrogenase. Experimentally,

they were able to confirm reasonable hydrogen evolution activity of MoS_2 nanoparticles, despite bulk MoS_2 being known to be a poor catalyst.[94] This was then taken further when a combination in in situ and ex situ techniques were used to confirm that the rate of reaction on MoS_2 is directly proportional to the number of edge sites present.[113]

Since this work, the importance of the identification and exposure of active sites has become increasingly prevalent. One facile synthesis approach was developed by Li *et al.* who used a solvothermal synthesis on reduced graphene oxide to achieve an abundance of exposed MoS_2 edges.[114] Testing in 0.5 M H_2SO_4 revealed an overpotential of ≈ 150 mV at -10 mA cm^{-2}, and a Tafel slope of 41 mV dec^{-1}, which is highly competitive relative to other hydrogen evolution catalysts including platinum.

A variety of other transition metal catalysts have also been investigated following the identification of MoS_2 edge sites. These include both transition metal and non-transition metal: sulfides, selenides, oxides, carbides, phosphides, and nitrides.[110,115] Comparison of the material groups revealed that phosphorous based catalysts appear to achieve the closest overpotentials to Pt-based catalysts, which remain the most promising, based solely on this metric.[110] The best Pt-free alloys have also proven to achieve overpotentials in line with Pt-based catalysts.

Many types of hydrogen evolution electrocatalysts have been researched and only briefly mentioned in this short introduction, however, a more thorough review of the catalysts that inspired the work in this thesis can be found in the introduction to Chapter 4.

1.6 Conclusions

Here, a short review of a selection of bimetallic and trimetallic electrocatalysts for CO_2 reduction is given, showcasing the most recent developments in the field of CO_2 electroreduction. The possible combinations of two or three metals, on top of the use of different synthesis techniques and mixing patterns, are endless. It is important to focus on those which produce desirable products at a high Faradaic efficiency and low overpotential. Cu-based catalysts appear to be the way forward due to copper's C−C coupling proficiency; the use of Ni and Zn as a secondary metal seem promising, reporting significant Faradaic efficiencies towards C_2 products. However, far fewer reports into C_2 products are available compared to those with predominant CO and/or formate production. This remains one of the biggest challenges in the field, electrochemical reduction of CO_2 to CO can be performed in aqueous solution at current densities in excess of 0.8 A cm^{-2} with Faradaic yields >98 %.[116] It is now that ways to efficiently reduce CO_2 past CO, by more than two electrons, need to be devised.

A deep mechanistic understanding of the synergistic effects between particular bimetallic and trimetallic combinations would benefit the field, aiding the understanding of why certain combinations are more effective/selective than others. A more systematic approach towards metal selection and screening would be beneficial.[117] A wider selection of materials including molecular catalysts and more complex multi-metallic catalysts should also be screened. Thorough and systematic study should find the optimum catalyst for the electrochemical reduction of CO_2 towards multi-carbon products.

A short review of the basics of electrochemical hydrogen evolution and its accompanying catalysts is also included. Development of Pt-free catalysts that compete with the activity seen by platinum remain the key goal of hydrogen evolution, targeting low overpotentials and Tafel slopes. It is also important that high Faradaic efficiencies can be tested and

maintained over industrially relevant time periods. Although the catalyst itself is a crucial element in both the investigated processes, it is worth noting that other elements of the experimental set-up, including cell design, electrolyte choice, pH, and the anodic reaction, should also be enhanced to reach a true optimum electrochemical performance.

1.7 References

[1] Intergovernmental Panel on Climate Change (IPCC), *Climate Change 2021 – The Physical Science Basis*, Cambridge University Press, 2021.

[2] P. Kumar, *Frontiers in Sustainable Cities*, 2021, **3**, 1–8.

[3] C. C. C. Service, *Copernicus Climate Change Service*, 2024, 1–24.

[4] E. Dlugokencky and P. Tans, *NOAA/ESRL*, `www.esrl.noaa.gov/gmd/ccgg/trends/`.

[5] U. Nations, *Framework Convention on Climate Change (2015) Adoption of the Paris Agreement*, 2015, 1–32.

[6] A. Majumdar and J. Deutch, *Joule*, 2018, **2**, 805–809.

[7] S. Nitopi, E. Bertheussen, S. B. Scott, X. Liu, A. K. Engstfeld, S. Horch, B. Seger, I. E. L. Stephens, K. Chan, C. Hahn, J. K. Nørskov, T. F. Jaramillo and I. Chorkendorff, *Chemical Reviews*, 2019, **119**, 7610–7672.

[8] P. D. Luna, C. Hahn, D. Higgins, S. A. Jaffer, T. F. Jaramillo and E. H. Sargent, *Science*, 2019, **364**, eaav3506.

[9] W. da Silva Freitas, A. D'Epifanio and B. Mecheri, *Journal of CO2 Utilization*, 2021, **50**, 101579.

[10] Z. Sun, T. Ma, H. Tao, Q. Fan and B. Han, *Chem*, 2017, **3**, 560–587.

[11] J. Zhao, S. Xue, J. Barber, Y. Zhou, J. Meng and X. Ke, *Journal of Materials Chemistry A*, 2020, **8**, 4700–4734.

[12] D. Schröder, C. A. Schalley, J. N. Harvey and H. Schwarz, *International Journal of Mass Spectrometry*, 1999, **185-187**, 25–35.

[13] M. H. V. Huynh and T. J. Meyer, *Chemical Reviews*, 2007, **107**, 5004–5064.

[14] J. Qiao, Y. Liu, F. Hong and J. Zhang, *Chemical Society Reviews*, 2014, **43**, 631–675.

[15] E. Tayyebi, J. Hussain, Y. Abghoui and E. Skúlason, *The Journal of Physical Chemistry C*, 2018, **122**, 10078–10087.

[16] R. Francke, B. Schille and M. Roemelt, *Chemical Reviews*, 2018, **118**, 4631–4701.

[17] Q. Lu, K. Eid, W. Li, A. M. Abdullah, G. Xu and R. S. Varma, *Green Chemistry*, 2021, **23**, 5394–5428.

[18] Y. Hori, K. Kikuchi and S. Suzuki, *Chemistry Letters*, 1985, **14**, 1695–1698.

[19] Y. Hori, A. Murata and R. Takahashi, *Journal of the Chemical Society, Faraday Transactions 1: Physical Chemistry in Condensed Phases*, 1989, **85**, 2309.

[20] Y. Hori, H. Wakebe, T. Tsukamoto and O. Koga, *Electrochimica Acta*, 1994, **39**, 1833–1839.

[21] D. T. Whipple and P. J. A. Kenis, *The Journal of Physical Chemistry Letters*, 2010, **1**, 3451–3458.

[22] A. A. Peterson and J. K. Nørskov, *The Journal of Physical Chemistry Letters*, 2012, **3**, 251–258.

[23] F. Abild-Pedersen, J. Greeley, F. Studt, J. Rossmeisl, T. R. Munter, P. G. Moses, E. Skúlason, T. Bligaard and J. K. Nørskov, *Phys. Rev. Lett.*, 2007, **99**, 016105.

[24] Y. Li and Q. Sun, *Advanced Energy Materials*, 2016, **6**, 1600463.

[25] A. Vasileff, C. Xu, Y. Jiao, Y. Zheng and S.-Z. Qiao, *Chem*, 2018, **4**, 1809–1831.

[26] G. O. Larrazábal, A. J. Martín and J. Pérez-Ramírez, *The Journal of Physical Chemistry Letters*, 2017, **8**, 3933–3944.

[27] D. M. Morales and M. Risch, *Journal of Physics: Energy*, 2021, **3**, 034013.

[28] L. Zhang, Z.-J. Zhao and J. Gong, *Angewandte Chemie International Edition*, 2017, **56**, 11326–11353.

[29] J. Wu, Y. Huang, W. Ye and Y. Li, *Advanced Science*, 2017, **4**, 1700194.

[30] M. Watanabe, M. Shibata, A. Kato, M. Azuma and T. Sakata, *Journal of The Electrochemical Society*, 1991, **138**, 3382–3389.

[31] J. He, N. J. J. Johnson, A. Huang and C. P. Berlinguette, *ChemSusChem*, 2018, **11**, 48–57.

[32] M. K. Birhanu, M.-C. Tsai, A. W. Kahsay, C.-T. Chen, T. S. Zeleke, K. B. Ibrahim, C.-J. Huang, W.-N. Su and B.-J. Hwang, *Advanced Materials Interfaces*, 2018, **5**, 1800919.

[33] C. Xiao and J. Zhang, *ACS Nano*, 2021, **15**, 7975–8000.

[34] D. Karapinar, C. E. Creissen, J. G. Rivera de la Cruz, M. W. Schreiber and M. Fontecave, *ACS Energy Letters*, 2021, **6**, 694–706.

[35] Y. Liu, H. Qiu, J. Li, L. Guo and J. W. Ager, *ACS Applied Materials & Interfaces*, 2021, **13**, 40513–40521.

[36] L. Wu, K. E. Kolmeijer, Y. Zhang, H. An, S. Arnouts, S. Bals, T. Altantzis, J. P. Hofmann, M. Costa Figueiredo, E. J. M. Hensen, B. M. Weckhuysen and W. van der Stam, *Nanoscale*, 2021, **13**, 4835–4844.

[37] C. Choi, J. Cai, C. Lee, H. M. Lee, M. Xu and Y. Huang, *Nano Research*, 2021, **14**, 3497–3501.

[38] L. R. L. Ting, O. Piqué, S. Y. Lim, M. Tanhaei, F. Calle-Vallejo and B. S. Yeo, *ACS Catalysis*, 2020, **10**, 4059–4069.

[39] H. Shang, D. Kim, S. K. Wallentine, M. Kim, D. M. Hofmann, R. Dasgupta, C. J. Murphy, A. Asthagiri and L. R. Baker, *Chemical Science*, 2021, **12**, 9146–9152.

[40] X. Ma, Y. Shen, S. Yao, C. An, W. Zhang, J. Zhu, R. Si, C. Guo and C. An, *Journal of Materials Chemistry A*, 2020, **8**, 3344–3350.

[41] W. Zhu, K. Zhao, S. Liu, M. Liu, F. Peng, P. An, B. Qin, H. Zhou, H. Li and Z. He, *Journal of Energy Chemistry*, 2019, **37**, 176–182.

[42] L. Peng, Y. Wang, Y. Wang, N. Xu, W. Lou, P. Liu, D. Cai, H. Huang and J. Qiao, *Applied Catalysis B: Environmental*, 2021, **288**, 120003.

[43] Y. Xiong, B. Wei, M. Wu, B. Hu, F. Zhu, J. Hao and W. Shi, *Journal of CO2 Utilization*, 2021, **51**, 101621.

[44] X. Zhang, L. Peng, B. Xu, P. Liu, X. Jiao, H. Kang, Z. Song, X. Yan, Y. Mao and J. Qiao, *Process Safety and Environmental Protection*, 2022, **158**, 560–566.

[45] Y. Takatsuji, I. Nakata, M. Morimoto, T. Sakakura, R. Yamasaki and T. Haruyama, *Electrocatalysis*, 2019, **10**, 29–34.

[46] J. Shao, Y. Wang, D. Gao, K. Ye, Q. Wang and G. Wang, *Chinese Journal of Catalysis*, 2020, **41**, 1393–1400.

[47] C. Shen, P. Wang, L. Li, X. Huang and Q. Shao, *Nano Research*, 2022, **15**, 528–534.

[48] B. Wei, Y. Xiong, Z. Zhang, J. Hao, L. Li and W. Shi, *Applied Catalysis B: Environmental*, 2021, **283**, 119646.

[49] X. Zhang, C. Liu, Y. Zhao, L. Li, Y. Chen, F. Raziq, L. Qiao, S.-X. Guo, C. Wang, G. G. Wallace, A. M. Bond and J. Zhang, *Applied Catalysis B: Environmental*, 2021, **291**, 120030.

[50] T. M. Suzuki, T. Ishizaki, S. Kosaka, N. Takahashi, N. Isomura, J. Seki, Y. Matsuoka, K. Oh-ishi, A. Oshima, K. Kitazumi, K. Sekizawa and T. Morikawa, *Chemical Communications*, 2020, **56**, 15008–15011.

[51] L. Zhu, Y. Lin, K. Liu, E. Cortés, H. Li, J. Hu, A. Yamaguchi, X. Liu, M. Miyauchi, J. Fu and M. Liu, *Chinese Journal of Catalysis*, 2021, **42**, 1500–1508.

[52] R. Zhou, X. Fan, X. Ke, J. Xu, X. Zhao, L. Jia, B. Pan, N. Han, L. Li, X. Liu, J. Luo, H. Lin and Y. Li, *Nano Letters*, 2021, **21**, 4092–4098.

[53] V. S. S. Mosali, L. Li, G. Puxty, M. D. Horne, A. M. Bond and J. Zhang, *ChemElectroChem*, 2022, **9**, e202101227.

[54] W. J. Dong, J. W. Lim, J. Y. Park, C. J. Yoo, S. Baek, W. S. Cho, W. Kim and J.-L. Lee, *Applied Surface Science*, 2021, **565**, 150460.

[55] D. Li, L. Huang, Y. Tian, T. Liu, L. Zhen and Y. Feng, *Applied Catalysis B: Environmental*, 2021, **292**, 120119.

[56] H. Li, X. Yue, Y. Qiu, Z. Xiao, X. Yu, C. Xue and J. Xiang, *Materials Today Energy*, 2021, **21**, 100797.

[57] L. Shang, X. Lv, L. Zhong, S. Li and G. Zheng, *Small Methods*, 2022, **6**, 2101334.

[58] S. Dongare, N. Singh and H. Bhunia, *Applied Surface Science*, 2021, **556**, 149790.

[59] L. Wang, H. Peng, S. Lamaison, Z. Qi, D. M. Koshy, M. B. Stevens, D. Wakerley, J. Zamora Zeledón, L. A. King, L. Zhou, Y. Lai, M. Fontecave, J. Gregoire, F. Abild-Pedersen, T. F. Jaramillo and C. Hahn, *Chem Catalysis*, 2021, **1**, 663–680.

[60] L. Wan, X. Zhang, J. Cheng, R. Chen, L. Wu, J. Shi and J. Luo, *ACS Catalysis*, 2022, **12**, 2741–2748.

[61] V. S. S. Mosali, X. Zhang, Y. Zhang, T. Gengenbach, S.-X. Guo, G. Puxty, M. D. Horne, A. M. Bond and J. Zhang, *ACS Sustainable Chemistry & Engineering*, 2019, **7**, 19453–19462.

[62] S. Lamaison, D. Wakerley, F. Kracke, T. Moore, L. Zhou, D. U. Lee, L. Wang, M. A. Hubert, J. E. Aviles Acosta, J. M. Gregoire, E. B. Duoss, S. Baker, V. A. Beck, A. M. Spormann, M. Fontecave, C. Hahn and T. F. Jaramillo, *Advanced Materials*, 2022, **34**, 2103963.

[63] A. Jo, S. Kim, H. Park, H.-Y. Park, J. Hyun Jang and H. S. Park, *Journal of Catalysis*, 2021, **393**, 92–99.

[64] J. Hao, H. Zhu, Y. Li, P. Liu, S. Lu, F. Duan, W. Dong, Y. Lu, T. Liu and M. Du, *Chemical Engineering Journal*, 2021, **404**, 126523.

[65] Y. Ito, S. Kukunuri, S. Jeong, G. Elumalai, A. A. Haji Tajuddin, Z. Xi, K. Hu and T. Ohto, *ACS Applied Energy Materials*, 2021, **4**, 7122–7128.

[66] D. Pavesi, R. C. J. van de Poll, J. L. Krasovic, M. Figueiredo, G.-J. M. Gruter, M. T. M. Koper and K. J. P. Schouten, *ACS Sustainable Chemistry & Engineering*, 2020, **8**, 15603–15610.

[67] Q. Hu, M. Xu, S. Hu, P.-L. Tremblay and T. Zhang, *Journal of Electroanalytical Chemistry*, 2020, **877**, 114623.

[68] G. H. Han, J. Kim, S. Jang, H. Kim, W. Guo, S. Hong, J. Shin, I. Nam, H. W. Jang, S. Y. Kim and S. H. Ahn, *Advanced Science*, 2022, **9**, 2104908.

[69] Y. Zhu, Z. Gao, Z. Zhang, T. Lin, Q. Zhang, H. Liu, L. Gu and W. Hu, *Nano Research*, 2022, **15**, 7861–7867.

[70] T. Cheng, H. Xiao and W. A. Goddard, *Proceedings of the National Academy of Sciences*, 2017, **114**, 1795–1800.

[71] A. J. Garza, A. T. Bell and M. Head-Gordon, *ACS Catalysis*, 2018, **8**, 1490–1499.

[72] E. D. Goodman, J. A. Schwalbe and M. Cargnello, *ACS Catalysis*, 2017, **7**, 7156–7173.

[73] R. Kortlever, J. Shen, K. J. P. Schouten, F. Calle-Vallejo and M. T. M. Koper, *The Journal of Physical Chemistry Letters*, 2015, **6**, 4073–4082.

[74] P. Hirunsit, W. Soodsawang and J. Limtrakul, *Journal of Physical Chemistry C*, 2015, **119**, 8238–8249.

[75] C.-T. Dinh, T. Burdyny, M. G. Kibria, A. Seifitokaldani, C. M. Gabardo, F. P. G. de Arquer, A. Kiani, J. P. Edwards, P. D. Luna, O. S. Bushuyev, C. Zou, R. Quintero-Bermudez, Y. Pang, D. Sinton and E. H. Sargent, *Science*, 2018, **360**, 783–787.

[76] J. H. Montoya, A. A. Peterson and J. K. Nørskov, *ChemCatChem*, 2013, **5**, 737–742.

[77] E. L. Clark, C. Hahn, T. F. Jaramillo and A. T. Bell, *Journal of the American Chemical Society*, 2017, **139**, 15848–15857.

[78] T. Takeguchi, T. Yamanaka, K. Asakura, E. N. Muhamad, K. Uosaki and W. Ueda, *Journal of the American Chemical Society*, 2012, **134**, 14508–14512.

[79] I. Kotoulas, A. Schizodimou and G. Kyriacou, *The Open Electrochemistry Journal*, 2013, **5**, 8–12.

[80] J. He, K. E. Dettelbach, A. Huang and C. P. Berlinguette, *Angewandte Chemie International Edition*, 2017, **56**, 16579–16582.

[81] A. P. Van Troostwijk and J. R. Deiman, *Journal de Physique, de Chimie et d'Histoire Naturelle*, 1789, **35**, 369–378.

[82] S. Trasatti, *Journal of Electroanalytical Chemistry*, 1999, **476**, 90–91.

[83] A. Kovač, M. Paranos and D. Marciuš, *International Journal of Hydrogen Energy*, 2021, **46**, 10016–10035.

[84] H. Ishaq, I. Dincer and C. Crawford, *International Journal of Hydrogen Energy*, 2022, **47**, 26238–26264.

[85] G. Kakoulaki, I. Kougias, N. Taylor, F. Dolci, J. Moya and A. Jäger-Waldau, *Energy Conversion and Management*, 2021, **228**, 113649.

[86] N. Kelly, in *Advances in Hydrogen Production, Storage and Distribution*, ed. A. Basile and A. Iulianelli, Woodhead Publishing, 2014, pp. 159–185.

[87] C. Lefrou, P. Fabry and J.-C. Poignet, *Electrochemistry: The Basics, with examples*, Springer Berlin Heidelberg, 2012.

[88] P. C. K. Vesborg, B. Seger and I. Chorkendorff, *The Journal of Physical Chemistry Letters*, 2015, **6**, 951–957.

[89] J. Wang, F. Xu, H. Jin, Y. Chen and Y. Wang, *Advanced Materials*, 2017, **29**, 1605838.

[90] B. Conway and B. Tilak, *Electrochimica Acta*, 2002, **47**, 3571–3594.

[91] G. Zhao, K. Rui, S. X. Dou and W. Sun, *Advanced Functional Materials*, 2018, **28**, 1803291.

[92] S. Trasatti, *Journal of Electroanalytical Chemistry and Interfacial Electrochemistry*, 1972, **39**, 163–184.

[93] J. K. Nørskov, T. Bligaard, A. Logadottir, J. R. Kitchin, J. G. Chen, S. Pandelov and U. Stimming, *Journal of The Electrochemical Society*, 2005, **152**, J23.

[94] B. Hinnemann, P. G. Moses, J. Bonde, K. P. Jørgensen, J. H. Nielsen, S. Horch, I. Chorkendorff and J. K. Nørskov, *Journal of the American Chemical Society*, 2005, **127**, 5308–5309.

[95] Q. Lu, G. S. Hutchings, W. Yu, Y. Zhou, R. V. Forest, R. Tao, J. Rosen, B. T. Yonemoto, Z. Cao, H. Zheng, J. Q. Xiao, F. Jiao and J. G. Chen, *Nature Communications*, 2015, **6**, 6567.

[96] T. Schmidt, P. Ross and N. Markovic, *Journal of Electroanalytical Chemistry*, 2002, **524-525**, 252–260.

[97] N. Danilovic, R. Subbaraman, D. Strmcnik, K. Chang, A. P. Paulikas, V. R. Stamenkovic and N. M. Markovic, *Angewandte Chemie International Edition*, 2012, **51**, 12495–12498.

[98] N. Danilovic, R. Subbaraman, D. Strmcnik, V. Stamenkovic and N. Markovic, *Journal of the Serbian Chemical Society*, 2013, **78**, 2007–2015.

[99] W. Sheng, M. Myint, J. G. Chen and Y. Yan, *Energy Environ. Sci.*, 2013, **6**, 1509–1512.

[100] M. Maji, S. Dutta, R. Jena, A. Dey, T. K. Maji, S. K. Pati and S. Bhattacharyya, *Angewandte Chemie International Edition*, 2024, **63**, e202403697.

[101] K. Sun, X. Wu, Z. Zhuang, L. Liu, J. Fang, L. Zeng, J. Ma, S. Liu, J. Li, R. Dai, X. Tan, K. Yu, D. Liu, W.-C. Cheong, A. Huang, Y. Liu, Y. Pan, H. Xiao and C. Chen, *Nature Communications*, 2022, **13**, 6260.

[102] Z. Zhou, Z. Pei, L. Wei, S. Zhao, X. Jian and Y. Chen, *Energy & Environmental Science*, 2020, **13**, 3185–3206.

[103] T. Shinagawa and K. Takanabe, *Physical Chemistry Chemical Physics*, 2015, **17**, 15111–15114.

[104] C.-T. Dinh, A. Jain, F. P. G. de Arquer, P. D. Luna, J. Li, N. Wang, X. Zheng, J. Cai, B. Z. Gregory, O. Voznyy, B. Zhang, M. Liu, D. Sinton, E. J. Crumlin and E. H. Sargent, *Nature Energy*, 2018, **4**, 107–114.

[105] A. J. Bard, L. R. Faulkner and H. S. P. o. c. White, *Electrochemical methods: fundamentals and applications*, John Wiley & Sons, Ltd, Hoboken, NJ, USA, Third / Allen J. Bard, Larry R. Faulkner, Henry S. White. edn., 2022.

[106] R. Guidelli, R. G. Compton, J. M. Feliu, E. Gileadi, J. Lipkowski, W. Schmickler and S. Trasatti, *Pure and Applied Chemistry*, 2014, **86**, 245–258.

[107] R. L. Doyle and M. E. G. Lyons, in *The Oxygen Evolution Reaction: Mechanistic Concepts and Catalyst Design*, ed. S. Giménez and J. Bisquert, Springer International Publishing, Cham, 2016, pp. 41–104.

[108] T. Shinagawa, A. T. Garcia-Esparza and K. Takanabe, *Scientific Reports*, 2015, **5**, 13801.

[109] I. Roger, M. A. Shipman and M. D. Symes, *Nature Reviews Chemistry*, 2017, **1**, 0003.

[110] M. Ďurovič, J. Hnát and K. Bouzek, *Journal of Power Sources*, 2021, **493**, 229708.

[111] Q.-X. Lv, F.-L. Wang, X.-J. Zhai, J.-Y. Lv, X. Li, H. Hu, S.-T. Wang, Y.-M. Chai and B. Dong, *International Journal of Hydrogen Energy*, 2024, **62**, 699–705.

[112] T. B. Ferriday, P. H. Middleton and M. L. Kolhe, *Energies*, 2021, **14**, 8535.

[113] T. F. Jaramillo, K. P. Jørgensen, J. Bonde, J. H. Nielsen, S. Horch and I. Chorkendorff, *Science*, 2007, **317**, 100–102.

[114] Y. Li, H. Wang, L. Xie, Y. Liang, G. Hong and H. Dai, *Journal of the American Chemical Society*, 2011, **133**, 7296–7299.

[115] J. Zhu, L. Hu, P. Zhao, L. Y. S. Lee and K.-Y. Wong, *Chemical Reviews*, 2020, **120**, 851–918.

[116] S. S. Bhargava, F. Proietto, D. Azmoodeh, E. R. Cofell, D. A. Henckel, S. Verma, C. J. Brooks, A. A. Gewirth and P. J. A. Kenis, *ChemElectroChem*, 2020, **7**, 2001–2011.

[117] J. He, K. E. Dettelbach, D. A. Salvatore, T. Li and C. P. Berlinguette, *Angewandte Chemie International Edition*, 2017, **56**, 6068–6072.

Chapter 2

Experimental Techniques

2.1 Electrochemical Techniques

Throughout this work a variety of electrochemical techniques were utilised; a potentiostat was employed to monitor and/or control the potential, current, charge and resistance in a given experiment, depending on the information required. The measurement of these variables forms the basis of electrochemical analysis, and this work. In this section, the electrochemical techniques applied will be briefly examined.

2.1.1 Electrode Setup

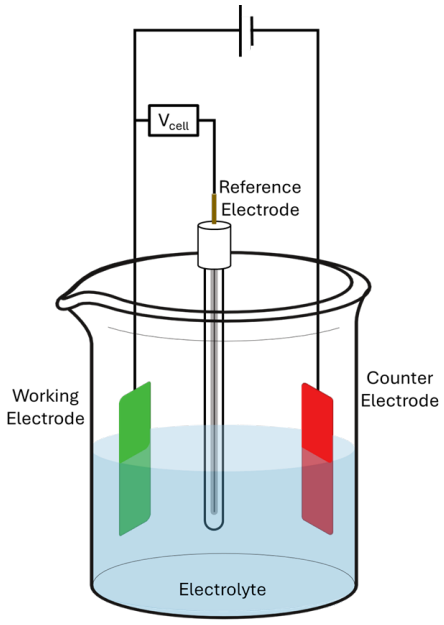

Figure 2.1: Diagram of a typical 3-electrode set up.

The analyses of electrochemical reactions are usually performed in a 3-electrode cell, Figure 2.1. The working electrode, shown here in green, is where the desired reaction occurs. This is the electrode that will be controlled and measured. Working electrodes can be highly varied in terms of material, composition and size; in this thesis catalyst electrodes were developed and tested for given reactions, thus these are always used as the working electrode. The reference electrode contains a well-established redox couple, with

a known half-cell potential which remains constant throughout the reaction conditions used.[1] Examples include Ag/AgCl for aqueous reactions and $Ag/AgNO_3$ for non-aqueous experiments. The final electrode is the counter electrode, shown in red, this is required to complete the circuit, passing equal and opposite current to the working electrode.

In this work, we focused on the analysis of reduction reactions occurring at the cathode, thus the cathode may be referred to as the working electrode and vice versa. The opposing oxidation reactions, which were not specifically monitored, therefore occurred at the counter electrode.

2.1.2 Membranes

For some reactions it is necessary to separate the oxidation and reduction reactions within the cell. This prevents desired products from being re-oxidised back to the starting materials as well as confining the products to particular regions for ease of measurement and safety. Hence membranes can be used to create two-compartment cells.

Several types of membranes are used depending on which components need to be exchanged between the compartments, which need to remain separated, and the reaction conditions. In this thesis a cation exchange membrane, often referred to as a proton exchange membrane, was used. This allowed the passage of water, protons and small cations to the cathode, whilst the movement of gases, anions and large cations was hampered.[2,3] A number of proton exchange membranes are widely available including Nafion, Fumatech and polystyrene.[4] The membranes consist of a robust chemical backbone and negatively charged functional groups (PO_3^-, COO^- and, SO_3^-). Nafion, Figure 2.2, is the membrane used throughout this work. It is a highly fluorinated co-polymer with hydrophilic sulfonic acid groups which line the cation channels.[5] This structure means it is highly conductive and stable in both reductive and oxidative aqueous environments.

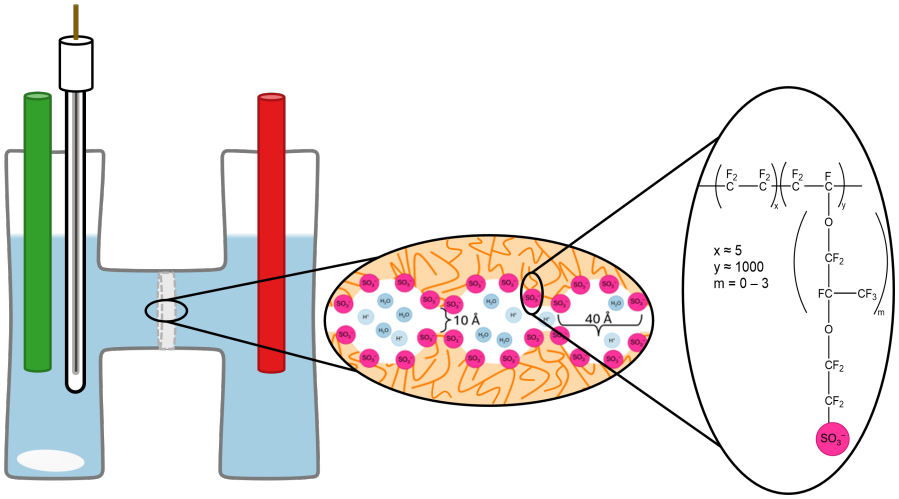

Figure 2.2: Schematic of a two-compartment electrochemical cell showing a generalised view of the pore structure of Nafion alongside its chemical structure.

2.1.3 Cyclic and Linear Sweep Voltammetry

Voltammetry is the measurement of current at a controlled potential. There are many types but the two used predominately in this work were linear sweep voltammetry (LSV) and cyclic voltammetry (CV). LSV sweeps between two given potentials in one direction, from V_1 to V_2, and measures the current. However a cyclic voltammogram cycles between the two potentials, sweeping back to V_1 upon reaching V_2. This gives the path V_1 to V_2 to V_1 etc. as a function of time as shown in Figure 2.3.

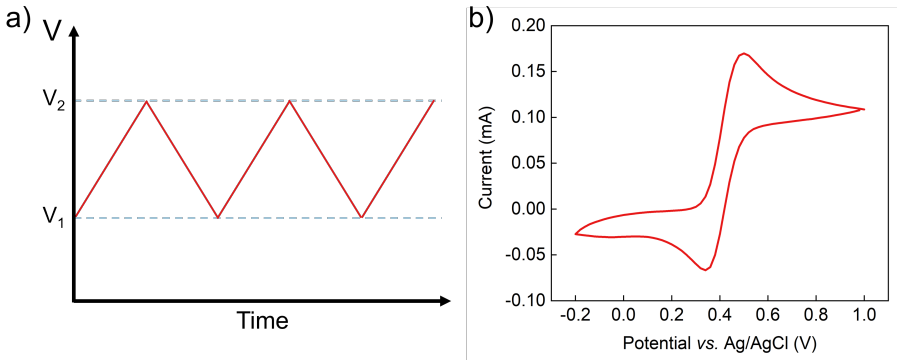

Figure 2.3: a) Potential vs. time graph showing the path of a standard cyclic voltammogram, b) An example cyclic voltammogram of the ferrocenium/ferrocene redox couple.

Cyclic voltammetry can be used to determine the electrochemical reversibility of a redox process. The typical "duck" line shape, as shown in Figure 2.3b, is often suggestive that a redox process is electrochemically reversible.[6]

Chemical reversibility concerns the stability of the electrochemically generated species towards further chemical reactions, equation 2.1.

$$\mathrm{Ox} + n\mathrm{e}^- \rightleftharpoons \mathrm{Red} \xrightarrow{k_c} \mathrm{Z} \tag{2.1}$$

Where Z is a product which cannot be converted back to the oxidised form, Ox, but conversion between the reduced form, Red and Ox is possible. The chemical reversibility is determined by the rate of further conversion as defined by k_c. If k_c is large, the redox couple Ox/Red is chemically irreversible; Red can quickly convert to Z preventing the regeneration of the oxidised species. In contrast, if k_c is small or zero the redox couple can be defined as chemically reversible.[7]

In a heterogeneous electrochemical system the rate of electron transfer is dependent on the concentration of active species at the electrode interface, thus we must involve the mass transfer of the oxidised form from the bulk to the electrode surface, equation 2.2, as well as the electron transfer, equation 2.3.

$$\mathrm{Ox_{bulk}} \longrightarrow \mathrm{Ox_{surface}} \tag{2.2}$$

$$\mathrm{Ox_{surface}} + n\mathrm{e}^- \underset{k_{Ox}}{\overset{k_{Red}}{\rightleftharpoons}} \mathrm{Red_{surface}} \tag{2.3}$$

An electrode process is defined as electrochemically reversible when the rate of electron transfer (k_{Ox} and k_{Red}) is higher than the rate of mass transport.[7] Irreversibility results from slow electron transfer between the electrode and the redox species.[8] A series of distinct properties in terms of potential, current and scan rate of a given redox couple, under cyclic voltammetry, can be used to define its reversibility. A reversible redox process obeys the proceeding constraints:[7]

- The peak-to-peak separation, $\Delta E_p = \frac{59}{n}$ mV at 25 °C, where n is the number of electrons transferred.
- The potential of the reduction and oxidation peaks does not vary with the scan rate.
- The ratio of the current at the forward and reverse peaks is equal to 1, and does not vary with scan rate.
- The current at the forward peak is proportional to the square root of the scan rate.

In practical terms, cyclic voltammetry solutions are not stirred. This allows both electron transport and any mass transport from the bulk solution that occurs to be measured. Stirring disturbs the "natural" diffusion of a given analyte to the electrical double layer at the electrode. Upon the potential sweep, once the potential is sufficiently positive, the electrode acts as an oxidant. This causes a Faradaic current to flow. In Figure 2.3b this can be seen as the oxidation peak at 0.46 V vs. Ag/AgCl and represents the oxidation of ferrocene to ferrocenium.[6] As the sweep continues the current rises and falls as all the ferrocene at the electrode surface is oxidised and the concentration depleted. Thus the rate of oxidation, shown by the current falls. On the return sweep the opposite occurs; the potential becomes sufficiently negative for reduction to occur and the cathodic current is measured. For the ferrocenium reduction to ferrocene a peak is seen at 0.34 V vs. Ag/AgCl. Again the peak shape is defined by diffusion as the ferrocenium near the electrode can be reduced first at a high rate until the concentration at the surface is depleted.[9]

Non-reversible electrochemical reactions are typically examined by linear sweep voltammetry. At first only non-faradaic currents are observed, however when sufficient potential is reached reduction begins and cathodic current measured.[10] In chapter 3 LSV is used to determine the active potential range for CO_2 reduction testing. In chapter 4 it is used for the determination of the Tafel slope; whereby the logarithm of the current density is plotted against the overpotential at the working electrode.[11]

2.1.4 Bulk Electrolysis

Bulk electrolysis is the application of a fixed condition to an electrochemical cell over a given period of time. The use of fixed current is termed chronopotentiometry, and referred to as galvanostatic. This is used to maintain the rate of reaction, the system will alter the potential input to maintain this and different reactions may occur at the electrode. The use of fixed potential is termed chronoamperometry, and referred to as potentiostatic. This technique is preferred to narrow the energy input and target only a specific reaction, increasing selectivity. Bulk electrolysis can be used to determine the theoretical yield of an electrochemical reaction by determining the charged passed, equation 2.4, and comparing it to the theoretical charge as defined by Faraday's laws of electrolysis, equation 2.5.

$$Q = It \tag{2.4}$$

$$Q = mnF \tag{2.5}$$

Where Q is the charge passed, I is the current and t is the reaction time. m is the theoretical number of moles produced, n is the number of electrons passed per mole and F is Faraday's constant (96,485 C mol^{-1}). In this thesis potentiostatic bulk electrolysis is used in chapter 3 and galvanostatic electrolysis is used in chapter 4.

2.2 Nuclear Magnetic Resonance

Nuclear Magnetic Resonance (NMR) spectroscopy is an analytical technique used in the elucidation of molecular structures. The response seen depends of the interaction of nuclear spins with the magnetic field.[12] A nucleus can only be probed by NMR if it has a magnetic moment (μ), equation 2.6, thus is must possess a non-zero spin quantum number, I.

$$\mu = I\gamma\frac{h}{2\pi} \tag{2.6}$$

Where, γ, is the gyromagnetic ratio of the nucleus and h is Planck's constant. It is clear that if I is equal to zero, the magnetic moment will be zero. The value of I originates from the mass number and atomic number of the given nucleus, thus different isotopes of an element have different spin quantum numbers.[13] Generally, nuclei can categorised into one of the following groups:

1. Isotopes with even mass and atomic numbers, such as ${}^{12}_{6}\mathrm{C}$ and ${}^{16}_{8}\mathrm{O}$. For this group I equals zero, and these nuclei are not active towards NMR spectroscopy.
2. Nuclei with even mass numbers and odd atomic numbers, such as ${}^{2}_{1}\mathrm{H}$ and ${}^{14}_{7}\mathrm{N}$. In this grouping I equates to an integer: $I = 1, 2, 3\ldots$ These nuclei experience an electrical quadrupole moment, leading to a non-spherical distribution of charge; they are active towards NMR, however, transitions can be broad and overlapping.[14]
3. Nuclei with odd mass and atomic numbers, such as ${}^{1}_{1}\mathrm{H}$ and ${}^{19}_{9}\mathrm{F}$, and nuclei with odd mass numbers and even atomic numbers, such as ${}^{13}_{6}\mathrm{C}$, have quantum spin numbers that are non-integer multiples of 1/2: $I = \frac{1}{2}, \frac{3}{2}, \frac{5}{2}\ldots$

Magnetic moments operate like bar magnets, typically, they are randomly oriented but in the presence of a strong magnetic field, B_0, such as in an NMR spectrometer, the magnetic moments align, some parallel and some anti-parallel with the external field, Figure 2.4.

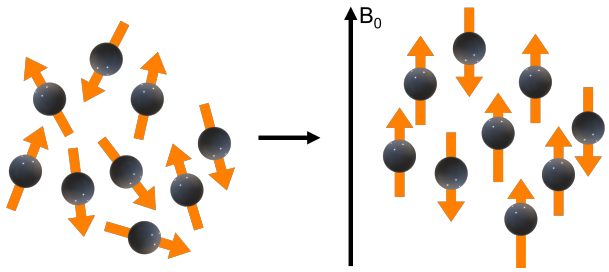

Figure 2.4: Diagram showing nuclei spin alignment in the presence of an external magnetic field, B_0

For a nucleus with spin, I, there are $2I+1$ spin-states, indicated by the magnetic quantum number, m. For the ^{1}H isotope, $m = +\frac{1}{2}$, denoted α and $-\frac{1}{2}$, denoted β. These spin states are described by distinct energy levels, the difference in which is proportional to the magnetic field strength, Figure 2.5. Typically the α spin state is the one with the lowest energy.[12] The energy difference between the spin states is of a magnitude so small that the introduction of energy as radiofrequency radiation is enough to induce transitions between the two states, in a static magnetic field. After excitation, the nuclei return to the lower energy states by relaxation during which a pulse of radiofrerquency (Rf) is emitted and detected by the spectrometer.

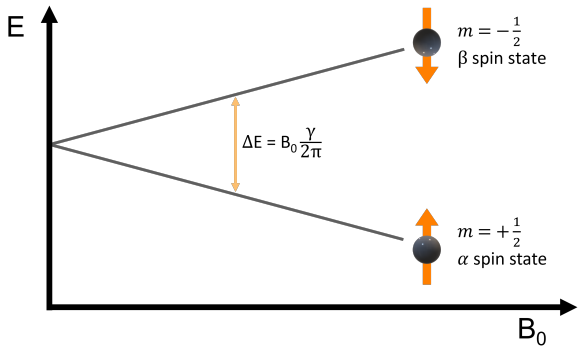

Figure 2.5: Diagram showing how the energy gap between the α and β spin-states depends on the magnetic field strength.

The Bohr relation, equation 2.7, can be used to determine the frequency needed for the transitions between the energy states. This is commonly expressed in terms of the gyromagnetic ratio to give the Larmor frequency (equation 2.8). The Larmor frequency is proportional to the magnetic field strength, thus by increasing the magnetic field strength and thereby the frequency, ΔE is increased; hence NMR spectrometers of higher frequency

are more sensitive.

$$\Delta E = h\nu \tag{2.7}$$

$$\nu = B_0 \frac{\gamma}{2\pi} \tag{2.8}$$

At a macroscopic level we describe the behaviour of all the contributing nuclei using the vector model. Herein we can compile the effect of all the magnetic moments present to reveal a bulk magnetisation vector, M_0, Figure 2.6. At equilibrium, over half the magnetic moments are spin-up, since this is a lower energy state, consequently, these are not cancelled out and M_0 is spin-up.

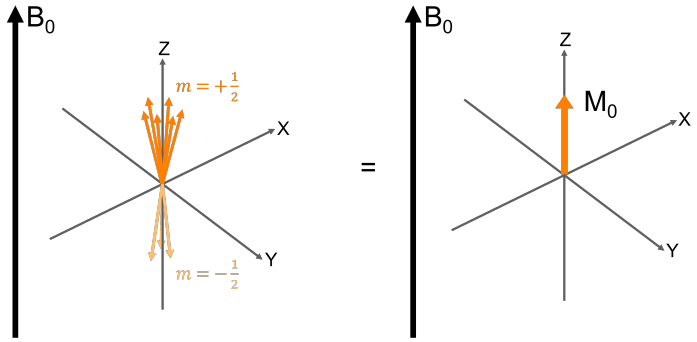

Figure 2.6: Graphic representation of the bulk magnetisation vector, resulting from many magnetic moments at equilibrium.

As before, in a static magnetic field, M_0 precesses about the z-axis at the Larmor frequency. When a Rf pulse is emitted at a frequency matching the Larmor frequency, and at a right-angle to the external field, depicted here as a coil on the x-axis, Figure 2.7, the vector absorbs this energy and many individual magnetic moments flip to the opposing state. This causes the bulk magnetisation vector to tilt away from the z-axis and precess in a cone-like fashion.[12]

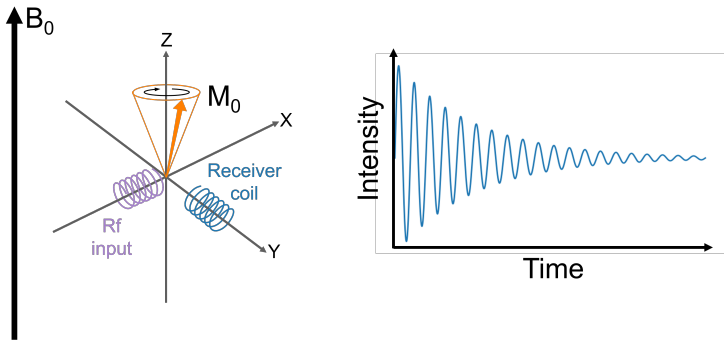

Figure 2.7: Diagram showing the effect of the radiofrequency pulse along the x-axis, and the free induction decay signal seen at the y-axis as a result of the relaxation of M_0.

The re-oriented M_0 emits a radiofrequency signal and induces a current in the receiver coil at the y-axis, which is detected and amplified. This displays a sine wave with decreasing magnitude as the relaxation of M_0 back to the z-axis (the direction of $\boldsymbol{B}_0$) occurs. This is known as free induction decay, FID. The absorbed radiofrequency energy can be emitted by two relaxation modes: spin-spin relaxation and spin-lattice relaxation, both of which contribute to the width and pattern of the absorption peaks.[13] In general, the longer the relaxation time, the sharper and more intense the final peak will be.

Each unique hydrogen environment in a molecule has a characteristic free induction decay signal. Fourier transform NMR acquires all these resonance frequencies simultaneously by exciting all the proton nuclei with a strong and short Rf pulse. This results in an overlapping signal. A Fourier transformation of this time domain signal, results in an intensity vs. frequency spectrum, with a peak for each unique hydrogen environment.

Each hydrogen environment produces a distinct signal due to local magnetic field differences caused by the surrounding electron densities. Electrons are charged particles so generate their own effective magnetic field when in the static magnetic field, $\boldsymbol{B}_0$, reducing its effect. An area of high electron density within a molecule will provide more shielding to the target nucleus, this leads to a lower effective magnetic field strength and thus a lower frequency. Shielded environments move signals to the right in the frequency domain, or upfield, whilst deshielded nuclei are shifted downfield. The variation in frequency observed due to shielding, or lack thereof, is known as chemical shift, δ.

Typically NMR signals are compared to that of an internal standard. Tetramethyl silane, $Si(CH_3)_4$, is often used because the carbons and protons are all in the same highly shielded environment, thus a single high intensity signal is observed. This is defined as 0 Hz.[15] Since the difference in magnetic field strength required to invert the spin of disparate hydrogen nuclei is on the order of 10^{-6} we can convert to the delta scale (equation 2.9) and apply units of parts per million, ppm. The scale also allows us to compare between NMR spectrometers of different frequencies.

$$\delta = \frac{\nu_{\text{sample}} - \nu_{\text{reference}}\ (\text{Hz})}{\text{frequency of the spectrometer (MHz)}} \tag{2.9}$$

NMR was used in chapter 3 of this thesis for the identification and quantification of the liquid products of electrochemical CO_2 reduction.

2.3 Gas Chromatography

Gas chromatography is an analytical technique that separates components of fluid mixtures based on retention coefficients, Figure 2.8. In contrast to other chromatography techniques, the mobile phase in gas chromatography does not interact with the stationary phase. The mobile phase is a dry, inert carrier gas, in our case argon, which flows through the system, pushing the sample through the stationary phase columns. Compounds within the injected sample with a greater affinity for the stationary phase spend longer in the columns, eluting after more time, and therefore are detected after a longer retention time. Affinity can be driven by many factors depending on the column installed, these include inter-molecular interactions, polarity and analyte size.[16] The columns are

contained within an oven to maintain the temperature and ensure consistent separation conditions. Two different column types and a series of valves were implemented in our gas chromatograph to reduce overall runtime whilst maintaining effective separation of our target molecules.

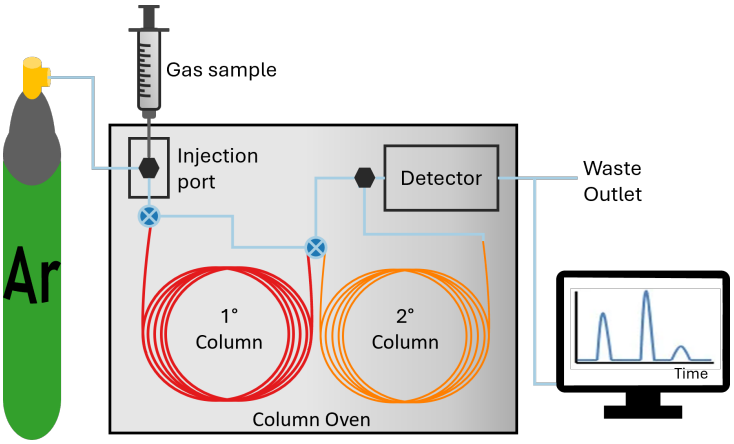

Figure 2.8: Diagram showing the key components of the gas chromatograph.

The gas chromatograph used in this work uses a thermal conductivity detector (TCD). This employs a set of filaments to compare the thermal conductivity of the separated gases exiting the columns and the pure carrier gas. The signal plotted is proportional to the difference in thermal conductivity of the analyte and the carrier gas, and the amount of the analyte.[16] The detector signal is plotted as a function of time such that each analyte appears as a symmetrical Gaussian peak at a specific time. Pure calibration gases were used to determine the retention time of each compound in our gas chromatograph. A calibration graph of peak area and known injection amount can then be used to determine the amount of each analyte in a given mixture.

Gas chromatography was used for gas product identification and quantification in chapters 3 and 4.

2.4 Scanning Electron Microscopy/Energy Dispersive X-ray Spectroscopy

Scanning electron microscopy (SEM) produces high resolution images of a sample's surface. An optical microscope has a theoretical resolution limit of about 200 nm given the average wavelength of visible light is 500 nm. Thus, to increase the resolution a different source is required. A focused beam of electrons, overcomes this due to its shorter wavelength, resulting in resolutions between 1 and 20 nm.[17]

A diagram of a typical scanning electron microscope is shown in Figure 2.9. Under vacuum, electrons are generated at the electron gun, commonly a tungsten filament. The electrons are then focused into a beam by passing through the positively charged anode. The beam size is determined by passing it through a series of condenser lenses. The size of the beam determines the resolution of the image. Scanning coils are then used to direct the beam in the x and y directions across the sample. A raster pattern, moving from left to right in lines from top to bottom across the target area is used to build the image pixel by pixel.[18]

Upon interaction with the sample the electrons generate several reciprocal responses that can be detected. Backscattered electrons are reflected back towards the scanning coils as the beam hits the sample. These elastic interactions are detected and produce compositional images, where higher contrast pertains to a higher atomic number. Secondary electrons result from inelastic interactions and are emitted from excited atoms within the sample.[19] The images generated from the detection of secondary electrons are topographical, with height being depicted by different contrast levels.

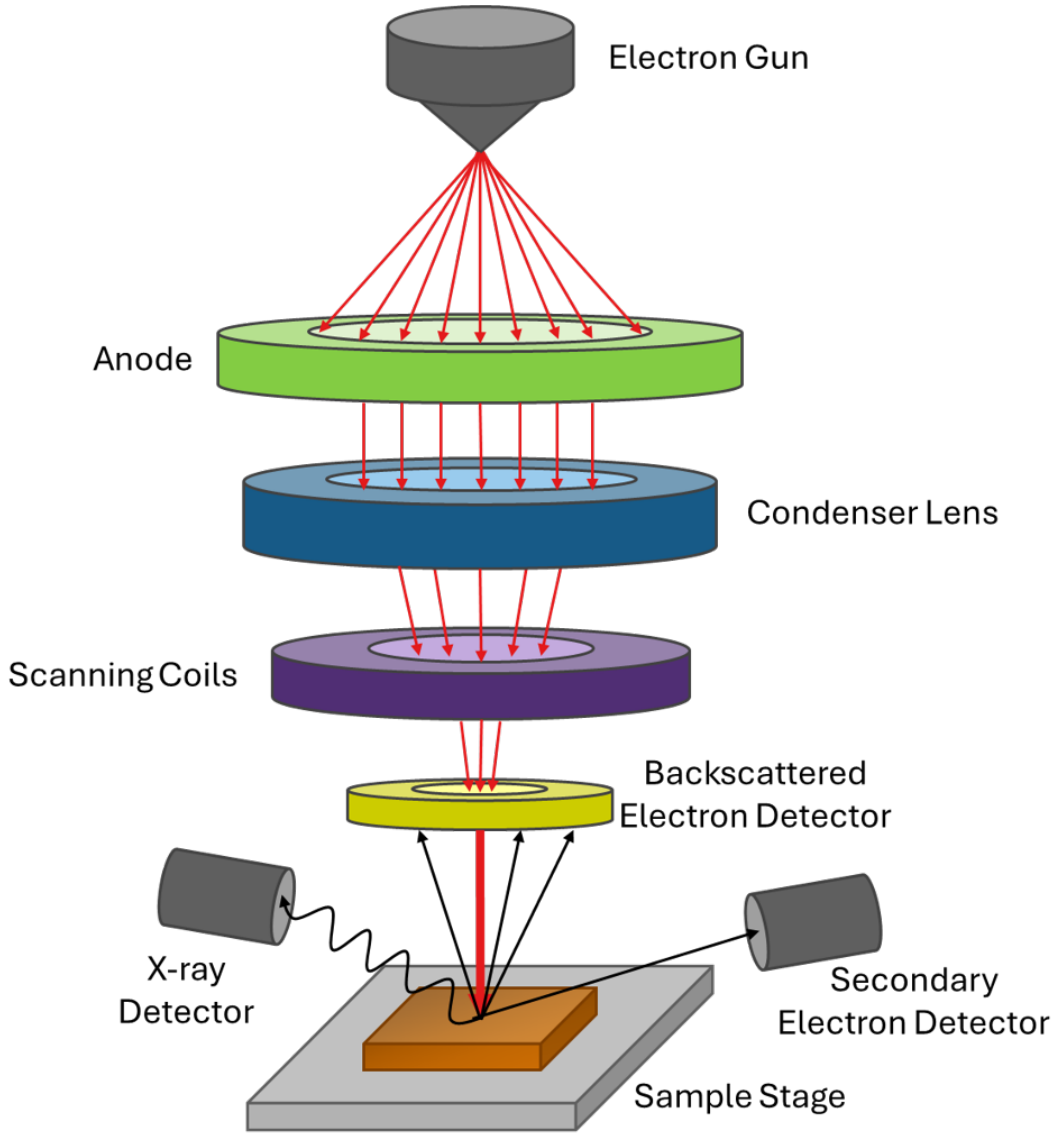

Figure 2.9: Diagram of a scanning electron microscope.

Some SEM systems are also able to complete energy dispersive X-ray (EDX) analysis and overlay this onto the images generated. After excitation from the electron beam, an electron from the nucleus is ejected leaving an electron hole. This hole is then filled by a higher energy outer shell electron, resulting in the release of a characteristic X-ray.[20] Since all elements have a unique X-ray emission spectrum[21] these can be detected and deconvoluted to measure the concentration of a given element present. Thus energy dispersive X-ray analysis can be used to analyse and portray the segregation and location of elements within the sample view. Elements with an atomic number between boron and californium can be detected at a 0.1 % concentration or higher.[20] SEM/EDX spectroscopy was used in chapters 3 and 4 to investigate the morphology of the synthesised catalysts.

2.5 Transmission Electron Microscopy

2.5.1 The Transmission Electron Microscope

Transmission electron microscopy (TEM) employs a beam of high energy electrons transmitted through a thin sample to investigate the internal structure and chemistry. The technique is similar to SEM in that electrons are used to avoid the resolution and diffraction limits that occur when using optical microscopy as defined by the wavelengths of visible light. In contrast to SEM, the images recorded are a result of the electron flux after it has passed through the sample.[22] This results in a variety of signals after the sample including inelastically and elastically scattered electrons, as well as those which are seen in SEM such as, characteristic X-rays, secondary electrons and backscattered electrons.[23]

A diagram of a standard transmission electron microscope is shown in Figure 2.10. An electron beam is generated at the electron gun under vacuum which is then focused and manipulated through a series of magnetic lenses. Magnetic lenses are able to bend and focus the electron beam as electrons have charge and thus can be deflected by a magnetic field. The lenses consist of a copper coil surrounding a pole piece with a small air gap; current is passed through the coils generating a magnetic field with a focusing effect, the strength of which is dependant on the current passed.[24] The gap allows the field to be concentrated and shortens the focal length of the lens.[24] The microscope also contains apertures, which limit the beam diameter, the sample holder, the viewing screen, and detectors.

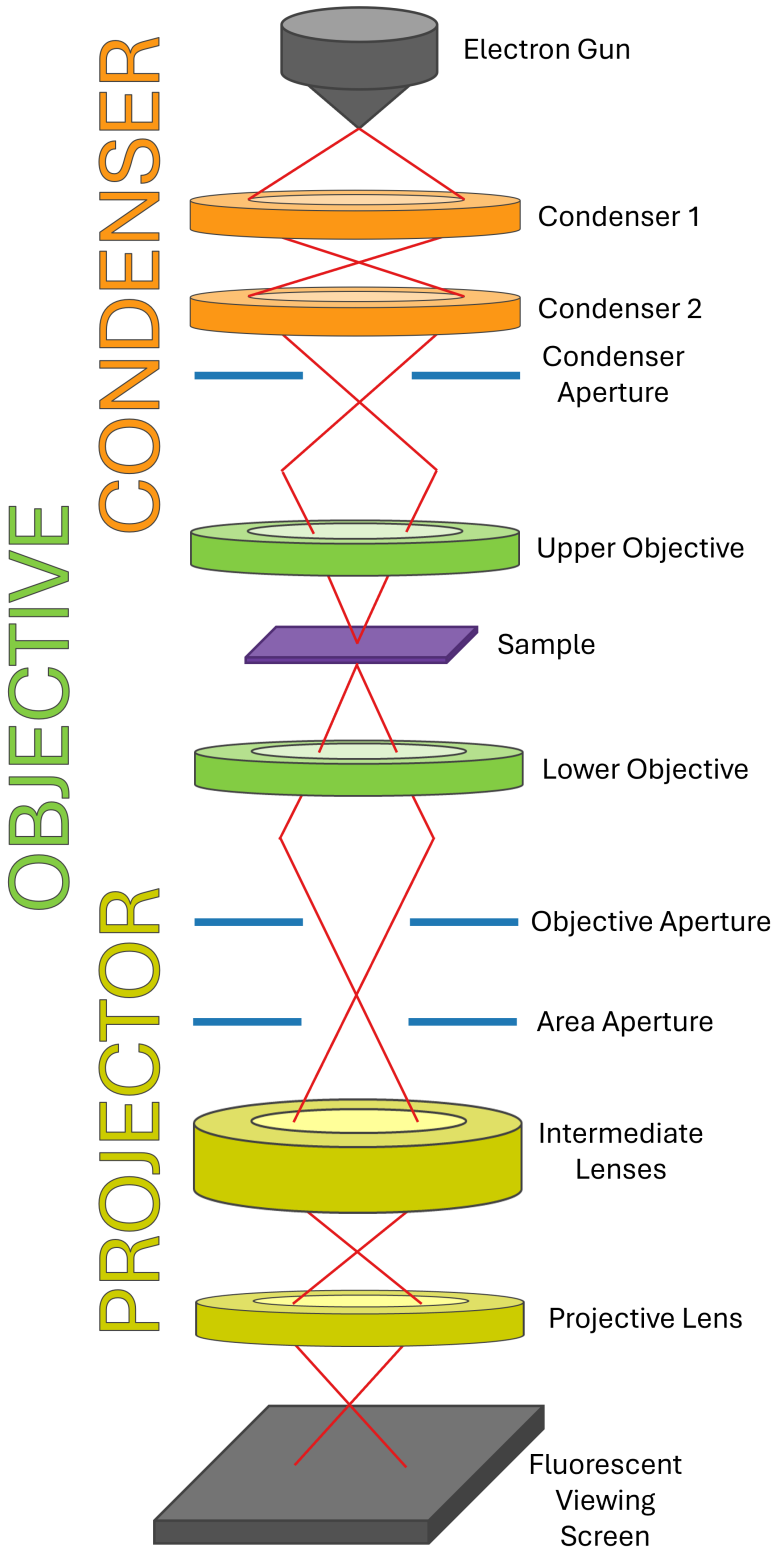

Figure 2.10: A simplified diagram of a transmission electron microscope.[25,26]

The electron beam first passes through a series of condenser lenses. The first condenser lens collimates the beam, controlling its size, and the second controls the convergence angle of beam.[25] The objective lenses before and after the sample stage are said to be the most important lenses in the TEM.[23] The first focuses the beam onto the sample, and the second forms the initial inverted image from the sample. The intermediate lenses then magnify this initial image before it is projected onto the viewing screen by the projective lens.

2.5.2 Imaging and Spectroscopic Analysis

Several different types of analysis can be conducted using TEM depending on which electron interactions are measured. The principal forms of scattering that occur are elastic (immeasurable energy loss) and inelastic (measurable yet small, relative to the beam, energy loss).[23] Elastic scattering is primarily a result of the interaction between the incoming electron beam and atomic nuclei. Inelastic scattering, however, is a result of the interaction of the electron beam with other electrons in the sample; this can then be exploited for analysis such as electron energy-loss spectroscopy (EELS) and EDX spectroscopy. Since both diffracted and transmitted electrons can be detected by TEM, parameters and apertures can be used to produced different kinds of images. Bright field imaging uses only the transmitted beam and diffracted regions of the sample appear dark, whereas dark field imaging detects only a diffracted beam which appears as bright on the resultant image.[25]

In this work, Scanning transmission electron microscopy (STEM) was used. In this set-up the electron beam is converged and rasters across the sample in contrast to viewing the entire sample at once. Bright field images were collected as described above however a high angle annular dark field (HAADF) detector was employed to detect inelastically scattered electrons at high angles.[27] Here, the scattering angle depends on the size of the atomic nucleus, thus higher atomic number elements are scattered at higher angles and appear brighter in the final image compared to light atoms.[23,27]

Energy dispersive X-ray analysis can be completed on a TEM sample in a similar way to in SEM, such that the specimen can be elementally mapped according to the characteristic X-rays detected.[23] However, in TEM electron energy-loss spectroscopy (EELS) can be used such that the reliance on emitted X-rays is eliminated. EELS allows the detection and quantification of all the elements in the periodic table, the ability for analysis of low Z number elements is particularly lauded. Yet, the best results are produced from extremely thin specimens for which preparation is tedious, requiring a sample thinning process by ion-bombardment.[22] This means there is still a need for X-ray analysis for some samples.

EELS detects any loss of energy by incident electrons; the energy loss measured is primarily caused by inelastic interactions within the core shells of atoms. The spectrometer would be located at the bottom of the TEM column, after what is shown in Figure 2.10. The spectrometer separates the electrons based on their energy, allowing the energy loss to be plotted against frequency. The resultant spectrum contains the zero-loss peak, a peak of extreme magnitude which represents all the non-scattered and elastically forward scattered electrons.[23] The remainder of the low-loss region follows, containing plasmon peaks and interband transitions, these display electron interactions resulting from valence and conduction band electrons in the sample.[23] Energy losses above 50 eV are considered part of the high-energy loss region, from which specific elemental information about the chemical structure and bonding can be extracted.[28] This allows the identification of elements and therefore elemental maps and cross-sectional profiles to be created. In this thesis, TEM imaging and EELS were used in chapter 3 to analyse the catalysts synthesised.

2.6 X-ray Diffraction

2.6.1 X-ray Crystallography Theory

Diffraction is a phenomenon caused by the interaction of a wave with an object in its path; it occurs when the dimensions of the object and the wavelength of the electromagnetic radiation are comparable.[29] Consequently, X-rays can be used to investigate crystal structures. Upon interaction with the plane of a crystal lattice, X-rays will be diffracted at the angle θ which is equal to the incoming, incident angle. As shown in Figure 2.11, a second X-ray beam may interact with the second layer of the crystal lattice. In this schematic an additional wavelength, λ, is travelled by the X-rays that are diffracted at the second layer. This is indicated by distance AB in the incident beam, and BC in the diffracted beam. In the general case we can represent the additional distance travelled by $n\lambda$ and equate this to our AB and BC lengths, equation 2.10.

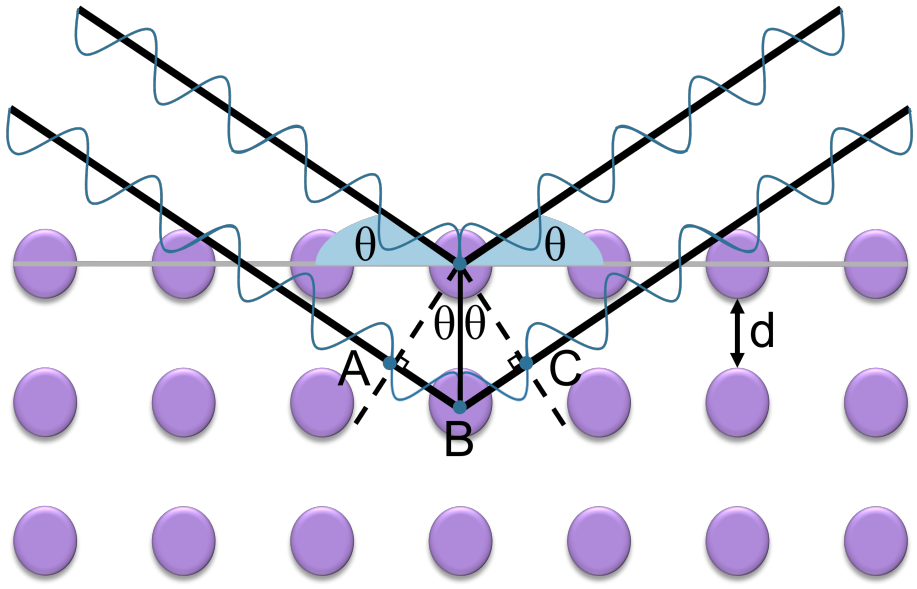

Figure 2.11: A representation of two X-rays being diffracted by a crystal lattice. θ is the angle between the incident rays and the crystal plane. AB and BC show the additional wavelength that the ray must travel to reach the second layer of the lattice.

$$AB + BC = n\lambda \tag{2.10}$$

By using the interplanar spacing, d, and some basic trigonometry we achieve Bragg's law, equation 2.11. When n is an integer value the resulting waves interfere constructively, and thus can be detected and the intensities plotted as a diffraction pattern. When n has a non-integer value, the X-rays interfere destructively and no signal can be detected. This means peaks are only seen in the diffraction pattern when Bragg's law is obeyed.

$$n\lambda = 2dsin\theta \tag{2.11}$$

For a given crystal unit cell only specific angles obey Bragg's law and thus distinct diffraction patterns with peaks at those angles are observed. The θ and peak intensities seen are characteristic of each crystal lattice, allowing compounds, mixtures and phases to be detected.

2.6.2 The X-ray Diffractometer

X-ray diffraction instrumentation consists of three key parts, the X-ray source, the sample holder, and the detector. The sample is irradiated with a monochromatic beam of X-rays typically Cu K_α radiation. This is collimated and aimed onto the sample at the given angle, after diffraction this is then detected and plotted as intensity against 2θ to produce a diffraction pattern.

Within the diffractometer the three components are commonly arranged in one of two configurations as shown in Figure 2.12. This first, Figure 2.12a, has a fixed X-ray source whilst the sample and detector both move, with a ratio of θ:2θ.[30] The other, Figure 2.12b, consists of a fixed sample holder, where the X-ray source and detector each move with a ratio θ:θ.[30] In both instances the distance between the sample and X-ray source, and the sample and the detector remain constant and equal. The former configuration is more common however the latter is especially advantageous if the sample needs to be kept still.

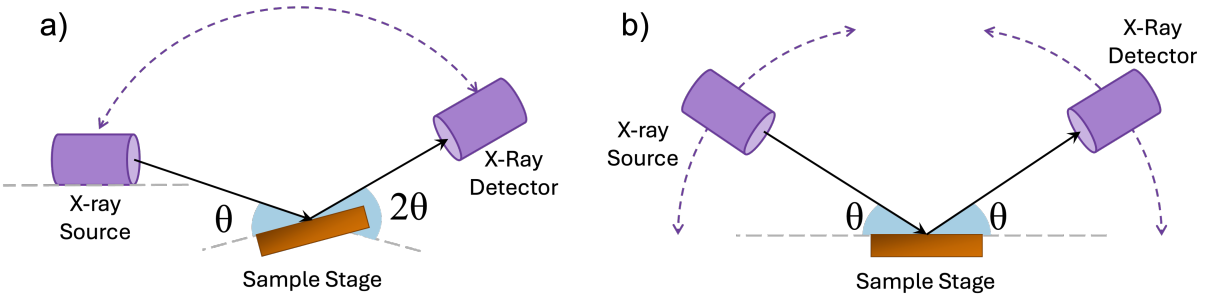

Figure 2.12: A schematic representation of the two most common configurations of an X-ray diffractometer.

Regardless of the configuration, samples are typically ground to a fine powder and spread in a thin layer. This increases the likelihood that every possible orientation of the crystal will be observed. The sample may also be rotated to further increase the randomness of the orientation of the crystals.[31] In this work XRD was used to analyse and confirm the structure of as-synthesised catalysts in chapters 3 and 4.

2.7 X-ray Photoelectron Spectroscopy

X-ray photoelectron spectroscopy (XPS) is based on the photoelectric effect, shown graphically in Figure 2.13. Radiation of a sample surface with an appropriate energy causes the ejection of photoelectrons. Measurement of the kinetic energy, E_k, of these photoelectrons allows for the calculation of their binding energy, E_b, according to equation 2.12, where $h\nu$ is the energy of the incident radiation and Φ is the work function of the material.

$$E_b = h\nu - E_k - \Phi \tag{2.12}$$

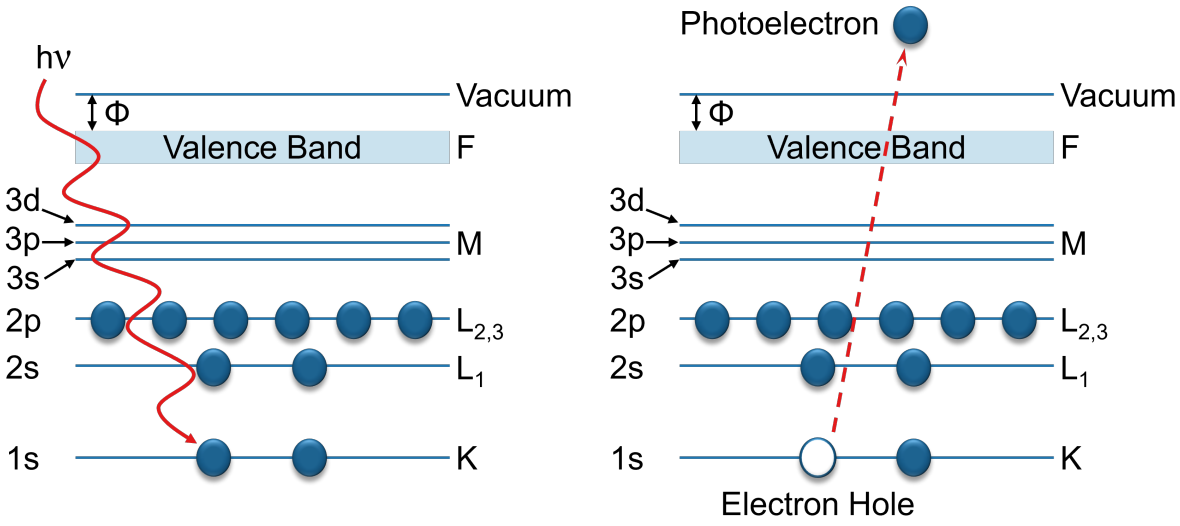

Figure 2.13: A schematic representation of the photoelectric effect.

Soft X-rays (200–1500 eV) are used to irradiate the sample, allowing photoelectrons from the core levels to be expelled. The removal of a core electron leaves behind an electron hole. This is highly unstable and so is readily filled by an electron from a higher energy level. This causes a release of energy either as X-ray fluorescence or an Auger electron, whereby the energy is transferred to a secondary outer shell electron giving it enough energy to be ejected from the atom. The kinetic energy of the photoelectron is measured at the detector and related to the electron binding energy; this allows determination of the element and its environment, as they are characteristic.

The monochromatic X-ray beam is commonly sourced from either Mg K_α, $h\nu$ =1.25 KeV, or Al K_α, $h\nu$ =1.49 KeV. Electrons are emitted from the surface of the specimen at depths of between 3 and 10 nm. Considering 1 nm is equivalent to 3 or 4 atomic layers,[32] this allows for analysis of surface oxides and adsorbates that would not be seen by bulk spectroscopy techniques.

XPS spectra are plotted in terms of energy against intensity. Often plots are in terms of binding energy, however since this can shift depending on the X-ray source used, it is important that the source is always specified. Peak locations are compared to tabulated databases of elements and their oxidation states. Peaks are deconvoluted to allow for the measurement and comparison of different surface oxides and impurities. XPS is often used to investigate the surface of catalysts before and after use to monitor their degradation.

In this thesis XPS is used to analyse the surface of synthesised catalyst stacks in chapters 3 and 4.

2.8 References

[1] T. J. Smith and K. J. Stevenson, in *Handbook of Electrochemistry*, ed. C. G. Zoski, Elsevier, Amsterdam, 2007, pp. 73–110.

[2] F. Barbir, *Solar Energy*, 2005, **78**, 661–669.

[3] Z. Li, X. Chen, J. Yuan, Y. Qiao, R. Dai, X. Wang, X. Li, J. Ma and Z. Wang, in *Electrochemical Membrane Technology for Water and Wastewater Treatment*, ed. Z. Wang, K.-H. Choo, C. Y. Tang and T. D. Waite, Elsevier, 2022, pp. 81–110.

[4] C. Spiegel, *An Introduction to Cation Exchange Membranes*, `https://www.fuelcellstore.com/blog-section/blogart94`.

[5] K. A. Mauritz and R. B. Moore, *Chemical Reviews*, 2004, **104**, 4535–4586.

[6] N. Elgrishi, K. J. Rountree, B. D. McCarthy, E. S. Rountree, T. T. Eisenhart and J. L. Dempsey, *Journal of Chemical Education*, 2018, **95**, 197–206.

[7] P. Zanello and R. S. of Chemistry (Great Britain), *Inorganic electrochemistry: theory, practice and application*, Royal Society of Chemistry, Cambridge, 2003.

[8] P. T. Kissinger and W. R. Heineman, *Journal of Chemical Education*, 1983, **60**, 702.

[9] T. J. Davies, R. R. Moore, C. E. Banks and R. G. Compton, *Journal of Electroanalytical Chemistry*, 2004, **574**, 123–152.

[10] A. J. Bard, L. R. Faulkner and H. S. P. o. c. White, *Electrochemical methods: fundamentals and applications*, John Wiley & Sons, Ltd, Hoboken, NJ, USA, Third / Allen J. Bard, Larry R. Faulkner, Henry S. White. edn., 2022.

[11] D. Voiry, M. Chhowalla, Y. Gogotsi, N. A. Kotov, Y. Li, R. M. Penner, R. E. Schaak and P. S. Weiss, *ACS Nano*, 2018, **12**, 9635–9638.

[12] J. Keeler, *Understanding NMR Spectroscopy*, Apollo - University of Cambridge Repository, 2002.

[13] M. Balci, in *Basic 1H- and 13C-NMR Spectroscopy*, ed. M. Balci, Elsevier Science, Amsterdam, 2005, pp. 9–24.

[14] G. Webb, in *Encyclopedia of Spectroscopy and Spectrometry (Third Edition)*, ed. J. C. Lindon, G. E. Tranter and D. W. Koppenaal, Academic Press, Oxford, Third Edition edn., 2017, pp. 274–283.

[15] R. J. Ouellette and J. D. Rawn, in *Organic Chemistry (Second Edition)*, ed. R. J. Ouellette and J. D. Rawn, Academic Press, Second Edition edn., 2018, pp. 427–461.

[16] O. D. Sparkman, Z. E. Penton and F. G. Kitson, in *Gas Chromatography and Mass Spectrometry (Second Edition)*, ed. O. D. Sparkman, Z. E. Penton and F. G. Kitson, Academic Press, Amsterdam, Second Edition edn., 2011, pp. 15–83.

[17] SciMed, *A Brief Introduction to SEM (Scanning Electron Microscopy)*, `https://www.scimed.co.uk/education/sem-scanning-electron-microscopy/`.

[18] R. F. Egerton, in *The Scanning Electron Microscope*, Springer US, Boston, MA, 2005, pp. 125–153.

[19] M. Rösler and W. Brauer, *physica status solidi (b)*, 1981, **104**, 575–587.

[20] M. Abd Mutalib, M. Rahman, M. Othman, A. Ismail and J. Jaafar, in *Membrane Characterization*, ed. N. Hilal, A. F. Ismail, T. Matsuura and D. Oatley-Radcliffe, Elsevier, 2017, pp. 161–179.

[21] N. M. Pirozzi, J. Kuipers and B. N. Giepmans, in *Correlative Light and Electron Microscopy IV*, ed. T. Müller-Reichert and P. Verkade, Academic Press, 2021, vol. 162 of Methods in Cell Biology, pp. 89–114.

[22] G. W. Stachowiak, A. W. Batchelor and G. B. Stachowiak, in *Experimental Methods in Tribology*, ed. G. W. Stachowiak, A. W. Batchelor and G. B. Stachowiak, Elsevier, 2004, vol. 44 of Tribology Series, pp. 165–220.

[23] D. B. Williams and C. B. Carter, *Transmission Electron Microscopy*, Springer US, 2009.

[24] G. Tatlock, in *Introduction to Electron Optics*, ed. R. Brydson and S. Brooks, John Wiley & Sons, Ltd, 2011, ch. 2, pp. 21–38.

[25] K. Holsgrove, *Ph.D. thesis*, Queen's University Belfast, 2017.

[26] R. B. Cummings, *Ph.D. thesis*, University of Glasgow, 2023.

[27] M. Tanaka, *Glossary of TEM Terms*, `https://www.jeol.com/words/emterms/`, Created by JEOL Ltd.

[28] B. Fultz and J. M. Howe, *Transmission Electron Microscopy and Diffractometry of Materials*, Springer Berlin, 2008.

[29] P. Atkins, J. de Paula and R. Friedman, *Physical Chemistry: Quanta, Matter, and Change*, Oxford University Press, 2023, pp. 330–343.

[30] R. Jenkins and R. L. Snyder, *Introduction to X-ray Powder Diffractometry*, Wiley, 1996, vol. 138, pp. 178–187.

[31] D. A. Skoog, F. J. Holler and S. R. Crouch, *Principles of instrumental analysis*, Thomson Brooks/Cole, Belmont, Calif, 6th edn., 2007.

[32] P. Van der Heide, *X-ray photoelectron spectroscopy: an introduction to principles and practices*, Wiley-Blackwell, Hoboken, N.J, 2012.

Chapter 3

NiCuAg: An Electrochemically-Synthesised Trimetallic Stack for CO_2 Reduction

Published as "NiCuAg: An Electrochemically-synthesised Trimetallic Stack for CO_2 Reduction." H. L. A. Dickinson, M. D. Symes, Electrochemica Acta, 2024, 493, 144355.

Acknowledgements and Declarations

Thanks go to Dr Liene Spruzeniece at the Geoanalytical Electron Microscopy and Spectroscopy (GEMS) facility in the School of Geographical and Earth Sciences, University of Glasgow for scanning electron microscopy. Thanks go to the Kelvin Nanocharacterisation Centre (KNC) in the School of Physics and Astronomy, University of Glasgow for cross-sectional transmission electron microscopy and analysis completed by Dr Kayla Fallon and Dr Sam McFadzean, and lamella fabrication by Mr William Smith. Thanks go to Dr Steve Francis at the University of St. Andrews for X-ray photoelectron spectroscopy and the subsequent deconvolution of the high resolution spectra.

Abstract

Electrochemical CO_2 reduction is a promising technique for the production of desirable hydrocarbons without the need to resort to fossil resources. However, high overpotentials and poor selectivity remain a challenge for CO_2 electroreduction, especially for deep reduction by more than two electrons. One apparently attractive approach for breaking the scaling relations caused by simultaneous CO_2 reduction pathways and for achieving deeper reduction is the use of multi-metallic electrodes, where several promising metal catalysts are present in close proximity. Herein, noting the activity shown by Ni, Cu and Ag for CO_2 electroreduction when used individually, we set out to synthesise a trimetallic "stack" catalyst, NiCuAg, and then to test this for electrochemical CO_2 reduction. The stack architecture was successfully generated and the trimetallic NiCuAg system did show improved Faradaic efficiency for the reduction of CO_2 to formic acid when compared to the bare Ni and bimetallic NiCu controls under some select conditions. However, the two-layer NiCu stack and bare Ni exhibited consistently higher Faradaic efficiencies than NiCuAg for deeper CO_2 electroreduction to methanol and ethanol, indicating that the combination of three individually promising metals does not necessarily translate into superior catalytic performance for deep carbon dioxide reduction.

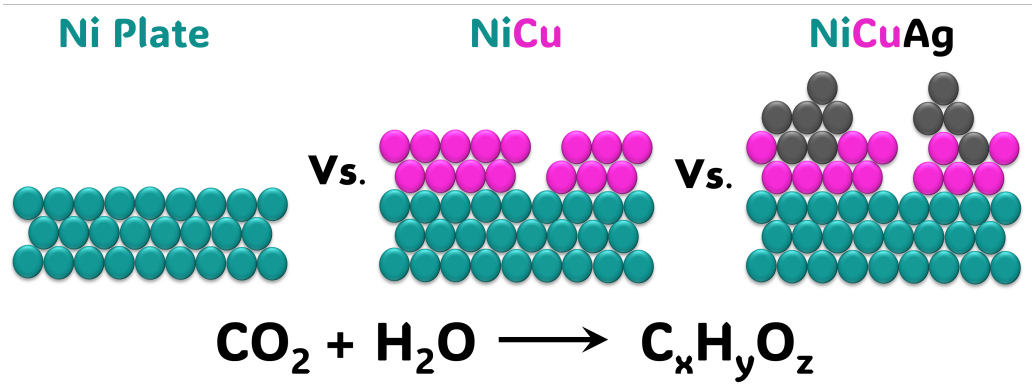

3.1 Introduction

Increased levels of carbon dioxide in the atmosphere compared to before the industrial revolution have led to intensified research into more sustainable energy and feedstock sources, to prevent further increases in emitted CO_2.[1–3] This atmospheric CO_2 can provide a useful feedstock for the storage of excess renewably-generated energy.[4–7] The electroreduction of CO_2, powered by renewables, has been suggested as a means of closing the carbon gap[8] whilst producing desirable, economically viable chemical feedstocks.[9] At least sixteen carbon products, including carbon monoxide, formic acid, methane, ethylene, and ethanol are commonly formed by electrochemical CO_2 reduction;[10] however, since the reaction is typically performed under aqueous and ambient conditions, hydrogen evolution is always a competing process.[11,12] This wide product range and competitive hydrogen evolution leads to poor selectivity and low energy efficiency.

Metal electrocatalysts have been a significant focus since Hori's seminal discovery that Cu can reduce CO_2 by more than two electrons to produce hydrocarbons.[13] Since CO_2 reduction proceeds via many simultaneous pathways[14,15] (wherein the reaction intermediates are approximately linearly related),[16] these scaling relations must be broken to achieve a high selectivity for a given product at a low overpotential. Thus, methods such as tethering, ligand stabilisation, mixed metal phases and alloying have been employed.[17] These are beneficial methods for directing morphology and composition and, accordingly, geometric and electronic environments.[18] Bimetallic catalysts, particularly those containing Cu, have garnered significant interest as they potentially allow two different metal sites to be in close proximity to a single reacting absorbate;[18–25] conversely, reported examples of trimetallic electrocatalysts for CO_2 reduction are much rarer. The interaction of these neighbouring active sites has been suggested to create what is termed a synergistic effect, whereby the activity of the combination of metals is mutually reinforced and thus greater than the sum of the activities of the separate components.[26] The term synergistic effect appears to have first been used in relation to CO_2 reduction by Watanabe *et al.*[27] upon

the discovery that Cu-Ni alloys produced methanol as a CO_2 reduction product whilst the individual metals did not. Despite the development of electroreduction and detection systems that have disproven the effect in this case, the term is still employed.[22] Apparent synergies can often be explained by one of the following influences:[22,28] (a) the promotion of desorption by dipole repulsion from the secondary metal,[29] (b) a bifunctional mechanism[30–32] whereby the secondary metal can stabilise an intermediate for reaction at the primary metal, and (c) spillover[33–35] wherein the close proximity of the metal active sites allows an excess of one intermediate to be produced (for example CO), leading to an increase in local concentration of that intermediate for further reduction on the other metal active sites.

In 2022 Zhu *et al.*[35] developed a AuAgCu heterostructure using a multi-step seed-mediated growth method to form a Au core encapsulated by Ag. Cu was selectively deposited on one side of the nanorod to give an asymmetric nanostructure. CO_2 reduction tests resulted in a Faradaic efficiency towards ethanol of 38% at -0.8 V vs. reversible hydrogen electrode (RHE). This enhanced activity was attributed to the promotion of C−C coupling at Cu sites. The catalysts' asymmetric design allowed for a CO spill-over process to occur, whereby weakly-bound CO was released from the Au and Ag sites, increasing the local concentration at the Cu sites to allow for C−C coupling.

Chaitree *et al.*[36] synthesised a Cu−Ni−Sn electrocatalyst on Pd-activated carbon fabric by electroless deposition. Testing in an H-cell showed decreased activity towards H_2 production compared to the other bi/monometallic catalysts that were tested; whilst a Faradaic efficiency of 12% towards acetone was claimed at -1.6 V vs. Ag/AgCl. The total Faradaic efficiency for C_{2+} products, including ethylene glycol, acetate, ethanol, 1-butanol, and acetone, was 37%.

Zhang *et al.*[37] assembled a Cu–Zn–Al layered double hydroxide electrocatalyst. CuZn alloys and CuZn aluminate oxides were stacked in alternating layers. The intention was to create many active sites by generating strong electronic interactions between the three metals in different oxidation states. The layered system achieved a Faradaic efficiency of 89% towards C_{2+} products in a flow-cell reactor at −1.15 V vs. RHE. This included Faradaic efficiencies of over 30% respectively for both ethylene and ethanol.

Herein we report an electrochemically synthesised trimetallic stack for CO_2 reduction, NiCuAg. We define "stack" here as being sequentially-coated metal layers. A multi-metal layered design was chosen to attempt to break the typical linear scaling relations seen in single metal CO_2 electroreduction catalysts. Previous studies have shown the combination of Cu and Ni to be promising. Zhang *et al.* achieved a Faradaic efficiency of 62% for C_{2+} products at −0.88 V vs. RHE with a Ni–Cu nanowire catalyst.[38] Similarly, Suzuki *et al.* developed a Cu–Ni nanoparticle catalyst that achieved a 35% Faradaic efficiency for C_2 products at −1.2 V vs. RHE.[39] Ag was added to our catalyst as a final layer inspired by Choi *et al.*, where it was found that the addition of Ag promoted CO binding on Cu sites, allowing reduction to methane at a 72% Faradaic efficiency at −1.17 V vs. RHE.[40]

It is generally accepted that single metals fall into several groups when used for the electrochemical reduction of CO_2.[41,42] Metals with a high H affinity (Fe, Ni, Pd, Pt) primarily produce hydrogen and are not active towards CO_2 reduction. Metals which coordinate CO strongly to produce CO (Ag, Au, Zn) form another group, and those which produce formic acid (Cd, In, Sn) are another. Cu, which has moderate (intermediate-strength) binding and thus can produce methane as well as products that require C–C coupling, is often given its own category.[41] Ni, Cu and Ag were chosen for our catalyst based on these groupings: Ni, for its high H affinity and good proton transfer ability; Cu, for its C–C coupling and further reduction ability; and Ag for its CO coordination ability. Despite the fact that Ni is typically associated with increased hydrogen evolution activity,[43,44] it has been shown that nickel based catalysts have the ability to promote C–C coupling.[45]

Indeed a Ni-Al catalyst was one of the first Cu-free electrocatalysts to be shown to produce C_2 and C_3 products by CO_2 reduction.[46] More generally, it has been suggested that the combination of additional metals with Ni would help to overcome the non-desirable features of pure Ni metal, such as CO poisoning and nanoparticle sintering.[45,47]

Our hypothesis was therefore that a synergistic effect and improved selectivity for C_{2+} products would be observed at lower potentials by combining the metals Cu, Ni and Ag. This hypothesis was based on the idea that CO_2 would firstly be reduced to CO on the Ag metal through well-studied mechanisms,[48–51] and would then spill over onto Cu sites for further reduction to C_{2+} products. The Ni was incorporated both for its own C−C bond forming ability, and also for its high affinity for H atoms, which we postulated might facilitate the hydrogenation of the C_{2+} products formed on the adjacent copper sites to give highly-reduced multi-carbon products.

We used a sequential synthesis approach to produce active sites in which all three metals would be present at the surface and exposed to the electrolyte.[39,40] However, our results suggest that there is no evidence for significant beneficial synergism by combination of these metals, with a bimetallic mixture of Ni and Cu displaying similar activity for methanol and ethanol production to an Ni cathode, and both of these displaying significantly better performance than the trimetallic NiCuAg material. Clearly then, not every combination of promising metals leads to improved selectivity for deep CO_2 electroreduction activity.

3.2 Experimental

3.2.1 Materials

Nickel foil (0.25 mm, [7440-02-0], annealed, 99.5 %), copper (II) sulfate ([7758-98-7], anhydrous, 98%), and potassium hydrogen carbonate ([298-14-6], 99%) were obtained from Alfa Aesar. Silver nitrate ([7761-88-8], ACS reagent, >99%) was obtained from Sigma Aldrich. Nafion-117 membranes were obtained from Fuel Cell Store. Carbon Dioxide (99.8%, Industrial Grade) and Argon (99.9%) were supplied by BOC Limited. All chemicals were used as received without further purification and all solutions were produced using ultrapure water (15.8 MΩ-cm).

3.2.2 Catalyst Preparation

Nickel foil was cut to a size of 2 × 1 cm and the backside covered using Sellotape. This was used as the working electrode. The Ni surface was cleaned prior to any coating by sonication for 10 minutes each in: acetone, followed by isopropyl alcohol and finally deionised water. Copper electrodeposition (from a solution of 0.1 M $CuSO_4$ at −200 mV vs. Ag/AgCl) was completed in an open beaker for 10 minutes whilst stirring. For copper deposition, a standard three-electrode setup was used: leak-free Ag/AgCl reference electrode (Innovative Instruments, Inc.), Ni foil working electrode, and graphite rod (Alfa Aesar) counter electrode. Where appropriate, a silver layer was added by galvanic replacement by placing the NiCu stack in a 0.01 M $AgNO_3$ solution for two minutes, without stirring, to give NiCuAg. All catalysts were prepared at room temperature and pressure.

3.2.3 Characterisation

The surface morphology of the prepared electrocatalyst plates was analysed in the Geoanalytical Electron Microscopy and Spectroscopy (GEMS) facility at the School of Geographical and Earth Sciences, University of Glasgow, using a Carl Zeiss Sigma variable pressure analytical Scanning Electron Microscope (SEM) with Oxford Microanalysis with a 15 kV accelerating voltage. A 20 nm thick carbon layer was coated onto the samples prior to analysis. Cross-sectional Transmission Electron Microscopy (TEM) was completed at the Kelvin Nanocharacterisation Centre. A cross-sectional TEM lamella was extracted from the bulk sample and transferred onto a Cu TEM grid using a FEI Nova NanoLab 200 dual beam SEMFIB. The TEM imaging and analysis was done on a JEOL Atomic Resolution Microscope (JEM-ARM200cF) STEM, operating at 200 kV. This microscope is equipped with a cold field emission gun and a Corrected Electron Optical Systems GmbH probe corrector for STEM imaging and a Gatan GIF Quantum electron spectrometer for electron energy-loss spectroscopy (EELS).

X-ray diffraction (XRD) was undertaken using a Rigaku MiniFlex benchtop diffractometer equipped with Cu sealed tube X-ray source. The surface composition of the catalysts was analysed by X-ray photoelectron spectroscopy (XPS) at the University of St Andrews using a Scienta 300 with a SPECS monochromated X-Ray source. All data analyses and fittings were made using CasaXPS software.

3.2.4 Electrochemical Characterisation

Electrochemical studies were controlled by a Gamry interface 1010E potentiostat, at room temperature and pressure. Linear sweep voltammograms and electrochemical CO_2 reduction experiments were carried out in a custom-made air-tight two-compartment H-cell (Figure 3.1) under a constant flow of Ar or CO_2 at 0.1 L min^{-1}. A graphite rod and

leak-free Ag/AgCl electrode were used as the counter and reference electrodes respectively. A Nafion-117 membrane was added to separate the anolyte and catholyte, alongside preventing the diffusion and re-oxidation of any reduction products. 0.1 M $KHCO_3$ was used as the electrolyte; it was purged with CO_2 or Ar gas at 0.1 L min^{-1} for at least 30 minutes prior to testing. Linear sweep measurements were taken between +0.2 and −2.0 V vs. Ag/AgCl with a scan rate of 25 mV/s.

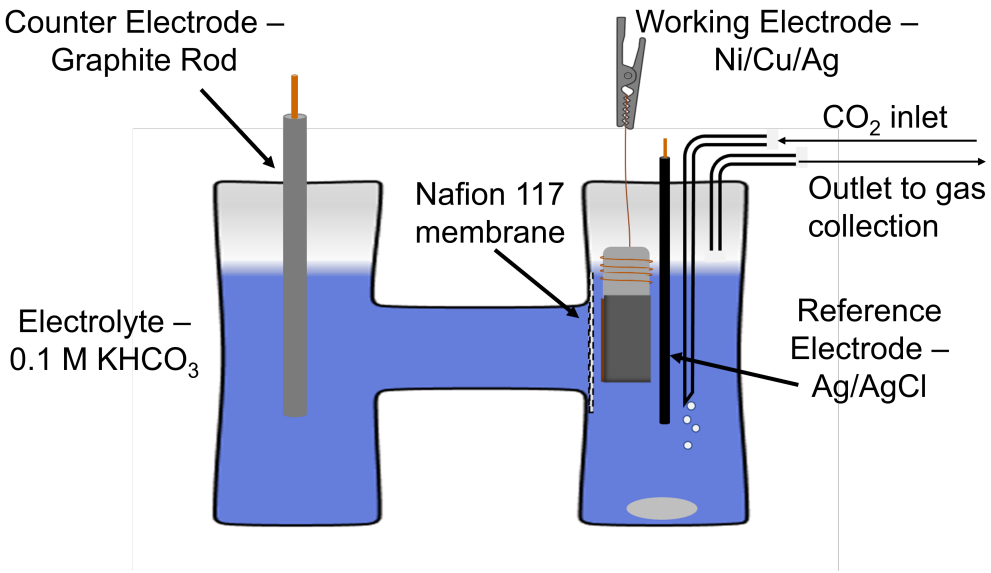

Figure 3.1: Custom air-tight H-cell set-up, as used for electrochemical CO_2 reduction tests.

3.2.5 Product Analysis

3.2.5.1 Gas Product Analysis

Throughout the bulk electrolysis the solution was stirred and flushed with CO_2. The flow of CO_2 acted as a medium to push any unreacted CO_2 alongside the gas products generated into a gas sampling bag. Electrolysis was ended once the sampling bag had reached capacity (2 L). The gases were analysed post-electrolysis by gas chromatography (Agilent 8860) equipped with 2 Porapak Q columns and a MoleSieve 13X column. A thermal conductivity detector was used and argon employed as the carrier gas. Each sample (1 mL) was introduced to the gas chromatograph, GC, by direct manual injection.

The GC was calibrated using a commercial gas mixture containing the possible CO_2 reduction products at given percentages (H_2–5.07%; CO–1.00%; CH_4–0.203%; C_2H_6–0.152% and C_2H_4–0.252%) and argon as a balance. The gas mixture was supplied by CK Isotopes Limited. An example chromatogram is shown in Figure 3.2. The red line shows the expected retention times of each peak in the calibration gas mixture, however, since our setup flushes the system with CO_2, the signals seen were more similar to that shown by the blue trace. To combat the CO_2 flushing, an alternate calibration gas consisting of 2% the original gas mixture and a balance of CO_2 was used for our calibration. This meant that the peak areas observed in the calibration were in a similar range to those observed after electrolysis. Consequently, the C_2H_6 and C_2H_4 peaks are no longer seen as they exist in too low a concentration to reach the detection limit of the GC. Peak areas of below 0.4 and 0.5 were deemed indistinguishable from the background trace for CH_4 and CO, respectively. Thus it is possible that both CO and CH_4 could have been produced at levels below the detection limit of this set up.

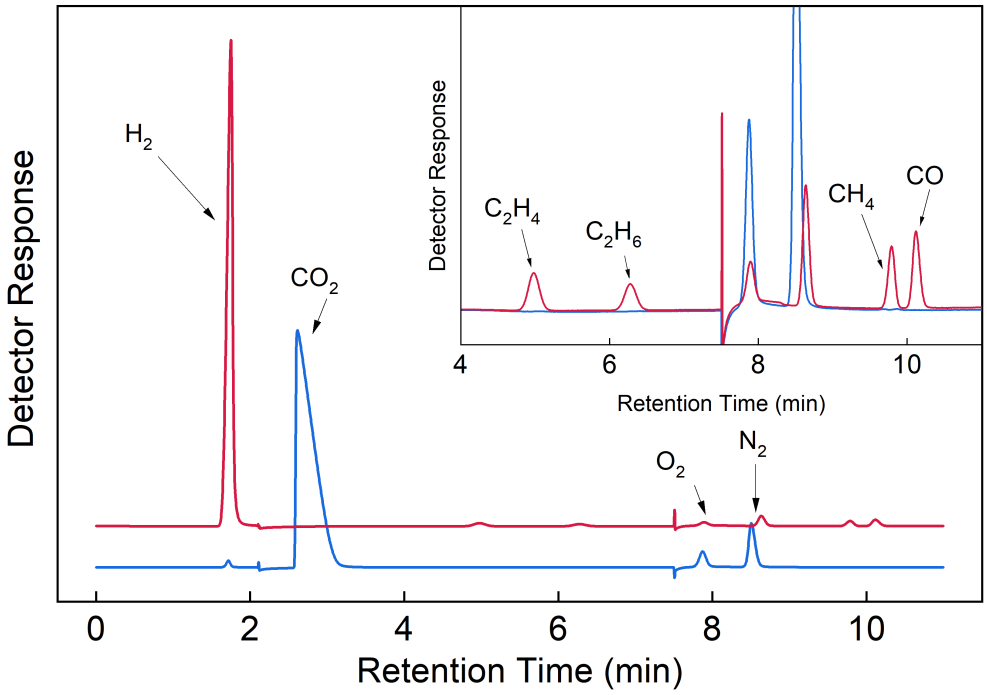

Figure 3.2: An example gas chromatogram, showing in red the excepted retention times for gaseous CO_2 reduction products (H_2, CO, CH_4, C_2H_4 and C_2H_6). In blue, a typical gas chromatogram for our system is shown, whereby the CO_2 is used to flush through the other gases.

The gas calibration was completed by injecting different volumes of the gas calibration mixture into the GC and recording the peak area for each gas. The volumes of each gas were then calculated and converted to the number of moles injected using the ideal gas equation. These were then plotted (Figure 3.3) as peak area against moles injected and the line of best fit determined. Thus the moles of a given product could be determined from the peak area of the post-electrolysis analysis.

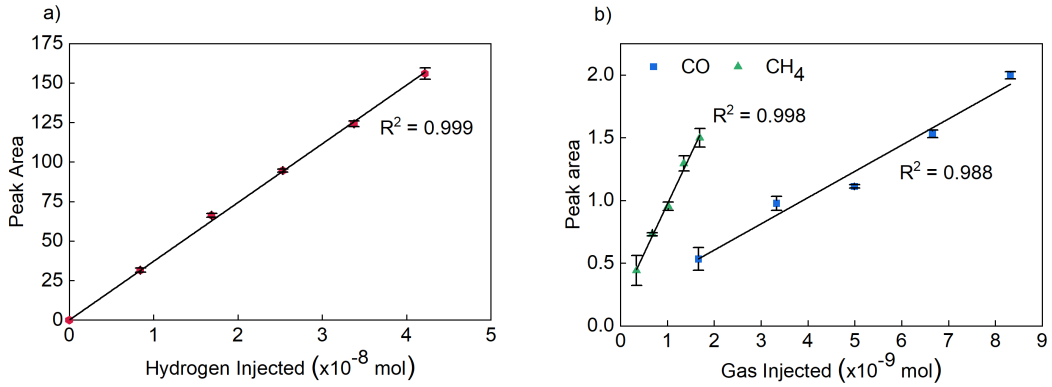

Figure 3.3: Gas calibration curves for a) hydrogen and b) carbon monoxide and methane.

3.2.5.2 Liquid Product Analysis

Liquid phase products were quantified by 1D ^{1}H Nuclear Magnetic Resonance (NMR) spectroscopy (400 MHz, Bruker). Typically NMR is not used quantitatively, because differences in spectral acquisition conditions can lead to changes in the relaxation of analytes changing their resulting peak areas.[52] However, the relative concentration of an analyte can be determined by using an internal standard. Internal standards are most commonly species that produce a single peak in a region that does not overlap with any of the analyte peaks; for electrochemical CO_2 reduction phenol and dimethyl sulfoxide (DMSO) are often used.[10] Additional benefits to using these standards are their non-volatility and wide-availability.

The same spectral acquisition parameters were used for all calibration and quantification spectra. 400 μL of the post-electrolysis electrolyte solution was mixed with 70 μL D_2O ([7789-20-0], 99.9% D, Goss Scientific) and 30 μL of internal standard solution for analysis. The internal standard consisted of 10 mM dimethyl sulfoxide-D6 ([67-68-5], 99.9% D, Cambridge Isotope Laboratories, Inc) and 50 mM phenol ([108-95-2] $\geq$99.0%, Sigma Aldrich) prepared in 100 mL 0.1 M $KHCO_3$. The water suppression method was used to record the ^{1}H spectra. An example ^{1}H NMR spectrum of the detected liquid CO_2 reduction products is shown in Figure 3.4 details of the peaks and those used for in the calibration are shown in Table 3.1. The peak height of the DMSO peak at 2.22 ppm appears unexpectedly high compared to the phenol peaks; this is likely due degradation of the internal standard solution over time, as only one batch was produced at the beginning of testing. This peak area ratio remained consistent throughout multiple experiment runs, and therefore were not deemed an error.

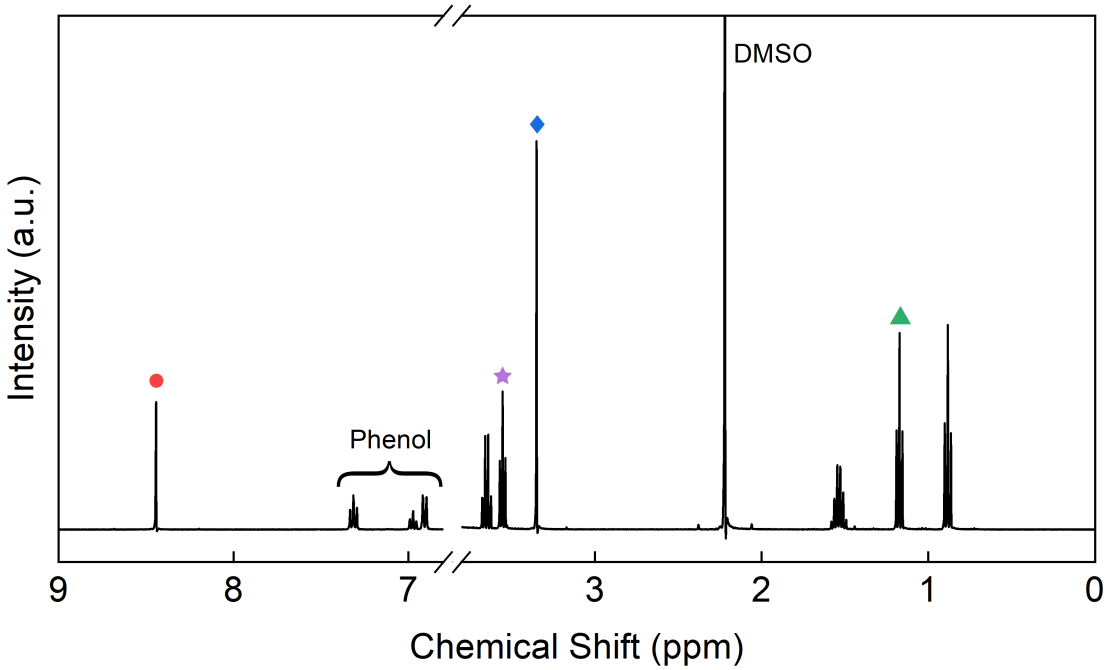

Figure 3.4: An example ^{1}H NMR spectrum showing possible liquid-phase CO_2 reduction products: formic acid, methanol, ethanol, and n-propanol, as detailed in Table 3.1. The symbols represent the peaks used for quantification. The internal standards, phenol and DMSO, are labelled. The gap in the x-axis removes the water peak.

The relative peak area of a given product peak was compared to the first phenol peak (7.32 ppm) to produce a standard calibration curve for each product, Figure 3.5. Post-electrolysis the ratio of the area of a given peak was compared to the standard curve to quantify the concentration produced. This value was then used to calculate the Faradaic efficiency.

Table 3.1: Liquid product ^{1}H NMR assignments based on commercial standards. Lines with symbols indicate the peaks used for quantification; those without symbols were used to confirm identification.

δ	^{1}H splitting	Probed Nucleus	Product Name	Symbol
8.45	s	HCOO$^-$	Formic Acid	●
7.31	t	meta−CH	Phenol	Labelled
6.97	t	para−CH	Phenol	
6.91	d	ortho−CH	Phenol	
		WATER		
3.66	q	CH_3CH_2OH	Ethanol	
3.55	t	$CH_3CH_2CH_2OH$	n-Propanol	★
3.35	s	CH_3OH	Methanol	◆
2.22	s	Internal Standard	DMSO	Labelled
1.53	sextet	$CH_3CH_2CH_2OH$	n-Propanol	
1.17	t	CH_3CH_2OH	Ethanol	▲
0.88	t	$CH_3CH_2CH_2OH$	n-Propanol	

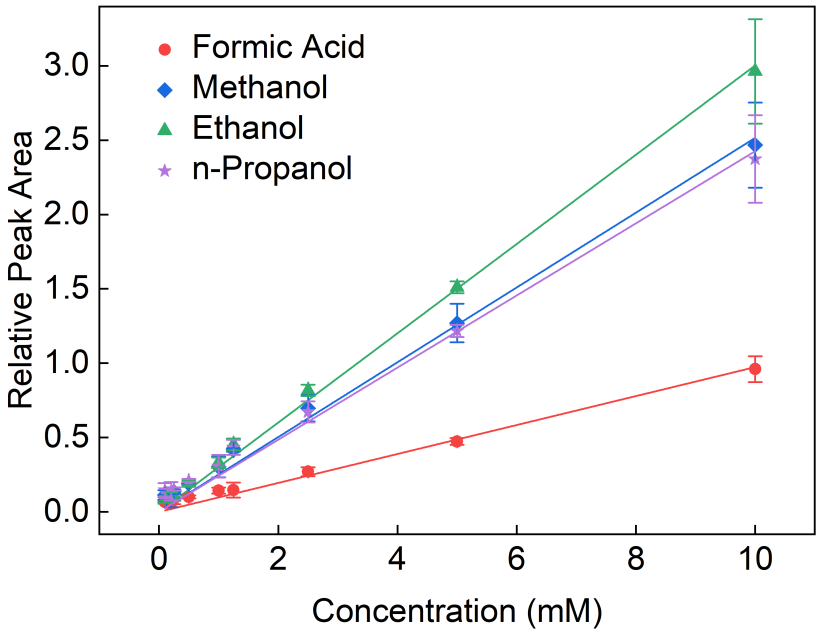

Figure 3.5: ^{1}H NMR calibration curves for possible liquid-phase CO_2 reduction products.

3.2.5.3 Faradaic Efficiency Calculations

Faradaic efficiency expresses the selectivity for a particular product from an electrochemical reaction; it is calculated using Equation 3.1, where a is the number of transferred electrons according to the relevant balanced chemical equation, n is the number of moles of a given product, F is Faraday's constant, and Q_{total} is the total charge passed.

$$\text{Faradaic Efficiency} = \frac{a \times n \times F}{Q_{total}} \times 100 \tag{3.1}$$

3.3 Results and Discussion

3.3.1 Catalyst Preparation

We first synthesised a NiCu stack by electrodeposition of copper. The deposition potential of copper was found by taking a cyclic voltammogram of $CuSO_4$ (Figure 3.6a). A reduction peak at -0.16 $V_{Ag/AgCl}$ and an oxidation peak at 0.15 $V_{Ag/AgCl}$ were seen. Thus, electrodeposition was carried out at -0.2 $V_{Ag/AgCl}$ for 600 seconds; a shiny red/brown Cu layer was seen on the Ni surface (Figure 3.6b and 3.6d). A silver layer was then added by galvanic replacement (Figure 3.6c and 3.6e); Cu acts as a sacrificial template, it is oxidised by Ag^+ due to the favourable difference in reduction potentials between copper and silver, 0.80 V Ag^+/Ag compared to 0.34 V for Cu^{2+}/Cu. Thus, some of the Cu layer is spontaneously replaced by Ag, upon submersion of the NiCu plate in a $AgNO_3$ solution for 2 minutes. This immersion period was selected as it is insufficient for complete replacement of the Cu by Ag (see Figures 3.7 and 3.14 for example).

3.3.2 Characterisation

Following their synthesis, the NiCu and NiCuAg films, and also a bare Ni plate were characterised by X-ray diffraction (XRD), scanning electron microscopy (SEM) with elemental mapping, and X-ray photoelectron spectroscopy (XPS). The NiCu and NiCuAg electrodes were also analysed by cross-sectional transmission electron spectroscopy (TEM) followed by electron energy-loss spectroscopy (EELS).

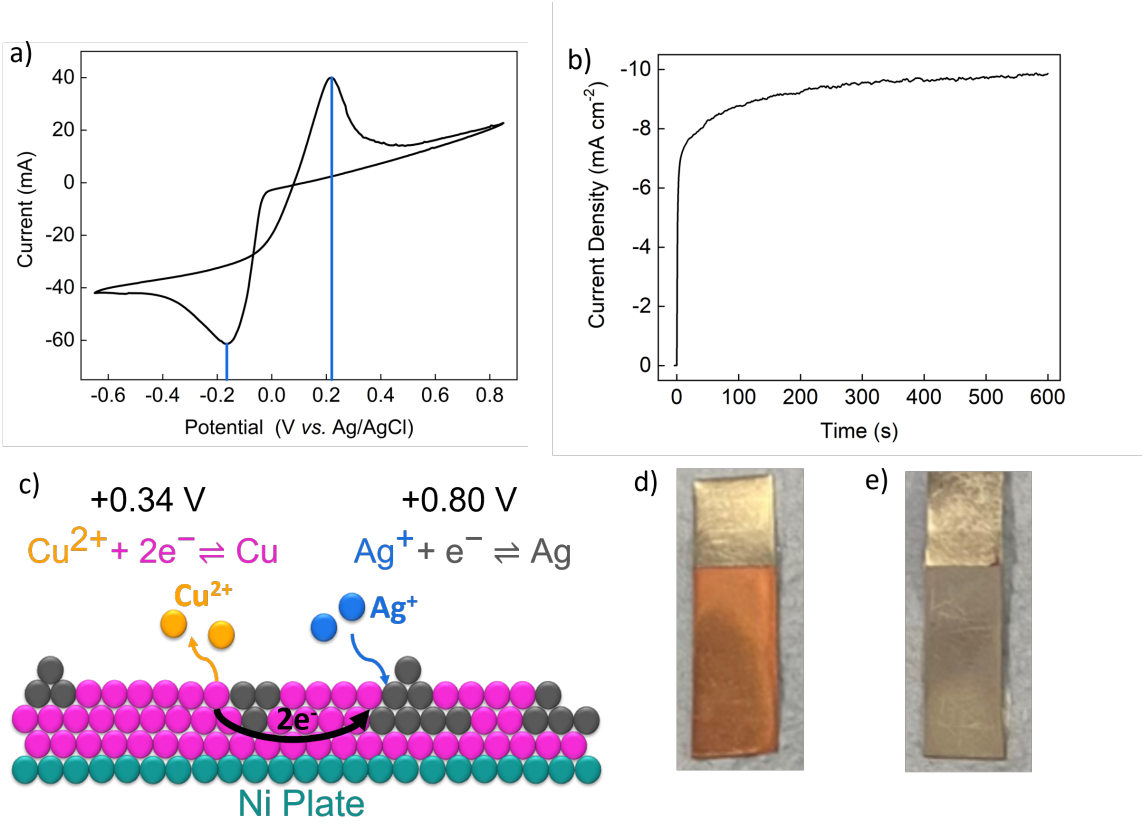

Figure 3.6: a) Cyclic voltammogram of 0.1 M $CuSO_4$ in a three-electrode set-up (Ni plate as the working electrode, leak-free Ag/AgCl as the reference electrode, and graphite rod as the counter electrode), at a scan rate of 25 mV s^{-1}; blue drop lines represent the reduction (-0.16 $V_{Ag/AgCl}$) and oxidation (0.15 $V_{Ag/AgCl}$) peaks. b) Bulk electrolysis to coat a Cu layer on Ni at -0.2 $V_{Ag/AgCl}$. c) Schematic of the galvanic replacement of Cu by Ag. d) Photo of an as-synthesised NiCu electrode. e) Photo of an as-synthesised NiCuAg electrode.

3.3.2.1 Morphology

SEM and elemental mapping were employed to investigate the surface of the catalysts. SEM images of NiCu and NiCuAg are shown in Figure 3.7. Bulbous florets of Cu nanoparticles can be seen on the Ni surface for both catalysts. A groove in the Ni surface can be seen in the NiCu images (Figure 3.7a & 3.7b): this is an outcome of the Ni plate manufacturing process, and as a result essentially no Cu is coated in that area. Figure 3.7c & 3.7d clearly show dendritic Ag particles that reach across the NiCuAg surface. Elemental mapping by energy dispersive X-ray spectroscopy Figure 3.7e-h confirms the

identity of each metal and shows that they are distinctly stacked on top of one another in layers. Yet, there are areas where Ni, and Cu are both exposed as well as the Ag. Thus, CO_2 (or its intermediate reduction products) should be able to bind on all the metal sites and benefit from the binding abilities of all three metals for various intermediates.

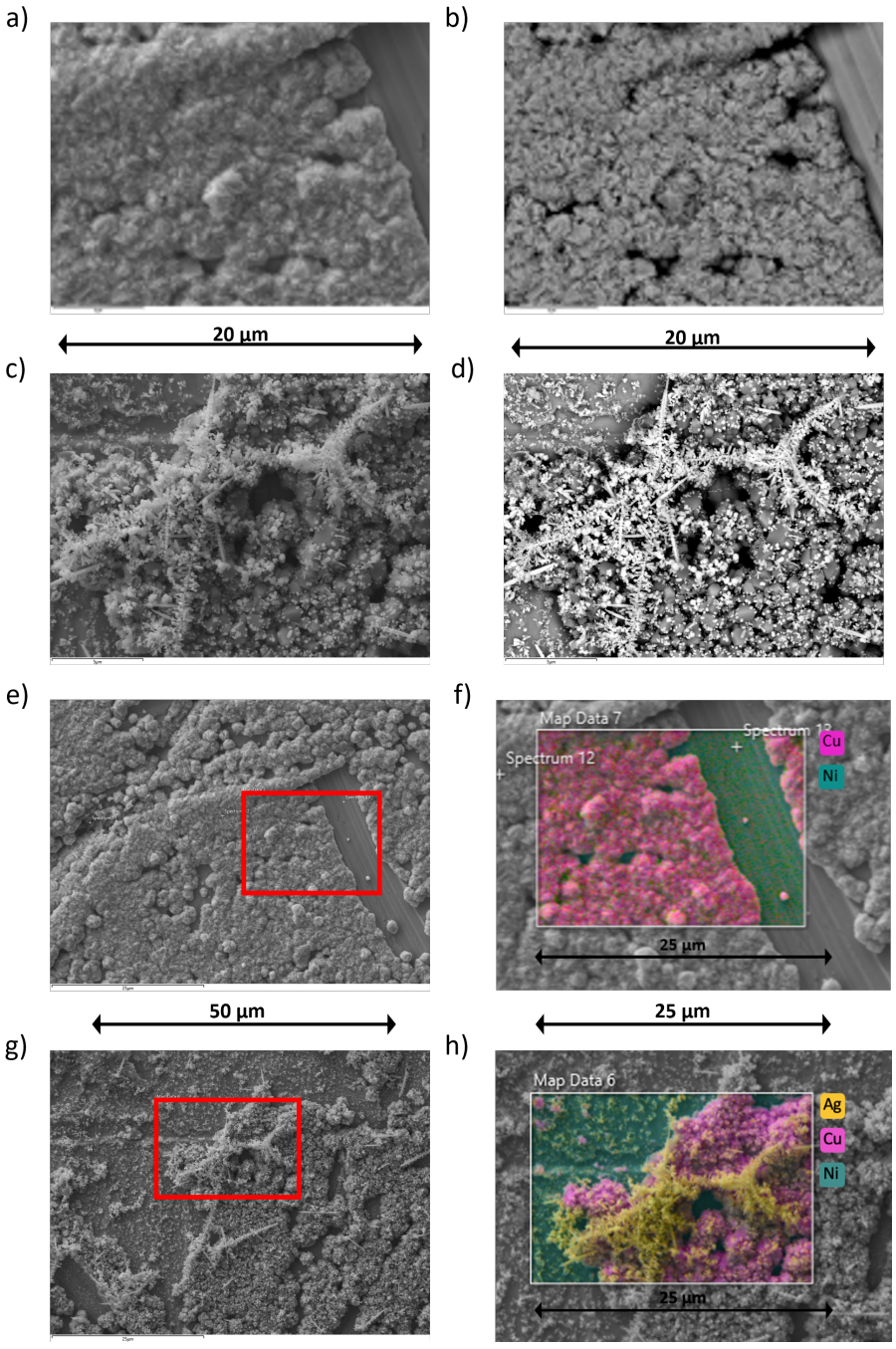

Figure 3.7: a) SEM image of NiCu. b) Backscattered electron image of NiCu. c) SEM image of NiCuAg. d) Backscattered electron image of NiCuAg. e) NiCu elemental mapping area. f) NiCu energy-dispersive X-ray spectroscopy (EDX) elemental map. g) NiCuAg elemental mapping area. h) NiCuAg EDX elemental map. For both electrode elemental maps: teal corresponds to Ni, pink to Cu and yellow to Ag.

Figure 3.8 shows the cross-sectional TEM lamellae of the NiCu and NiCuAg electrodes. Figure 3.8a clearly shows the nickel and copper layers of the NiCu electrode. Both layers are polycrystalline, with Cu showing smaller grains than Ni. The deposited Cu layer was calculated to be between 1 and 1.5 μm thick. The boundary between the Ni and Cu layer is roughly outlined by the black dashed line. The boundary between the electrodeposited Cu and the Pt, deposited as part of the imaging process, is illustrated by a blue dashed line. Both boundaries are confirmed by electron energy-loss spectroscopy (EELS), Figure 3.9, and elemental analysis, Figure 3.10.

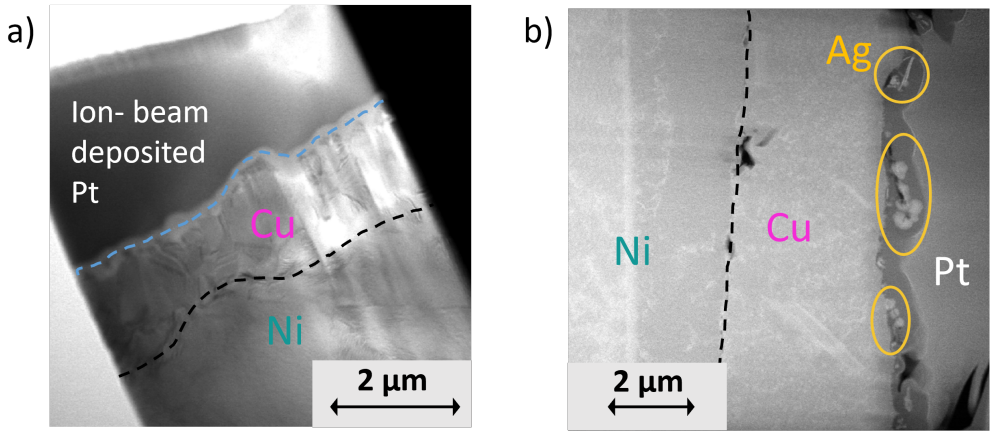

Figure 3.8: a) Bright field STEM image of the fabricated NiCu lamella. b) High-angle annular dark-field (HAADF) STEM image of the fabricated NiCuAg lamella. In both cases, the black dashed lines indicate the Ni/Cu boundary. The blue dashed line in panel a) indicates the Cu/Pt boundary; this is more difficult to pinpoint on the NiCuAg sample. Ag can be seen ringed in gold.

The Cu layer on the NiCu electrode was excessively thick to allow for full spectral area mapping of the sample, instead a series of line spectra were taken. Figure 3.9 shows a) the location of each spectral profile and b) their accompanying spectra. The sample is clean and homogeneous; Ni and Cu are prominent with only some evidence of oxygen at the boundary and within the nickel layer. Although it looks as though there is copper present in the Ni layer, this is an artefact due to the long tail produced by the Ni edge during EELS. This overlap leads to an erroneous Cu signal in the composition profiles.

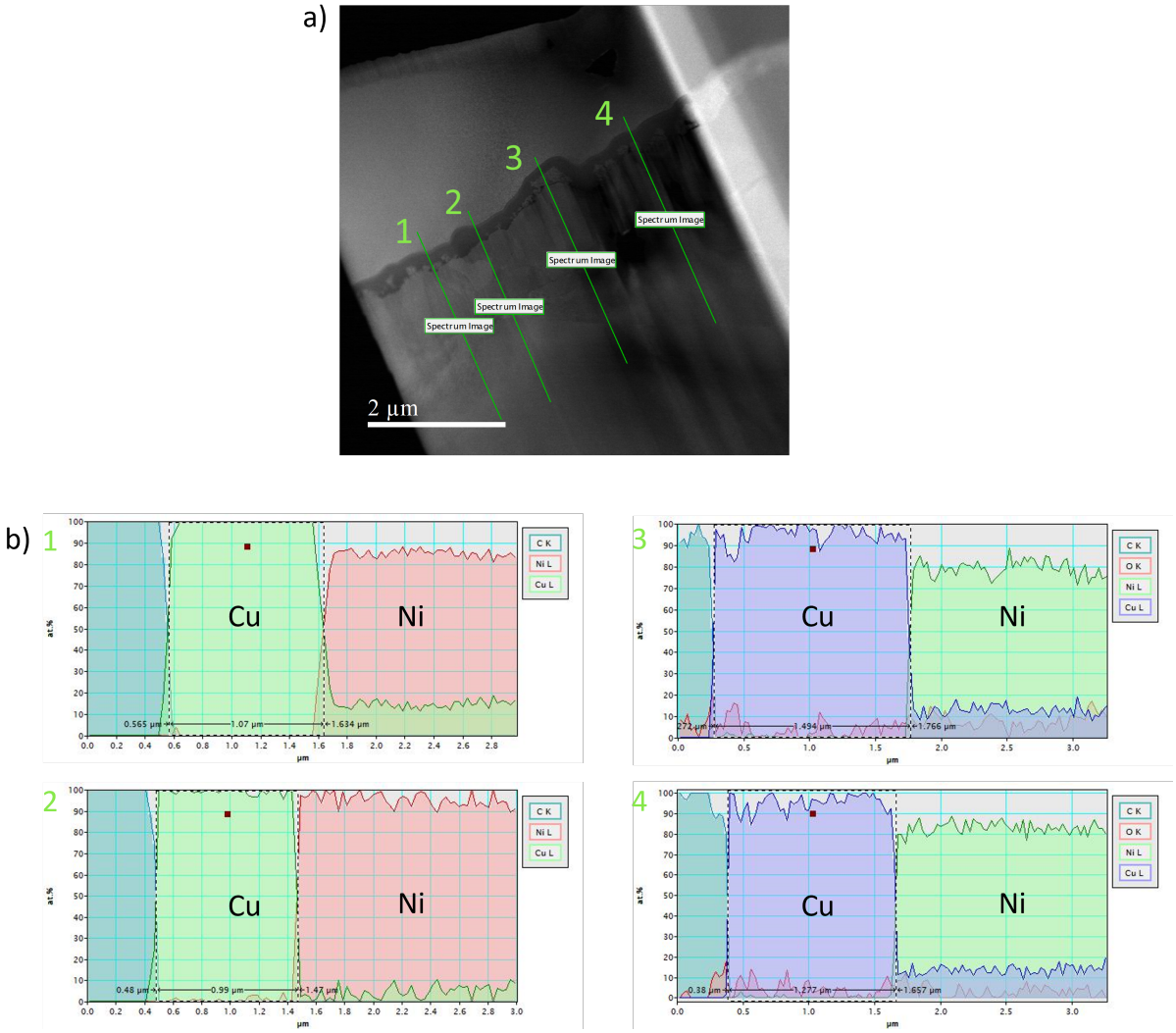

Figure 3.9: a) STEM-HAADF image of a NiCu electrode showing the locations of the composition profiles spanning the Cu layer. b) Line composition profiles collected by EELS, showing Ni, Cu, O and C. Scans 3 and 4 show that oxygen is present at the Ni/Cu boundary.

Figure 3.10 shows the elemental analysis of the NiCu lamella. The mapping clearly depicts the presence of oxygen at the interface. The colour composite displays oxygen in yellow confirming that oxide species, most likely NiO, as seen by XPS and XRD, can be found at the surface and within the bulk Ni layer shown in green.

For the NiCuAg plate, high-angle annular dark-field STEM imaging was used to create a suitable contrast between the layers (Figure 3.8b). The Ni and Cu layers are clearly defined with the boundary depicted by a dashed line. The bright areas visible on the Cu surface are due to Ag. This further confirms the uneven distribution of Ag seen in the

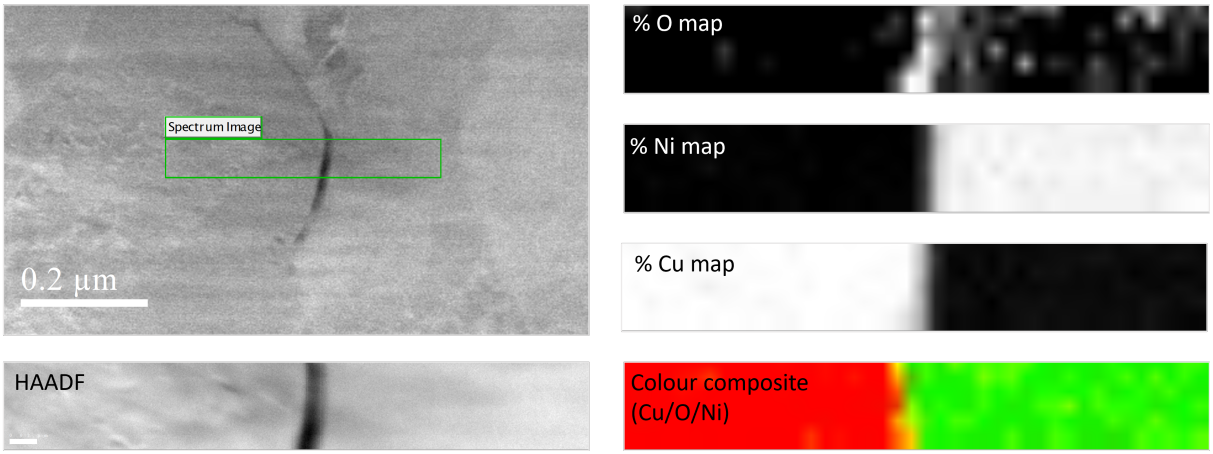

Figure 3.10: STEM-HAADF image of a Ni/Cu interface of a NiCu electrode and its EELS map profile. White = 100% Black = 0% in percentage maps. Red represents Cu, yellow represents O, and green represents Ni in the colour composite map.

SEM images above. Figure 3.8b suggests that in some areas the Ag thickness could be up to 1 μm whilst at other points there is no Ag present. It can also be seen that the galvanic replacement of Ag produces an irregular surface, increasing the surface area for CO_2 reduction to occur.

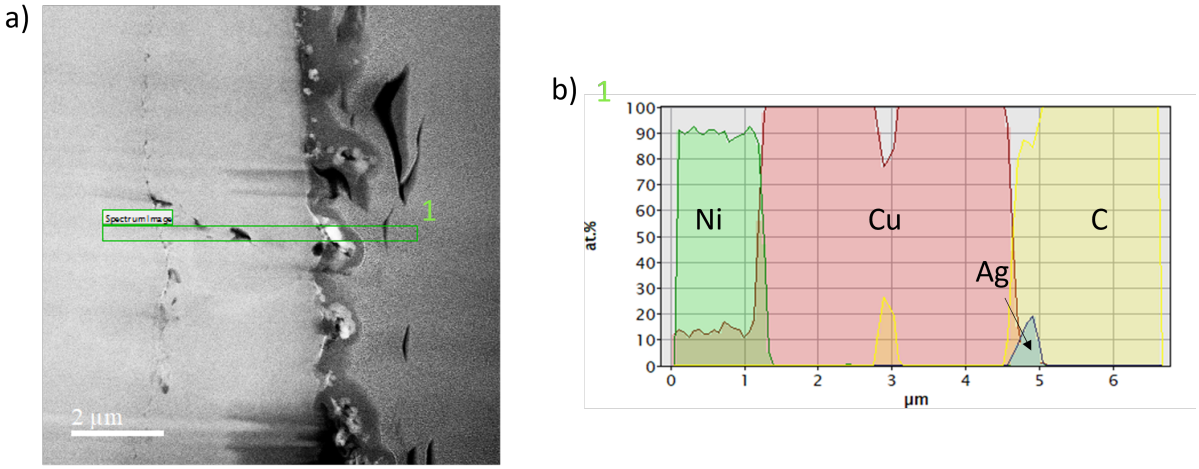

Figure 3.11: a) STEM-HAADF image of a NiCuAg electrode showing the locations of the composition profiles spanning the Cu layer. b) Line composition profiles collected by EELS, showing Ni, Cu, Ag and C.

Figure 3.11 illustrates the location and associated line composition profile of the NiCuAg lamella. Here the Cu layer is significantly thicker than in the NiCu sample, ≈3.5 μm, this suggests that the Cu layer thickness varies across the electrode. The trace also confirms that both Ag and Cu are exposed to the surface, since both are in contact with the protective carbon rich Pt that was added as part of the fabrication process. Figure 3.12

shows a narrow area elemental scan of the NiCuAg cross-sectional lamella. This further confirms that both Ag and Cu are exposed to the surface. The elemental composition percentage for Ag reaches a maximum of 23% in the brightest areas. This confirms the irregularity of the Ag coating, suggesting that even within a thin slice of the electrode Ag is exposed on multiple sides and therefore encompassed within the Pt/C mixture.

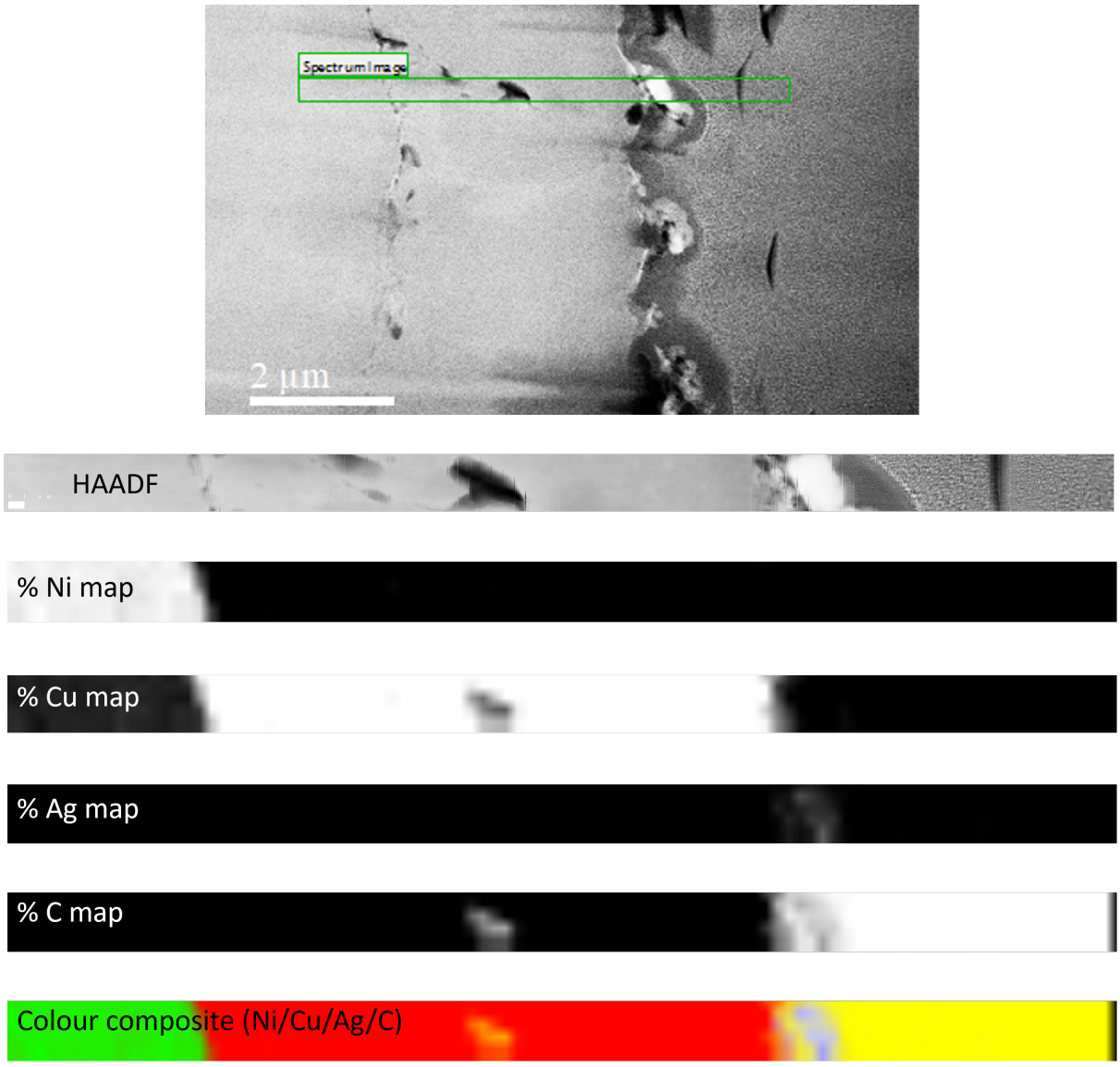

Figure 3.12: STEM-HAADF image of a NiCuAg electrode and its EELS map profile. White = 100% Black = 0% in percentage maps. Green represents Ni, red represents Cu, blue represents Ag, and yellow represents C in the colour composite map.

3.3.2.2 Composition

Figure 3.13 compares the XRD patterns of the Ni plate and as-synthesised NiCu and NiCuAg; only peaks related to the corresponding metals as defined by the PDF cards (Ni PDF no. 9009862, Cu PDF no. 4105040 and Ag PDF no. 9013047) and NiO (PDF no. 9008693) are observed. For Ni, the key peaks occur at 44.6°, 52.0° and 76.6°, which can clearly be seen in the diffractogram. Standard Cu peaks appear at 43.7°, 51.0° and 74.9°. These peaks are present in the NiCu sample at low intensity, which is consistent with the difference in layer thickness between the Cu layer and the Ni plate. For the NiCuAg sample the Cu peaks present in the NiCu sample are diminished and new peaks corresponding to the new top layer of Ag are present. The peaks at 37.8°, 44.0° and 76.7° correspond to this added Ag layer. Although the peaks of pure Ni, Cu and Ag are in similar positions, it is clear from the XRD that the additional layers have been coated and no major impurity peaks are present, save for some NiO.

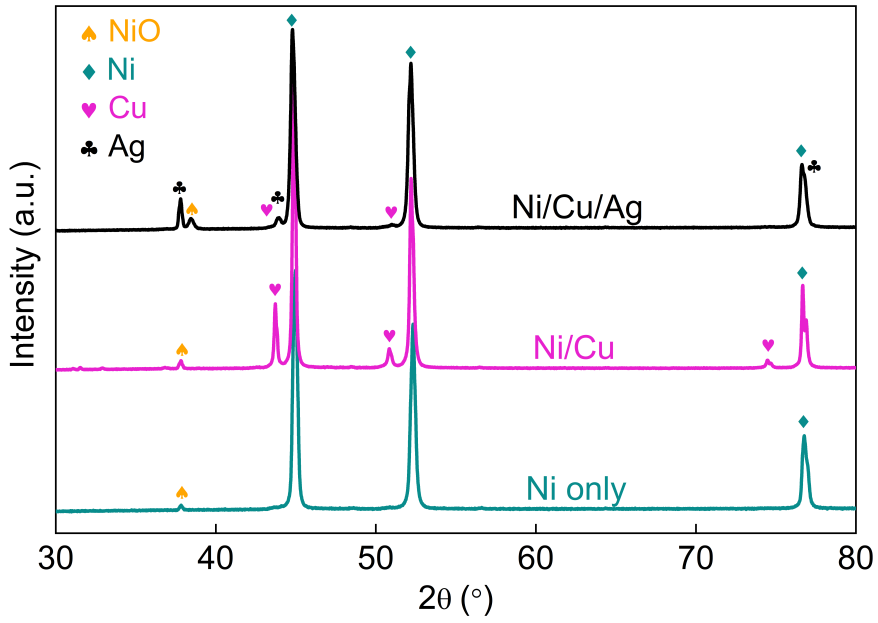

Figure 3.13: Stacked XRD patterns for Ni, NiCu and NiCuAg. Teal diamonds signify peaks relating to Ni (PDF no. 9009862), orange spades signify NiO peaks (PDF no. 9008693), pink hearts represent Cu peaks (PDF no. 4105040), and black clubs signify Ag peaks (PDF no. 9013047).

3.3.2.3 Surface Analysis

The chemical states and surface electronic structure of the catalyst plates at each stage of synthesis were detected by X-ray photoelectron spectroscopy. This allowed the identification of surface oxides which are present in low quantities and whose presence is hard to detect by bulk techniques like XRD. Figure 3.14a shows that a survey spectrum of the bare Ni plate evinces the presence of C (285 eV, C 1s), O (531 eV, O 1s), and Ni (855 eV, Ni 2p). The NiCu spectrum shows additional peaks resulting from Cu (934 eV for Cu 2p and 590 eV for Cu LMM) and the addition of the Ag layer gives further peaks (610-590 eV for Ag 3p and 369 eV for Ag 3d) in the NiCuAg spectrum. Upon coating with Cu, and further Ag, the Ni signal at 855 eV is significantly decreased. This suggests that the Cu coating is sufficiently thick that the Ni plate below is no longer detected (at least on the areas analysed). However, the final Ag layer is sufficiently discontinuous for the underlying Cu to still be detectable by XPS.

From the NiCuAg catalyst survey scan, the binding energy difference between Cu $2p_{1/2}$ and Cu $2p_{3/2}$ was 19.9 eV: this is typical of metallic Cu with an oxidised layer containing $CuO/Cu(OH)_2$ on the surface.[55] The binding energy difference between the Ag $3d_{3/2}$ and Ag $3d_{5/2}$ was 6.0 eV, characteristic of metallic Ag.[54]

The deconvoluted high-resolution spectra for each of the metals within the NiCuAg stack (Figure 3.14b–3.14d), reveal further detail about the coated species. Binding energies and peak assignments are given in Table 3.2. The Ni spectrum, focused on the Ni $2p_{3/2}$ region, shows the presence of multiple Ni containing species. The largest peak, at 856.0 eV, is attributed to NiO, whilst the peak at 852.6 eV is assigned to metallic Ni. Since the XPS measurement depth is approximately 5 nm and there are coated layers above the Ni plate,

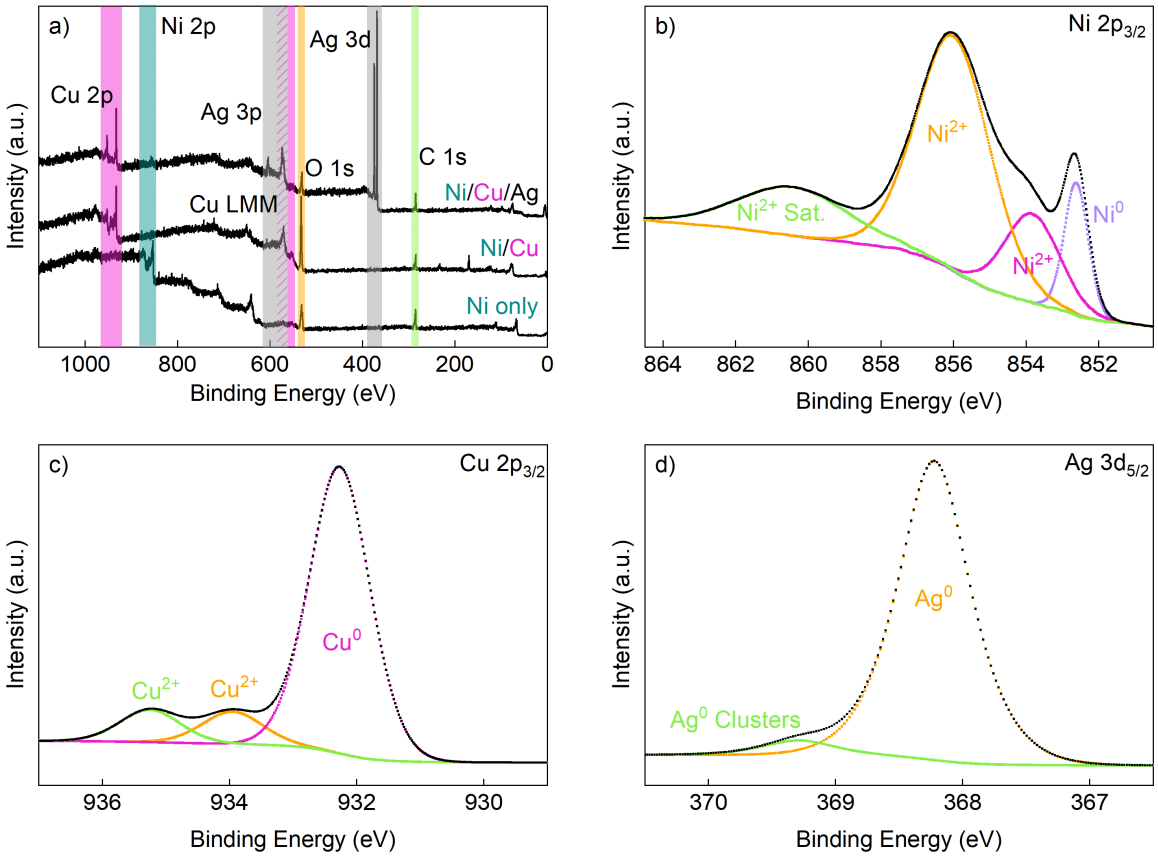

Figure 3.14: X-ray photoelectron spectroscopy survey spectra of a) each stage of the synthesised catalyst stack. Deconvoluted high resolution XPS spectrum of the NiCuAg stack: b) Ni $2p_{3/2}$; c) Cu $2p_{3/2}$; d) Ag $3d_{5/2}$. Data analysis and fittings were performed in CasaXPS software. Peak assignments were made using the NIST X-ray Photoelectron Spectroscopy Database,[53] and Perkin-Elmer Handbook of X-ray Photoelectron Spectroscopy.[54]

surface NiO is preferentially seen in the Ni XPS spectrum, Figure 3.14b. However, when the bare Ni plate is analysed, Figure 3.16, the peak assigned to metallic Ni appears to be more pronounced and the adsorbed surface NiO makes less of a contribution. This further confirms the presence of oxygen at the interface between the metals as seen by TEM.

The high-resolution Cu spectrum, Figure 3.14c, shows the Cu $2p_{3/2}$ region, however the measurement was taken over a small binding energy range, hence any data relating to Cu satellite peaks cannot be seen. The three peaks reveal that the Cu layer consists mostly of metallic Cu species with some Cu^{2+} oxides. These have been assigned as CuO which may have formed during electrodeposition[56–59] or via oxidation of the coated metallic Cu during drying. The Ag $3d_{5/2}$ spectrum is deconvoluted to reveal two peaks, the largest at

368.2 eV is attributed to metallic silver. The secondary peak at 369.3 eV results from the agglomeration of Ag particles to form clusters on the surface.[60] Thus, although there are no oxide species in the top Ag layer, both the Cu and Ni layers of the catalyst displayed peaks characteristic of their oxides.

Table 3.2: XPS binding energies for the NiCuAg catalyst stack. Binding energies calculated relative to C 1s = 285.0 eV.

Element	**Binding Energy / eV**	**Assignment**	**References**
Ni $2p_{3/2}$	852.6	Ni^0	[61]
	853.8	Ni^{2+}–NiO_{ads}	[62]
	856.0	Ni^{2+}–NiO	[63]
	860.4	Ni^{2+}–satellites	[61]
Cu $2p_{3/2}$	932.2	Cu^0	[64]
	933.9	Cu^{2+}–CuO	[65]
	935.3	Cu^{2+}–CuO	[66]
Ag $3d_{5/2}$	368.2	Ag^0	[67,68]
	369.3	Ag^0 clusters	[60]

The deconvoluted high-resolution spectrum for Cu in the NiCu stack is shown in Figure 3.15. The Cu layer in the NiCu stack was sufficiently thick that no Ni signal could be detected, thus a high-resolution Ni scan was not completed for the NiCu catalyst.

The high-resolution Cu spectrum shows the Cu $2p_{3/2}$ region. The spectrum contains seven peaks, three of which can be assigned as satellites to other peaks. The largest peak at 932.4 eV is attributed to metallic Cu, this suggests that the Cu layer primarily consists of metallic Cu. The binding energy of the peak is consistent with metallic Cu from Ni/Cu.[69] The remaining peaks in the spectrum are assigned to copper oxides mostly CuO. Surface oxides likely result from oxidation of the electrodeposited copper whilst it dries under air. Further binding energy and peak assignment details for the Cu $2p_{3/2}$ are given in Table 3.3.

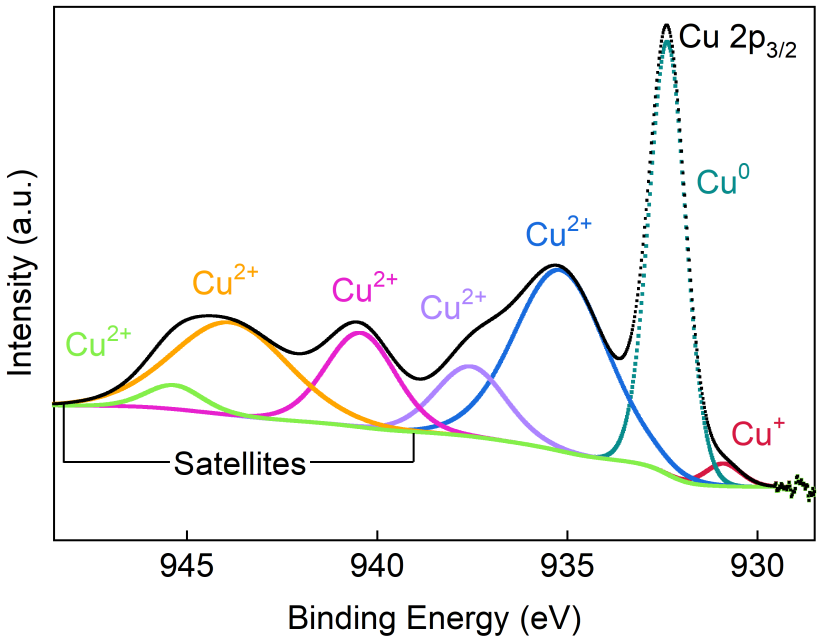

Figure 3.15: Deconvoluted high resolution XPS spectrum of the Cu $2p_{3/2}$ region for the NiCu catalyst stack. Data analysis and fittings were performed in Casa XPS software. Peak assignments were made using the NIST X-ray Photoelectron Spectroscopy Database,[53] and Perkin-Elmer Handbook of X-ray Photoelectron Septroscopy.[54]

Table 3.3: XPS binding energies for the NiCu catalyst stack. Binding energies calculated relative to C 1s = 285.0 eV.

Element	Binding Energy / eV	Assignment	References
Cu $2p_{3/2}$	930.9	Cu^{+}–Cu_2O	70
	932.4	Cu^{0}–from Ni/Cu	69
	935.2	Cu^{2+}–CuO	66
	937.5	Cu^{2+}–CuO	71
	940.4	Cu^{2+} sat.–CuO	66
	943.9	Cu^{2+} sat.–CuO	66
	945.3	Cu^{2+} sat.–CuO	66

The deconvoluted high-resolution spectrum for Ni from the bare Ni plate is shown in Figure 3.16. The Ni $2p_{3/2}$ region shown in the spectrum contains five peaks. The peak with the largest area is attributed to Ni^{2+} from adsorbed NiO,[62] at a binding energy of 853.8 eV. This is expected as XPS is a surface technique and the Ni plates were constantly exposed to air, so a layer of surface oxides was inevitable. The spectrum also shows a peak at 852.6 eV which is assigned to metallic Ni. Details of all the binding energies and assignments for the spectrum can be found in Table 3.4.

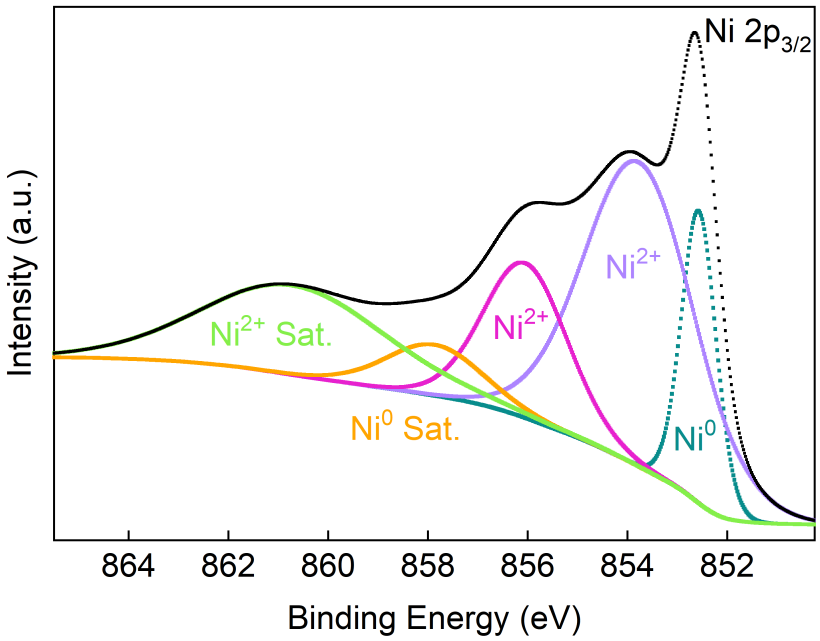

Figure 3.16: Deconvoluted high resolution XPS spectrum of the Ni $2p_{3/2}$ region for the bare Ni plate. Data analysis and fittings were performed in Casa XPS software. Peak assignments were made using the NIST X-ray Photoelectron Spectroscopy Database,[53] and Perkin-Elmer Handbook of X-ray Photoelectron Septroscopy.[54]

Table 3.4: XPS binding energies for the bare Ni plate. Binding energies calculated relative to C 1s = 285.0 eV.

Element	**Binding Energy / eV**	**Assignment**	**References**
Ni $2p_{3/2}$	852.6	Ni^0	61
	853.8	Ni^{2+}–NiO_{ads}	62
	856.1	Ni^{2+}–NiO, multiplet splitting	63
	857.9	Ni^0–satellites	72
	860.7	Ni^{2+}–satellites	61

3.3.3 Electrochemical Tests

3.3.3.1 Electrochemically Active Surface Area

Classically, electrocatalysts are evaluated based on catalytic activity often in terms of current density, in simpler terms, the current divided by the electrode area. However, it is argued by many that simply normalising by the geometric area of an electrode is inadequate to reveal the catalytic activity.[73–76] Electrode roughness and porosity can significantly affect the area available to carry out the desired reaction. Thus, the electrochemically active surface area (ECSA) has prevailed as a desirable parameter for the true surface area of a catalyst electrode. Microscopic (atomic force microscopy) and gas adsorption (Brunauer-Emmett-Teller analysis) techniques have also been suggested to evaluate the surface area however these techniques are unable to eliminate non-conductive areas as well as areas that may not be accessible to the liquid electrolyte in which the desired reaction is run.[73,75] CO_2 reduction studies often fail to accurately assess the active surface area of potential catalysts.[77]

Herein the electrochemically active surface area for the NiCuAg, NiCu and bare Ni plates were calculated using the double layer capacitance, C_{DL}, and the specific capacitance, C_S, equation 3.2, following the procedure outlined by Morales and Risch.[73]

$$\text{ECSA} = \frac{C_{DL}}{C_S} \tag{3.2}$$

The double layer capacitance can be calculated by evaluating the gradient of a plot of charging current against scan rate. A series of cyclic voltammetry experiments were undertaken at a variety of scan rates in the non-faradaic region. Measurements were conducted in a custom H-cell in 0.1 M $KHCO_3$, the electrolyte and set-up used for CO_2 reduction testing. Thus the conditions resembled the reduction conditions as closely as possible.

Initially a CV with a wide potential window and very slow scan rate was taken so that the non-faradaic region could be found. This is the potential region where no redox-processes can be observed and therefore only non-faradaic processes such as capacitance are controlling the system.[78]

Starting from the slowest scan rate a series of consecutive cyclic voltammograms were measured. A wide scan rate range was used to increases the accuracy of the end result. A bigger data set also allows for easier detection of outliers. 10 cycles were completed; the data from the last full scan was used for the capacitance calculations. Figure 3.17a shows an overlay of all the voltammograms used for the calculation of the ECSA of the NiCuAg plate, Figure 3.17b is a magnified version of the same data showing only the slower scan rates (0.01–1.00 V s^{-1}) in more detail.

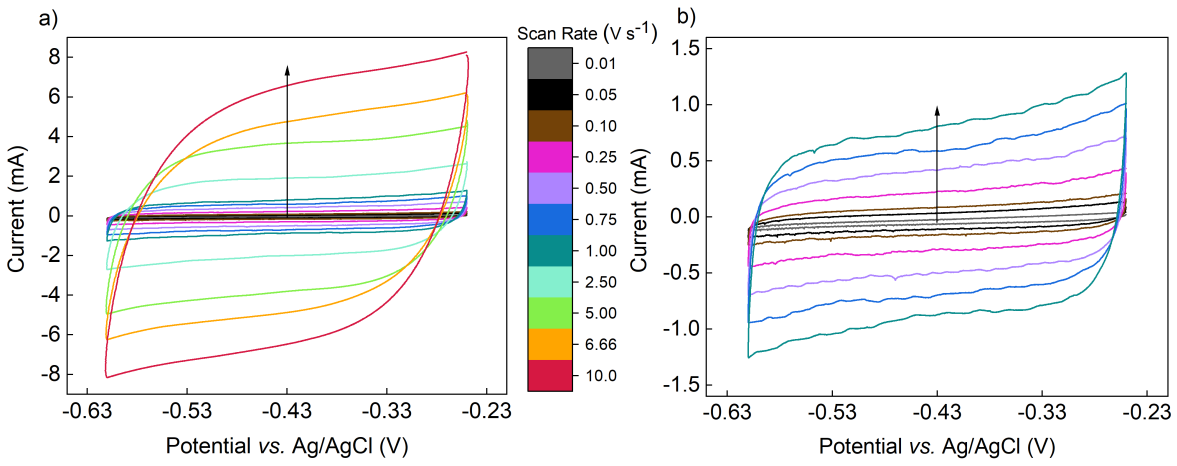

Figure 3.17: Cyclic voltammograms with different scan rates as shown in the central colour bar a) from 0.01–10.0 V s^{-1} and b) 0.01–1.00 V s^{-1} for NiCuAg in 0.1 M $KHCO_3$ in the non-faradaic potential region, −0.25 V to −0.61 V. The arrows indicate the centre potential from which the anodic charging current was extracted.

The anodic and cathodic charging current was extracted from the point around which the cyclic voltammogram is centred. For NiCuAg, this was −0.43 V, as indicated by the arrows in Figure 3.17. In an ideal capacitor the anodic and cathodic charging currents are equal in absolute value; by convention the cathodic current is negative and the anodic, positive. The charging current, i_c, is then plotted against the scan rate, Figure 3.18.

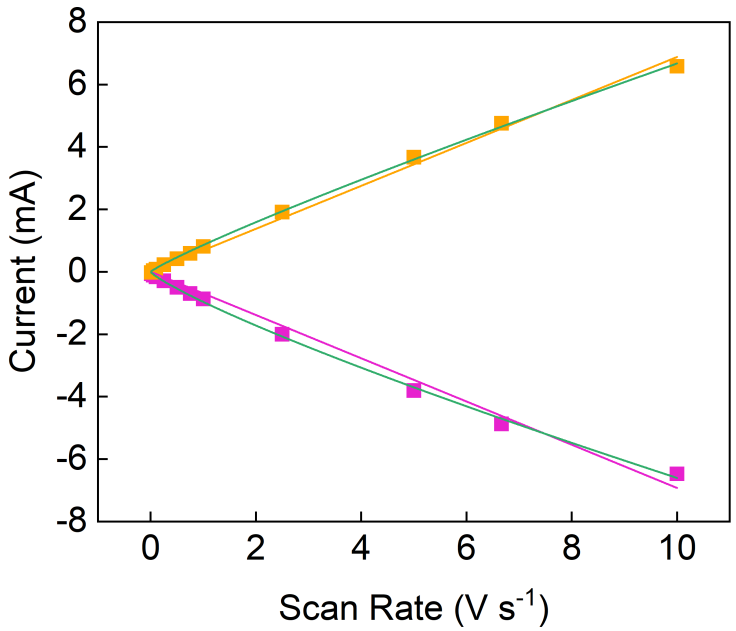

Figure 3.18: Current as a function of scan rate, taken from the cyclic voltammograms of NiCuAg. The pink squares represent the extracted cathodic charging currents and the orange squares represent the anodic charging currents. The pink and orange lines represent the initial linear regression fitting. The green lines represent the allometric data fittings.

An ideal capacitor can be represented by equation 3.3, thus the gradient of a plot of i_c vs. the scan rate, ν yields the capacitance. However, the NiCuAg plate does not behave as an ideal capacitor. This was determined by assessing the validity of the linear regression model applied to the extracted data. Typically R^2 is used to evaluate the variance of a data set from the linear regression. Table 3.5 shows the capacitance as calculated using the linear regression and the R^2 values obtained by doing so. Alternatively, the percentage non-linearity, %nL, can be used to determine the suitability of a linear model.[79] The maximum percentage non-linearity, $\%nL_{max}$, is calculated using equation 3.4, where ΔY_{max} is the maximum difference in current between the current measured and the current calculated using the linear fit, and $Y_{max} - Y_{min}$ equates to the difference between the maximum and minimum current measured.

$$i_c = \nu \times C \tag{3.3}$$

Table 3.5: Double layer capacitance, linear and allometric fit parameters and assessments of their validity by R^2 and percentage non-linearity, $\%nL_{max}$, for the NiCuAg electrode.

	Anodic Sweep			
Fit Type	C_{DL} / μF	b	R^2	$\%nL_{max}$
Linear Regression	68.80	-	0.997	4.55
Allometric Fitting	85.62	0.89	0.999	1.71
	Cathodic Sweep			
Fit Type	C_{DL} / μF	b	R^2	$\%nL_{max}$
Linear Regression	69.25	-	0.993	7.11
Allometric Fitting	96.50	0.84	0.998	2.56

$$\%nL_{\max} = \frac{|\Delta Y_{\max}|}{|Y_{\max} - Y_{\min}|} \times 100 \tag{3.4}$$

The $\%nL_{max}$ for the linear regression fits of the anodic and cathodic sweeps are shown in Table 3.5. The lower the $\%nL_{max}$ the more accurate the fit. Thus an allometric fitting was calculated, which takes the form of equation 3.6. The allometric fit can be seen visually as the green lines on Figure 3.17. As can be seen in Table 3.5 the $\%nL_{max}$ for both the anodic and cathodic sweeps was lower and thus improved by using this fitting method. This confirms that the NiCuAg electrode does not behave as an ideal capacitor, and thus the double layer capacitance was taken from the allometric fittings. This gave a final averaged value of 91.06 $\pm$ 2.4 μF as the double layer capacitance of the NiCuAg plate. It is likely that the non-ideality arises from resistance within the catalyst. Due to the layered nature of the material, the equivalent series resistance is increased; imperfections could also be found between the metals which cause the material to dissipate energy as heat further increasing the resistance and decreasing the performance away from that of an ideal capacitor.

$$y = ax + c \tag{3.5}$$

$$y = ax^b \tag{3.6}$$

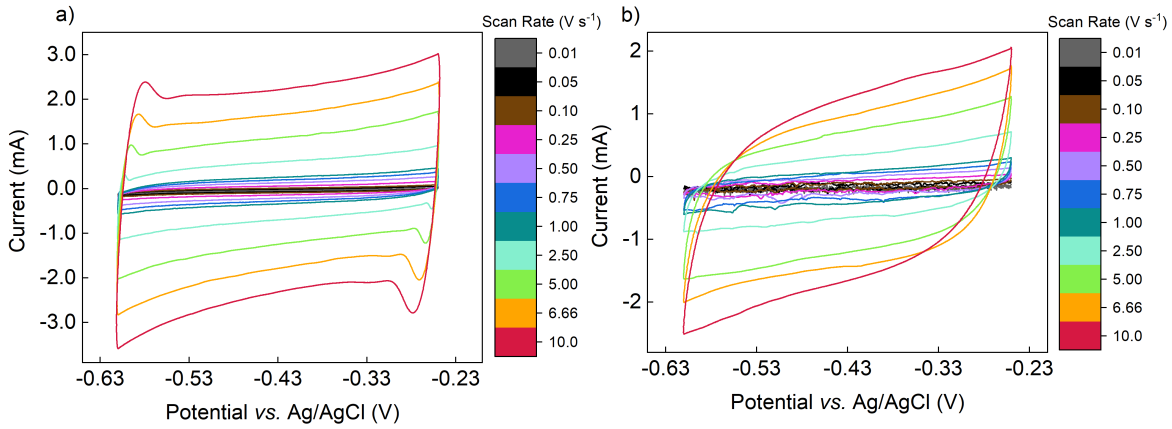

Figure 3.19: Cyclic voltammograms with different scan rates as shown in the colour bar from 0.01–10.0 V s^{-1} for a) NiCu and b) Ni in 0.1 M $KHCO_3$ in the non-faradaic potential region, −0.25 V to −0.61 V.

The double layer capacitance of the NiCu and Ni electrodes were calculated in a similar manner. Figure 3.19a shows the cyclic voltammmogram series for NiCu and Figure 3.19b shows the cyclic voltammogram series for the bare Ni plate. Figure 3.19a shows peaks at around −0.58 V and −0.27 V at scan rates above 1 V s^{-1}, these occur at the turning points of the cycle because the experiment was run above the practical bounds of the software, the Gamry software is unable to acquire the data points fast enough following the change in sweep direction.[80] The midpoint anodic and cathodic current was extracted from each scan rate, thus the turning point features did not affect the capacitance calculation. Initially, a linear fit was attempted as shown pink and orange in Figure 3.20, however after evaluation of the percentage non-linearity an allometric fitting was chosen as more suitable. Details of the fittings, R^2 and $\%nL_{max}$ values for the NiCu plate can be found in Table 3.6, and for the Ni electrode in Table 3.7.

Table 3.6: Double layer capacitance, linear and allometric fit parameters and assessments of their validity by R^2 and percentage non-linearity, $\%nL_{max}$, for the NiCu electrode plate.

	Anodic Sweep			
Fit Type	C_{DL} / μF	b	R^2	$\%nL_{max}$
Linear Regression	23.01	-	0.997	5.63
Allometric Fitting	26.18	0.94	0.997	5.03
	Cathodic Sweep			
Fit Type	C_{DL} / μF	b	R^2	$\%nL_{max}$
Linear Regression	24.62	-	0.990	6.75
Allometric Fitting	35.08	0.82	0.995	5.11

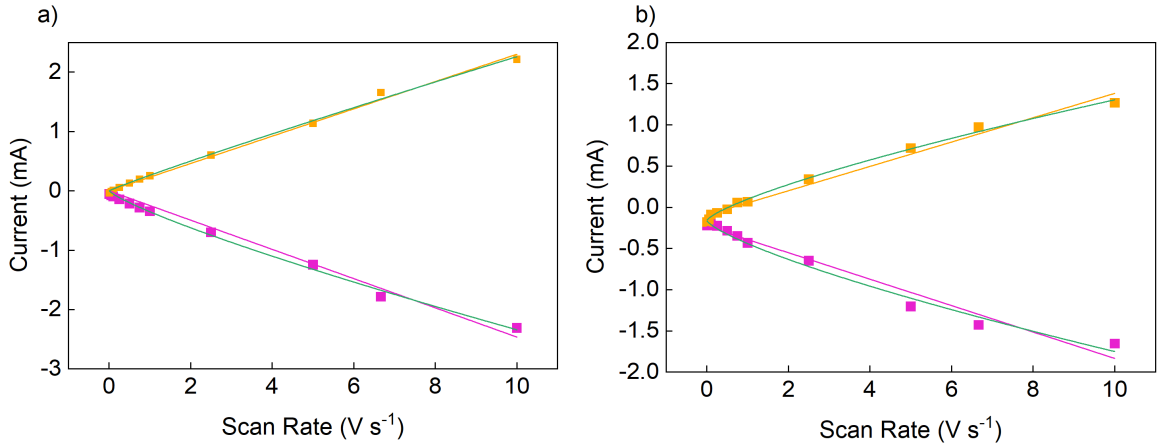

Figure 3.20: Current as a function of scan rate, taken from the cyclic voltammograms of a) NiCu and b) Ni. The pink squares represent the extracted cathodic charging currents and the orange squares represent the anodic charging currents. The pink and orange lines represent the initial linear regression fitting. The green lines represent the allometric data fittings.

Table 3.7: Double layer capacitance, linear and allometric fit parameters and assessments of their validity by R^2 and percentage non-linearity, $\%nL_{max}$, for the bare Ni plate.

	Anodic Sweep			
Fit Type	C_{DL} / μF	b	R^2	$\%nL_{max}$
Linear Regression	13.32	-	0.964	12.43
Allometric Fitting	25.79	0.75	0.997	3.86
	Cathodic Sweep			
Fit Type	C_{DL} / μF	b	R^2	$\%nL_{max}$
Linear Regression	19.51	-	0.930	20.23
Allometric Fitting	27.99	0.75	0.985	6.89

The NiCu and Ni plate electrodes both do not behave as ideal capacitors, and thus the double layer capacitance was taken from the allometric fittings. This gave a final averaged value of 30.63 $\pm$ 1.5 μF as the double layer capacitance for the NiCu plate, and 26.89 $\pm$ 1.6 μF for the Ni plate.

Alongside the double layer capacitance, the specific capacitance, C_S of each electrode must be calculated before the electrochemically active surface area can be defined. The specific capacitance allows the mass, area, or volume of active material on the electrode to be incorporated within the capacitance.[81] Equation 3.7 shows how the specific capacitance, C_S, can be calculated from the charge, Q, electrode area, a, and potential, V. Simple rearrangements allow the equation to be written in terms of the scan rate, ν, and current, I. This gives equation 3.8.

$$C_S = \frac{Q}{a \times V} = \frac{I}{a \times {}^{V}/_{t}} \tag{3.7}$$

$$I = C_S \times a \times \nu \tag{3.8}$$

The specific capacitance can be evaluated using cyclic voltammetry data.[82] The area under the charging curve of the voltammogram, A_{charge}, whereby the potential increases from V_1 to V_2 is defined by equation 3.9. By combining equations 3.8 and 3.9 we can include the specific capacitance, equation 3.10.

$$A_{\text{charge}} = \int_{V_1}^{V_2} I \, \mathrm{d}V \tag{3.9}$$

$$\begin{aligned} A_{\text{charge}} &= \int_{V_1}^{V_2} C_S \times a \times \nu \, \mathrm{d}V \\ &= C_S \times a \times \nu \times \int_{V_1}^{V_2} \mathrm{d}V \\ &= C_S \times a \times \nu \times (V_2 - V_1) \end{aligned} \tag{3.10}$$

The area of a complete cyclic voltammogram, A is defined by equation 3.11a. The area under the discharge curve, $A_{\text{discharge}}$, must be subtracted from A_{charge} to reveal only the area contained within the cyclic voltammogram. The equations for A_{charge} and $A_{\text{discharge}}$ are given by equations 3.11b and 3.11c, respectively.

$$A = A_{\text{charge}} - A_{\text{discharge}} \tag{3.11a}$$

$$A_{\text{charge}} = C_S \times a \times \nu \times (V_2 - V_1) \tag{3.11b}$$

$$A_{\text{discharge}} = C_S \times a \times \nu \times (V_1 - V_2) \tag{3.11c}$$

The combination of these equations leads to equation 3.12, which can be rearranged to give the specific capacitance, C_S, in terms of CV area, A, electrode area, a, scan rate, ν, and the CV potential difference, $(V_2 - V_1)$, as equation 3.13.

$$\begin{aligned} \therefore A &= [C_S \times a \times \nu \times (V_2 - V_1)] - [C_S \times a \times \nu \times (V_1 - V_2)] \\ &= 2[C_S \times a \times \nu \times (V_2 - V_1)] \end{aligned} \tag{3.12}$$

$$\therefore C_S = \frac{A}{2 \times a \times \nu \times (V_2 - V_1)} \tag{3.13}$$

The specific capacitance for each electrode was calculated using the as obtained cyclic voltammograms. Each CV area and scan rate gave a different value for the specific capacitance thus an averaged value for each catalyst plate is given in Table 3.8. However, this specific capacitance calculation still relies upon the geometric electrode area, a, not the true surface area of each catalyst. Thus the C_S values in Table 3.8 are approximately half the calculated C_{DL} values and the ECSA are all approximately 2 cm^2.

Commonly, a standardised value of 40 μF cm^{-2} is used for the specific capacitance, or the values of individual known materials are taken from the literature.[83] Here an attempt was made to calculate the specific capacitance for the new catalyst materials, yet the true area and surface roughness were overlooked. The surface roughness can be measured by atomic force microscopy, however this doesn't take areas of non-conductivity into account. The values for the ECSA calculated suggest that the surface is mostly a smooth coating with only small variations, contradicting the SEM images obtained, therefore these results are not accurate.

Table 3.8: Double layer capacitance, C_{DL}, specific capacitance, C_S, and electrochemically active surface area, ECSA, for the NiCuAg, NiCu and bare Ni electrodes.

Catalyst	**C_{DL} / μF**	**C_S / μF cm^{-2}**	**ECSA / cm^2**
NiCuAg	91.06 ± 2.4	48.9 ± 6.7	1.86 ± 0.3
NiCu	30.63 ± 1.5	19.3 ± 2.9	1.59 ± 0.3
Ni	26.89 ± 1.6	18.6 ± 5.6	1.45 ± 0.4

Notwithstanding the importance of the calculating of the active surface area and reporting the double layer capacitance, we suggest that the use of the geometric area to calculate the current density would not be erroneous in our case. Thus throughout the following electrochemical analysis the geometric area of 2 cm^2 was employed for all catalyst plates.

3.3.3.2 Linear Sweep Voltammetry

Linear sweep voltammetry was undertaken to measure and compare the activities of the bare Ni plate, NiCu, and NiCuAg in CO_2-saturated $KHCO_3$ and Ar-saturated $KHCO_3$, across a range of potentials, Figure 3.21. Only a single sweep from positive to negative potential was investigated for each catalyst here, however, an increased number of scans could reveal further detail about the catalytic activity. Little to no current flow was seen in both the CO_2-purged electrolyte (solid lines) or the argon-purged electrolyte (dashed lines) until a potential of around -0.4 V_{RHE} was reached, at which point appreciable current began to flow. Since this happens regardless of whether CO_2 is present or not, this current can be attributed to the onset of the background hydrogen evolution reaction.

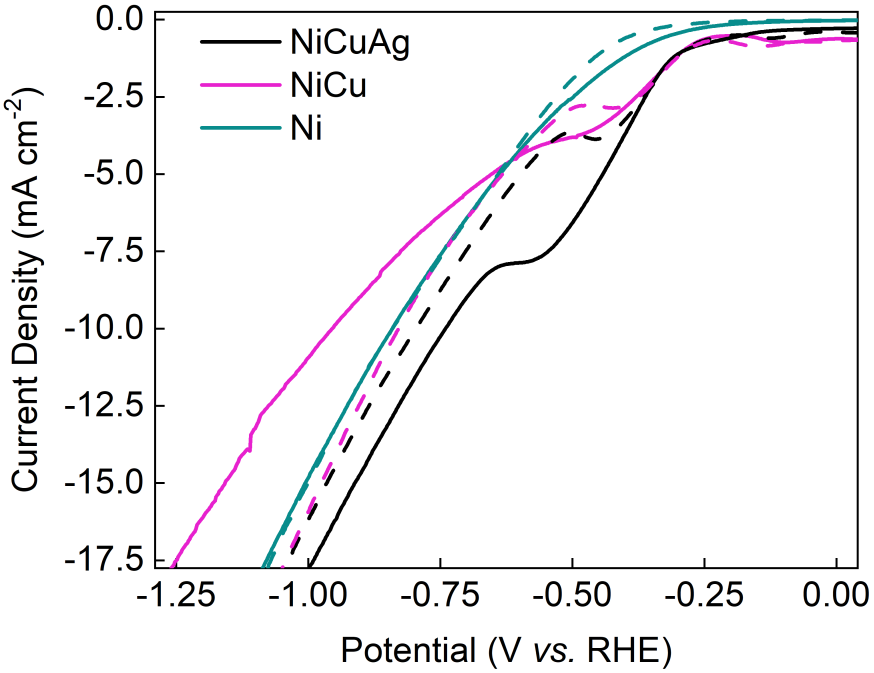

Figure 3.21: Linear Sweep Voltammetry at a sweep rate of 25 mV s^{-1}, of pure Ni (teal), NiCu (pink) and NiCuAg (black) in CO_2 saturated 0.1 M $KHCO_3$ (solid lines) and Ar-saturated 0.1 M $KHCO_3$ (dashed lines).

In the Cu-containing materials, a shoulder manifests at around −0.5 V_{RHE} in argon; this feature is well documented.[13,15,84] This has been ascribed to either the reduction of Cu oxides, which could be present in both the NiCuAg and NiCu samples, on the catalyst surface[85,86] or, the reduction of CO or related species (manifesting from the carbonate electrolyte) adsorbed on the surface of the electrode.[84,87] In support of this assertion, this shoulder becomes more pronounced in the presence of CO_2 (e.g. black solid line), suggesting that this wave is indeed due to reduction of CO or related species. In order to determine the products of any CO_2 reduction occurring via the process underlying this wave, we conducted bulk electrolysis across a range of potentials, starting from −0.29 V_{RHE}.

3.3.3.3 Bulk Electrolysis

The electrochemical CO_2 reduction activity and selectivity of the catalyst stacks and bare Ni plate were tested in a custom air-tight H-cell, Figure 3.1. CO_2-saturated 0.1 M $KHCO_3$ solution (pH = 6.8) was used as the electrolyte. Testing was performed at fixed potentials between -0.29 V_{RHE} and -1.09 V_{RHE} at 0.20 V intervals. CO_2 was continually flowed at a rate of 0.1 L min^{-1} through the set-up to flush the gas products into the gas collection bag; therefore, experiments were carried out until the attached gas collection bag had reached its capacity (2 L). Consequently, experiment length ranged but typically lasted around 40 minutes. This variability was attributed to fluctuations in CO_2 solubility in the electrolyte between experiments, as well as external factors such as temperature and changes to the integrity of the cell setup in preventing leaks. To mitigate the impact of these variations, the average result of at least three experiments was reported.

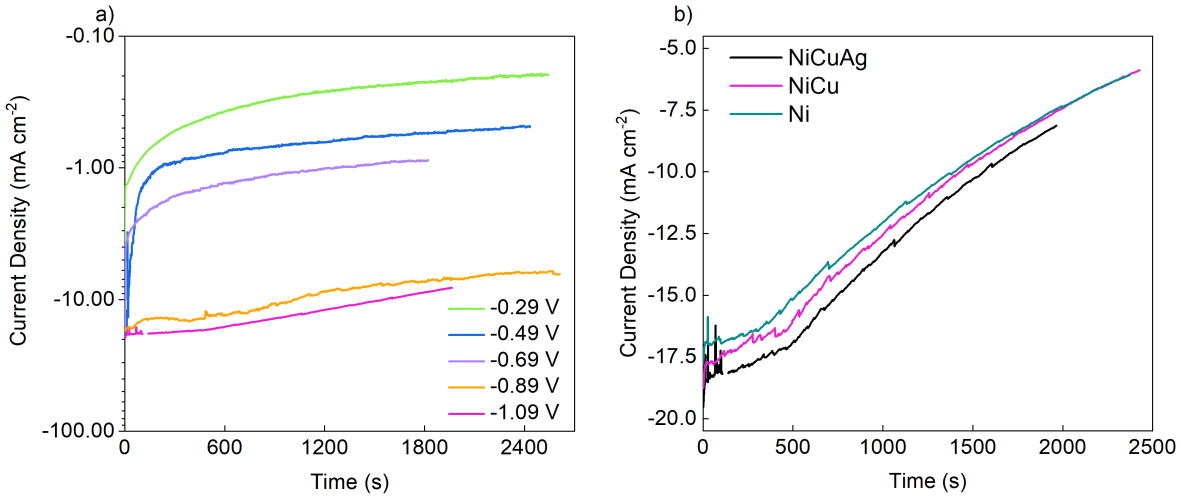

Figure 3.22: Chronoamperometry of a) NiCuAg at various potentials, and b) a comparison of the performance of NiCuAg with NiCu and Ni at 1.09 V_{RHE}, for the electrochemical reduction of CO_2 in 0.1 M $KHCO_3$ in a custom-made H-cell. Current densities were calculated using the geometric plate area of 2 cm^2.

Figure 3.22a shows bulk electrolysis using the NiCuAg catalyst at a variety of potentials. At all potentials tested, there is a decrease in current density at the experiment outset. After this initial decrease, the current density appears to become more stable; however, in all cases it continues to decrease, though at a slower rate. The average current density measured over the electrolysis for each potential can be found in the Table 3.9.

Table 3.9: Average current densities for bulk electrolysis at each potential with each catalyst.

	Average Current Density / mA cm^{-2}		
Potential / V vs. RHE	**NiCuAg**	**NiCu**	**Ni**
−0.29	−0.31	−0.25	−0.14
−0.49	−0.85	−0.53	−0.63
−0.69	−1.66	−1.83	−2.07
−0.89	−8.81	−6.48	−4.66
−1.09	−10.39	−11.24	−10.53

Faradaic efficiencies (FE) of all products observed are shown in Figure 3.23 and Table 3.10. For the 3-layered stack, NiCuAg (Figure 3.23a), the main products are H_2 and formic acid; the Faradaic efficiency for formic acid ranges from 5% to 16% over the potential range from −0.49 to −1.09 V vs. RHE. At potentials of −0.89 and −1.09 V vs. RHE, methanol is detected at Faradaic efficiencies of 2 ± 0.2% and 1 ± 0.3% respectively. At −1.09 V vs. RHE, ethanol is also seen with a Faradaic efficiency of 2 ± 0.3%. An extended-duration stability test with this electrode was performed at −1.09 V vs. RHE (see 3.3.4), showing that the catalyst maintains significant activity for up to an hour.

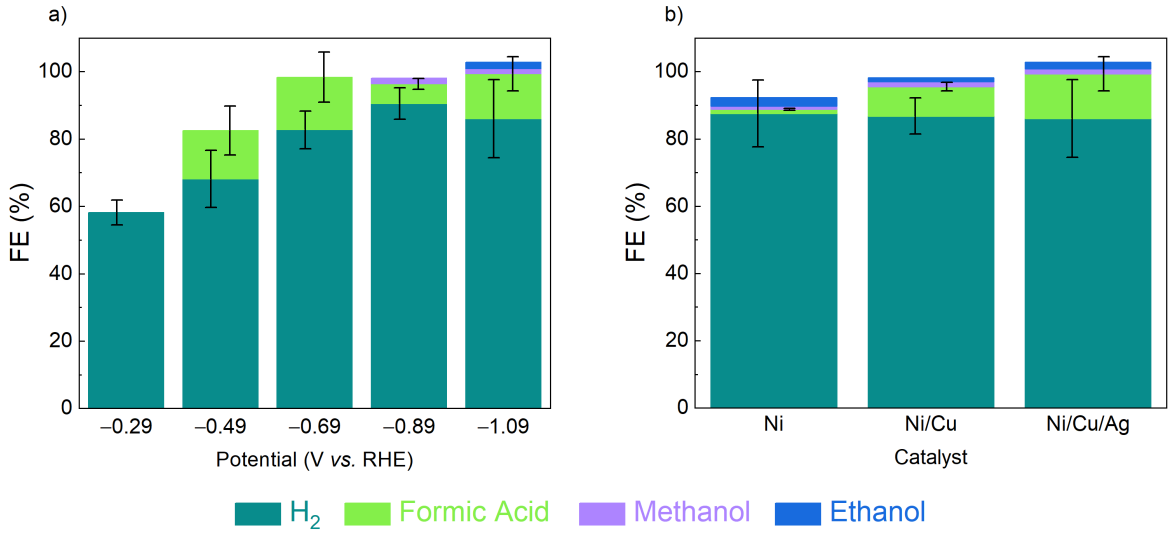

Figure 3.23: Stacked Faradaic efficiency graphs comparing a) NiCuAg across various potentials, and b) a comparison of the performance of NiCuAg with NiCu and Ni at −1.09 V_{RHE}, for the electrochemical reduction of CO_2 in 0.1 M $KHCO_3$ in a custom-made H-cell.

Faradaic efficiencies were also measured, at a range of potentials, with the other structures. Figure 3.23b shows the comparison of the CO_2 reduction products at each stage of the stack synthesis at a potential of -1.09 V_{RHE}. It is clear from this graph that the addition of each layer increased the Faradaic efficiency towards formic acid. The bare Ni plate achieved an FE of 1 ± 0.3%, predominantly favouring the hydrogen evolution reaction over the reduction of CO_2. The addition of the electrodeposited Cu layer (NiCu) increased the FE for formic acid to 9 ± 1.3%. Meanwhile, the three-layer catalyst, NiCuAg exhibited a Faradaic efficiency of 13 ± 5.1% at the same potential.

Table 3.10: Faradaic efficiencies for all products at all potentials for a) NiCuAg, b) NiCu, and c) Ni.

a) NiCuAg	**Faradaic Efficiency / %**			
Potential / V vs. RHE	**H_2**	**Formic Acid**	**Methanol**	**Ethanol**
−0.29	58 ± 3.7	-	-	-
−0.49	68 ± 8.5	14 ± 7.3	-	-
−0.69	83 ± 5.6	16 ± 7.4	-	-
−0.89	90 ± 4.7	6 ± 1.6	2 ± 0.2	-
−1.09	86 ± 11.6	13 ± 5.1	1 ± 0.3	2 ± 0.3

b) NiCu	**Faradaic Efficiency / %**			
Potential / V vs. RHE	**H_2**	**Formic Acid**	**Methanol**	**Ethanol**
−0.29	43 ± 0.8	-	-	-
−0.49	59 ± 14.5	15 ± 4.6	-	-
−0.69	65 ± 12.5	23 ± 6.2	-	-
−0.89	58 ± 14.6	24 ± 8.5	4 ± 2.4	4 ± 3.3
−1.09	87 ± 5.4	9 ± 1.3	1 ± 0.3	1 ± 0.4

c) Ni	**Faradaic Efficiency / %**			
Potential / V vs. RHE	**H_2**	**Formic Acid**	**Methanol**	**Ethanol**
−0.29	80 ± 10.8	-	-	-
−0.49	85 ± 2.2	-	-	-
−0.69	94 ± 6.4	4 ± 1.8	-	7 ± 0.5
−0.89	76 ± 8.4	3 ± 0.3	4 ± 0.8	5 ± 2.5
−1.09	88 ± 10.0	1 ± 0.3	1 ± 0.7	3 ± 1.8

Despite this, the highest Faradaic efficiency for formic acid was seen with the two-layer NiCu catalyst, 24 ± 8.5% at 0.89 V vs. RHE. Thus, the addition of the Ag layer may not always be conducive to improved CO_2 reduction. Indeed, Table 3.10b-c shows that Ni and NiCu in fact give better Faradaic yields for CO_2 reduction to methanol and ethanol than NiCuAg does. On this basis, it seems that there is little evidence to suggest that there is a beneficial synergism for carbon dioxide electroreduction from having Ni, Cu and Ag all in close proximity on the electrode surface.

The Faradaic efficiencies in Figure 3.23 and Table 3.10 don't total 100% for every catalyst and potential combination. This suggests that some percentage of the charge passed for each run is unaccounted for, and CO_2 could have reduced to a product that could not be measured as it was below the detection limit of the setup. Given that both CO and CH_4 were only detectable at peak areas above 0.5 and 0.4 we can calculate the minimum charge that would be required to achieve a peak of this size and compare it to the missing charge. For CO, 0.58 C would be required to create a peak area of 0.5 in the final GC output, and for CH_4, 1.13 C would be needed to give a peak of 0.4. This indicates that if the unaccounted for charge is below 0.58 C, 1.13 C or a combined value of 1.71 C, it could reasonably be assumed that CO, CH_4, or a mixture of both, are being produced at undetectable levels.

The missing Faradaic efficiencies and therefore average unassigned charge for each catalyst/potential combination are shown in Table 3.11. Almost all the average unaccounted for charge values are lower than the charges required to measure a detectable level of CO or CH_4, thus it is likely that some levels of CO and CH_4 were produced by all the catalysts. For the experiments which still would not reach 100%, any missing Faradaic efficiency could be lost due to product crossover or supersaturation of the electrolyte. Products could also have been lost due to the batch processing nature of this setup.

Table 3.11: Missing Faradaic efficiency, FE, and average unaccounted for charge for a) NiCuAg, b) NiCu, and c) Ni.

a) NiCuAg **Potential / V vs. RHE**	**Missing FE / %**	**Average Unaccounted for Charge / C**
−0.29	42	0.56
−0.49	18	0.63
−0.69	1	0.08
−0.89	2	0.91
−1.09	0	0

b) NiCu **Potential / V vs. RHE**	**Missing FE / %**	**Average Unaccounted for Charge / C**
−0.29	57	0.75
−0.49	26	0.67
−0.69	12	1.07
−0.89	10	3.41
−1.09	2	1.20

c) Ni **Potential / V vs. RHE**	**Missing FE / %**	**Average Unaccounted for Charge / C**
−0.29	20	0.09
−0.49	15	0.44
−0.69	0	0
−0.89	12	2.81
−1.09	7	3.64

3.3.4 Stability Testing

The electrochemical stability of the NiCuAg catalyst was determined using a long-term test at a potential of 1.09 V vs. RHE. The test was performed in 0.1 M CO_2-saturated $KHCO_3$ solution (pH = 6.8). The experiment was carried out until 10 gas collection bags had been filled (5.75 hours). CO_2 was flowed through the cell to flush the generated gases into the collection bags. Thus, each point on Figure 3.24 represents a new gas collection bag, wherein the charge difference between each point, and the capacity of a single gas collection bag (2 L) were used to calculate the Faradaic efficiency at that point.

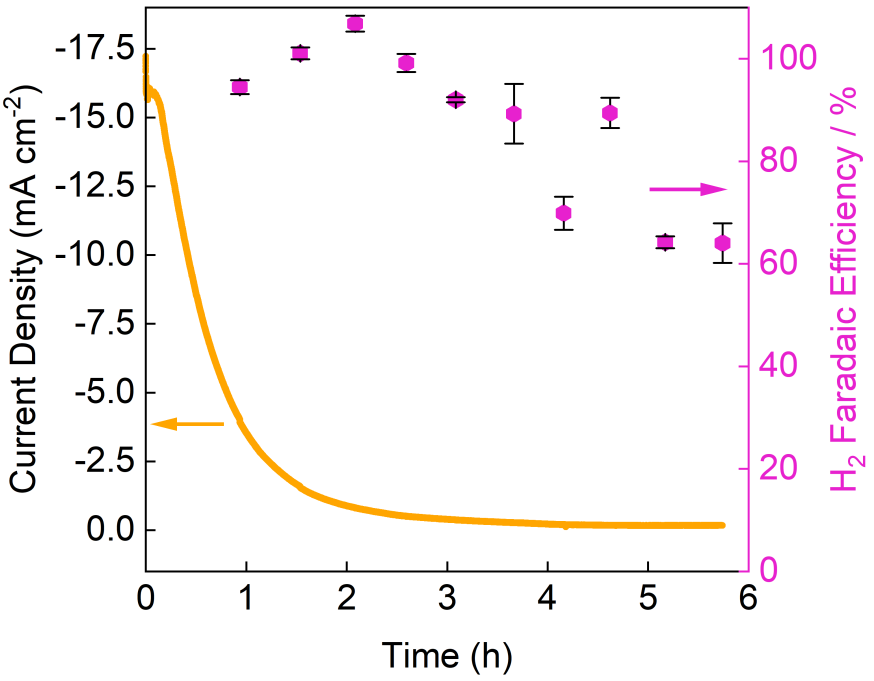

Figure 3.24: Chronoamperometric long term stability test of NiCuAg at -1.09 V_{RHE}, in 0.1 M CO_2-saturated $KHCO_3$. Current densities were calculated using the geometric plate area of 2 cm^2.

Figure 3.24 shows a rapid decrease in activity within the first 2 hours, from a current density of -16.5 mA cm^{-2} to around -0.5 mA cm^{-2}. The current density settles at around -200 μA cm^{-2} from hour 4 until the end of testing. The activity here is poor and no significant oxidation of the surface or reactivation is seen. Catalyst deactivation could be due to a change in the catalyst surface such as an oxidation state change, catalyst poisoning, or detachment. Many factors can inhibit the stability of a catalyst; a discussion of the deactivation modes of Cu containing catalysts for CO_2 reduction can be found elsewhere.[88]

Although the current density decreases, the Faradaic efficiency for hydrogen remains roughly constant between 100% and 90% for the majority of the test. This falls to between 65–70% towards the end of testing. Once the test was completed, liquid products were analysed by ^{1}H NMR. A Faradaic efficiency of 6% was calculated for formic acid. This value is lower than expected; however, this may be due to the degradation of formic acid to CO and H_2 which may have occurred at room temperature given the extent of the testing time. No other liquid products were detected.

3.4 Conclusion

In summary, we have successfully synthesised, characterised, and tested a 3-layer NiCuAg stack as a catalyst for the electrochemical reduction of CO_2. The additional metal layers of copper and silver were added by electrodeposition and galvanic replacement respectively. The corresponding 2-layer NiCu stack, as well as bare Ni, were also characterised and tested. Analysis of the results of carbon dioxide reduction experiments with these different materials showed that bimetallic NiCu and bare Ni both gave higher Faradaic efficiencies for CO_2 electroreduction to methanol and ethanol than the synthesised trimetallic NiCuAg stacks. There is, therefore, no evidence to support the hypothesis that the combination of Ni, Cu and Ag is conducive to deeper reduction of CO_2 than can be achieved by NiCu or Ni alone. All catalysts showed significant activity towards hydrogen evolution, yet the NiCu and NiCuAg catalysts remain unique compared to catalysts in the literature, in their ability to reduce CO_2 to liquid products, formic acid, methanol, and ethanol, at measurable quantities without producing high levels of carbon containing gaseous products.

The catalysts were tested at a similar potential range to that used throughout the literature, however no significant increase in activity was observed. Typically, Cu containing catalysts produce some level of CO; in this CO_2 reduction setup none was measured, however, it is likely that CO was produced at levels below the detection limit. In-line gas analysis with a GC that employed He as the carrier gas could combat this, as the thermal conductivity difference between the carrier gas and CO (and CH_4) would be greater.

The stability of the NiCuAg catalyst was poor in comparison to CO_2 reduction catalysts containing similar metals. One reason for this could be CO poisoning of the Ni sites, yet this only applies to the Ni sites not Ag and Cu. Membrane degradation, catalyst morphological changes, oxidation state changes, or surface contamination have all been

shown to occur in the presence of Fe-impurities, which could arise from cell components or unpurified electrolytes.[89] These could be the source of the poor stability in this case. Post-electrolysis analysis of the catalysts and electrolyte could be completed to investigate this further.

This work has ramifications for the development of multi-metallic catalysts for a range of electrochemical processes, showing that the combination of three individually promising materials does not necessarily lead to improved performance in the resulting ensemble.

3.5 References

[1] Intergovernmental Panel on Climate Change, *Climate Change 2021 – The Physical Science Basis*, Cambridge University Press, 2023.

[2] L. Li, J. Lin, N. Wu, S. Xie, C. Meng, Y. Zheng, X. Wang and Y. Zhao, *Energy and Built Environment*, 2022, **3**, 139–157.

[3] S. Sen and S. Ganguly, *Renewable and Sustainable Energy Reviews*, 2017, **69**, 1170–1181.

[4] M. Gattrell, N. Gupta and A. Co, *Energy Conversion and Management*, 2007, **48**, 1255–1265.

[5] N. S. Lewis and D. G. Nocera, *Proceedings of the National Academy of Sciences*, 2006, **103**, 15729–15735.

[6] K. Malik, S. Singh, S. Basu and A. Verma, *WIREs Energy and Environment*, 2017, **6**, e244.

[7] G. A. Olah, A. Goeppert and G. K. S. Prakash, *The Journal of Organic Chemistry*, 2009, **74**, 487–498.

[8] P. D. Luna, C. Hahn, D. Higgins, S. A. Jaffer, T. F. Jaramillo and E. H. Sargent, *Science*, 2019, **364**, eaav3506.

[9] M. Jouny, W. Luc and F. Jiao, *Industrial & Engineering Chemistry Research*, 2018, **57**, 2165–2177.

[10] K. P. Kuhl, E. R. Cave, D. N. Abram and T. F. Jaramillo, *Energy & Environmental Science*, 2012, **5**, 7050–7059.

[11] A. Bagger, *Current Opinion in Electrochemistry*, 2023, **40**, 101339.

[12] D. T. Whipple and P. J. A. Kenis, *The Journal of Physical Chemistry Letters*, 2010, **1**, 3451–3458.

[13] Y. Hori, A. Murata and R. Takahashi, *Journal of the Chemical Society, Faraday Transactions 1: Physical Chemistry in Condensed Phases*, 1989, **85**, 2309.

[14] R. Kortlever, J. Shen, K. J. P. Schouten, F. Calle-Vallejo and M. T. M. Koper, *The Journal of Physical Chemistry Letters*, 2015, **6**, 4073–4082.

[15] A. H. Shah, Y. Wang, A. R. Woldu, L. Lin, M. Iqbal, D. Cahen and T. He, *Journal of Physical Chemistry C*, 2018, **122**, 18528–18536.

[16] A. A. Peterson and J. K. Nørskov, *The Journal of Physical Chemistry Letters*, 2012, **3**, 251–258.

[17] Y. Li and Q. Sun, *Advanced Energy Materials*, 2016, **6**, 1600463.

[18] J. He, N. J. J. Johnson, A. Huang and C. P. Berlinguette, *ChemSusChem*, 2018, **11**, 48–57.

[19] M. K. Birhanu, M.-C. Tsai, A. W. Kahsay, C.-T. Chen, T. S. Zeleke, K. B. Ibrahim, C.-J. Huang, W.-N. Su and B.-J. Hwang, *Advanced Materials Interfaces*, 2018, **5**, 1800919.

[20] H. L. Dickinson and M. D. Symes, *Electrochemistry Communications*, 2022, **135**, 107212.

[21] D. Karapinar, C. E. Creissen, J. G. R. de la Cruz, M. W. Schreiber and M. Fontecave, *ACS Energy Letters*, 2021, **6**, 694–706.

[22] S. Nitopi, E. Bertheussen, S. B. Scott, X. Liu, A. K. Engstfeld, S. Horch, B. Seger, I. E. L. Stephens, K. Chan, C. Hahn, J. K. Nørskov, T. F. Jaramillo and I. Chorkendorff, *Chemical Reviews*, 2019, **119**, 7610–7672.

[23] B. Sun, M. Dai, S. Cai, H. Cheng, K. Song, Y. Yu and H. Hu, *Fuel*, 2023, **332**, 126114.

[24] C. Xiao and J. Zhang, *ACS Nano*, 2021, **15**, 7975–8000.

[25] J. Zhao, S. Xue, J. Barber, Y. Zhou, J. Meng and X. Ke, *Journal of Materials Chemistry A*, 2020, **8**, 4700–4734.

[26] J. Hu, F. Yang, J. Qu, Y. Cai, X. Yang and C. M. Li, *Journal of Energy Chemistry*, 2023, **87**, 162–191.

[27] M. Watanabe, M. Shibata, A. Kato, M. Azuma and T. Sakata, *Journal of The Electrochemical Society*, 1991, **138**, 3382–3389.

[28] A. Vasileff, C. Xu, Y. Jiao, Y. Zheng and S.-Z. Qiao, *Chem*, 2018, **4**, 1809–1831.

[29] J. Christophe, T. Doneux and C. Buess-Herman, *Electrocatalysis*, 2012, **3**, 139–146.

[30] S. Back, J.-H. Kim, Y.-T. Kim and Y. Jung, *ACS Applied Materials & Interfaces*, 2016, **8**, 23022–23027.

[31] Z. Cai, Y. Wu, Z. Wu, L. Yin, Z. Weng, Y. Zhong, W. Xu, X. Sun and H. Wang, *ACS Energy Letters*, 2018, **3**, 2816–2822.

[32] D. Kim, J. Resasco, Y. Yu, A. M. Asiri and P. Yang, *Nature Communications*, 2014, **5**, 4948.

[33] J. Gao, H. Zhang, X. Guo, J. Luo, S. M. Zakeeruddin, D. Ren and M. Grätzel, *Journal of the American Chemical Society*, 2019, **141**, 18704–18714.

[34] C. G. Morales-Guio, E. R. Cave, S. A. Nitopi, J. T. Feaster, L. Wang, K. P. Kuhl, A. Jackson, N. C. Johnson, D. N. Abram, T. Hatsukade, C. Hahn and T. F. Jaramillo, *Nature Catalysis*, 2018, **1**, 764–771.

[35] Y. Zhu, Z. Gao, Z. Zhang, T. Lin, Q. Zhang, H. Liu, L. Gu and W. Hu, *Nano Research*, 2022, **15**, 7861–7867.

[36] W. Chaitree, A. Hongmeuan, P. Pinthong and J. Panpranot, *Catalysts*, 2023, **13**, 1020.

[37] Z.-Y. Zhang, H. Tian, L. Bian, S.-Z. Liu, Y. Liu and Z.-L. Wang, *Journal of Energy Chemistry*, 2023, **83**, 90–97.

[38] X. Zhang, C. Liu, Y. Zhao, L. Li, Y. Chen, F. Raziq, L. Qiao, S.-X. Guo, C. Wang, G. G. Wallace, A. M. Bond and J. Zhang, *Applied Catalysis B: Environmental*, 2021, **291**, 120030.

[39] T. M. Suzuki, T. Ishizaki, S. Kosaka, N. Takahashi, N. Isomura, J. Seki, Y. Matsuoka, K. Oh-ishi, A. Oshima, K. Kitazumi, K. Sekizawa and T. Morikawa, *Chemical Communications*, 2020, **56**, 15008–15011.

[40] C. Choi, J. Cai, C. Lee, H. M. Lee, M. Xu and Y. Huang, *Nano Research*, 2021, 3497–3501.

[41] A. Bagger, W. Ju, A. S. Varela, P. Strasser and J. Rossmeisl, *ChemPhysChem*, 2017, **18**, 3266–3273.

[42] Y. Hori, K. Kikuchi and S. Suzuki, *Chemistry Letters*, 1985, **14**, 1695–1698.

[43] A. Krishnan, A. Ajith, A. V. Krishnan, R. E. Saji, S. Syamli and S. M. A. Shibli, *Surfaces and Interfaces*, 2023, **36**, 102619.

[44] V. Vij, S. Sultan, A. M. Harzandi, A. Meena, J. N. Tiwari, W.-G. Lee, T. Yoon and K. S. Kim, *ACS Catalysis*, 2017, **7**, 7196–7225.

[45] X.-H. Liu, X.-L. Jia, Y.-L. Zhao, R.-X. Zheng, Q.-L. Meng, C.-P. Liu, W. Xing and M.-L. Xiao, *Advanced Sensor and Energy Materials*, 2023, **2**, 100073.

[46] A. R. Paris and A. B. Bocarsly, *ACS Catalysis*, 2017, **7**, 6815–6820.

[47] A. I. Tsiotsias, N. D. Charisiou, I. V. Yentekakis and M. A. Goula, *Nanomaterials*, 2020, **11**, 28.

[48] N. Hoshi, M. Kato and Y. Hori, *Journal of Electroanalytical Chemistry*, 1997, **440**, 283–286.

[49] J. Rosen, G. S. Hutchings, Q. Lu, S. Rivera, Y. Zhou, D. G. Vlachos and F. Jiao, *ACS Catalysis*, 2015, **5**, 4293–4299.

[50] S. Verma, X. Lu, S. Ma, R. I. Masel and P. J. A. Kenis, *Physical Chemistry Chemical Physics*, 2016, **18**, 7075–7084.

[51] X.-G. Zhang, X. Jin, D.-Y. Wu and Z.-Q. Tian, *The Journal of Physical Chemistry C*, 2018, **122**, 25447–25455.

[52] T. D. Claridge, in *High-Resolution NMR Techniques in Organic Chemistry (Third Edition)*, ed. T. D. Claridge, Elsevier, Boston, Third Edition edn., 2016, pp. 133–169.

[53] A. V. Naumkin, A. Kraut-Vass, S. W. Gaarenstroom and C. J. Powell, *NIST X-ray Photoelectron Spectroscopy Database*, `http://dx.doi.org/10.18434/T4T88K`.

[54] C. Wagner, W. Riggs, L. Davis and J. Moulder, *Handbook of X-ray Photoelectron Spectroscopy*, Perkin-Elmer Corporation, 1979.

[55] D. H. Kim, D. H. Kwak, H. J. Tak, Y. Jung, K. Jung, S.-H. Park and J. S. Ko, *Applied Surface Science*, 2022, **590**, 153083.

[56] N. Cheng, Y. Xue, Q. Liu, J. Tian, L. Zhang, A. M. Asiri and X. Sun, *Electrochimica Acta*, 2015, **163**, 102–106.

[57] V. Patake, S. Joshi, C. Lokhande and O.-S. Joo, *Materials Chemistry and Physics*, 2009, **114**, 6–9.

[58] J.-J. Velasco-Vélez, K. Skorupska, E. Frei, Y.-C. Huang, C.-L. Dong, B.-J. Su, C.-J. Hsu, H.-Y. Chou, J.-M. Chen, P. Strasser, R. Schlögl, A. Knop-Gericke and C.-H. Chuang, *The Journal of Physical Chemistry B*, 2018, **122**, 780–787.

[59] J. Wang, L. Zhu, L. Ji and Z. Chen, *Journal of Materials Research*, 2018, **33**, 581–589.

[60] H. S. V. Parra, S. C. Velasco, J. E. A. Orjuela, J. J. O. Florez and S. Carvalho, *Coatings*, 2023, **13**, 1154.

[61] A. M. Venezia, R. Bertoncello and G. Deganello, *Surface and Interface Analysis*, 1995, **23**, 239–247.

[62] K. Kim and N. Winograd, *Surface Science*, 1974, **43**, 625–643.

[63] C. L. Bianchi, M. G. Cattania and P. Villa, *Applied Surface Science*, 1993, **70-71**, 211–216.

[64] B. R. Strohmeier, D. E. Levden, R. S. Field and D. M. Hercules, *Journal of Catalysis*, 1985, **94**, 514–530.

[65] T. Nakamura, H. Tomizuka, M. Takahashil and T. Hoshi, *Hyomen Kagaku*, 1995, **16**, 515–520.

[66] F. Parmigiani, G. Pacchioni, F. Illas and P. Bagus, *Journal of Electron Spectroscopy and Related Phenomena*, 1992, **59**, 255–269.

[67] M. P. Seah, I. S. Gilmore and G. Beamson, *Surface and Interface Analysis*, 1998, **26**, 642–649.

[68] G. Johansson, J. Hedman, A. Berndtsson, M. Klasson and R. Nilsson, *Journal of Electron Spectroscopy and Related Phenomena*, 1973, **2**, 295–317.

[69] K. Kishi and M. Sasanuma, *Journal of Electron Spectroscopy and Related Phenomena*, 1989, **48**, 421–434.

[70] A. H. Asif, N. Rafique, R. A. K. Hirani, L. Shi, Y. Wang, X. Duan, Y. Yin and H. Sun, *Chemical Engineering Journal*, 2023, **469**, 143915.

[71] A. Khalid, P. Ahmad, A. I. Alharthi, S. Muhammad, M. U. Khandaker, M. Rehman, M. R. I. Faruque, I. U. Din, M. A. Alotaibi, K. Alzimami and D. A. Bradley, *Nanomaterials*, 2021, **11**, 451.

[72] L.-S. Hsu and R. Williams, *Journal of Physics and Chemistry of Solids*, 1994, **55**, 305–312.

[73] D. M. Morales and M. Risch, *Journal of Physics: Energy*, 2021, **3**, 034013.

[74] R. Martínez-Hincapié, J. Wegner, M. U. Anwar, A. Raza-Khan, S. Franzka, S. Kleszczynski and V. Čolić, *Electrochimica Acta*, 2024, **476**, 143663.

[75] H. Ren, Y. Pan, C. C. Sorrell and H. Du, *J. Mater. Chem. A*, 2020, **8**, 3154–3159.

[76] M. Rahaman, A. Dutta and P. Broekmann, *ChemSusChem*, 2017, **10**, 1733–1741.

[77] P. Chauhan, K. Hiekel, J. S. Diercks, J. Herranz, V. A. Saveleva, P. Khavlyuk, A. Eychmüller and T. J. Schmidt, *ACS Materials Au*, 2022, **2**, 278–292.

[78] A. J. Bard, L. R. Faulkner and H. S. P. o. c. White, *Electrochemical methods: fundamentals and applications*, John Wiley & Sons, Ltd, Hoboken, NJ, USA, Third / Allen J. Bard, Larry R. Faulkner, Henry S. White. edn., 2022.

[79] K. Emancipator and M. H. Kroll, *Clinical Chemistry*, 1993, **39**, 766–772.

[80] Gamry, *Gamry Instruments Framework Help*, `https://www.gamry.com/Framework%20Help/HTML5%20-%20Tripane%20-%20Audience%20A/framework_help.htm`, Created by Gamry.

[81] B. E. Conway, *Electrochemical Supercapacitors*, Springer US, 1999.

[82] S. Sharma and P. Chand, *Results in Chemistry*, 2023, **5**, 100885.

[83] C. C. L. McCrory, S. Jung, J. C. Peters and T. F. Jaramillo, *Journal of the American Chemical Society*, 2013, **135**, 16977–16987.

[84] Y. Hori, A. Murata, R. Takahashi and S. Suzuki, *Journal of the Chemical Society, Chemical Communications*, 1988, 17.

[85] M. Kang and A. A. Gewirth, *The Journal of Physical Chemistry B*, 2002, **106**, 12211–12220.

[86] B. Vidhyadharan, I. I. Misnon, R. A. Aziz, K. P. Padmasree, M. M. Yusoff and R. Jose, *J. Mater. Chem. A*, 2014, **2**, 6578–6588.

[87] A. Wuttig, C. Liu, Q. Peng, M. Yaguchi, C. H. Hendon, K. Motobayashi, S. Ye, M. Osawa and Y. Surendranath, *ACS Central Science*, 2016, **2**, 522–528.

[88] H. Wu, H. Yu, Y.-L. Chow, P. A. Webley and J. Zhang, *Advanced Materials*, 2024, **36**, 2403217.

[89] A. F. Staerz, M. van Leeuwen, T. Priamushko, T. Saatkamp, B. Endrődi, N. Plankensteiner, M. Jobbagy, S. Pahlavan, M. J. W. Blom, C. Janáky, S. Cherevko and P. M. Vereecken, *Angewandte Chemie International Edition*, 2024, **63**, e202306503.

Chapter 4

Layered Catalysts for the Hydrogen Evolution Reaction

Acknowledgements and Declarations

Thanks go to Mr Jim Gallagher at the Scanning Electron Microscopy facility in the School of Chemistry, University of Glasgow for imaging and elemental mapping services. Thanks go to Dr Chris Kelly in the School of Chemistry, University of Glasgow for X-ray photoelectron spectroscopy services.

Abstract

The development of catalysts for hydrogen evolution remains a key area in the move towards hydrogen as a future energy carrier for renewable energy. The stacked catalysts synthesised in Chapter 3, originally for CO_2 reduction, produced high levels of hydrogen upon testing, thus their hydrogen evolution activity was defined at a range of pH values. Platinum is the best catalyst for hydrogen evolution; however, it is expensive and scarce. Herein, the trimetallic NiCuAg "stack" catalyst was tested and adapted to include a Pt layer, NiCuPt. The two-layer NiCu, bare Ni, and a two-layer NiPt catalyst were also tested in a range of electrolytes. The synthesis method was adjusted somewhat successfully to produce NiPt by electrodeposition, and NiCuPt by galvanic replacement; both of which were successfully characterised. Upon testing NiPt exhibited the lowest overpotential at -100 mA cm^{-2} of -102 ± 21 mV and a Tafel slope of -51.8 ± 2.7 mV dec^{-1} in 0.1 M KOH. NiCuPt displayed improved activity compared to the other catalysts in acid, yet the overpotentials and Tafel slope observed in basic media were comparable to that of bare Ni, suggesting the Pt layer could be further optimised. The Faradaic efficiency of all the catalysts was around 90%.

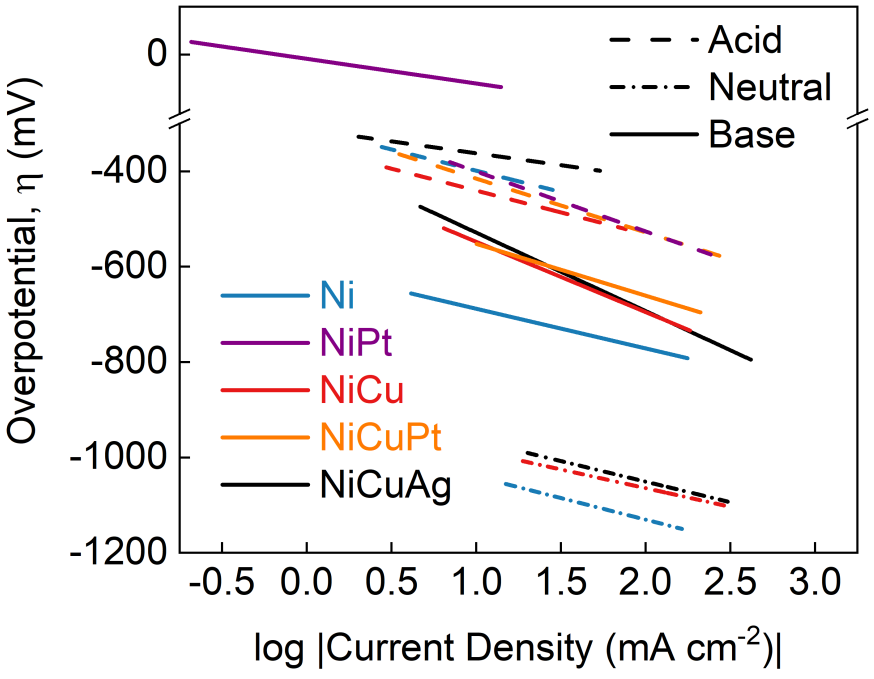

4.1 Introduction

The production of sustainable hydrogen from electrochemical water electrolysis is a promising technique[1,2] against the growing demand for renewable energy storage[3,4] alongside the much needed decrease in CO_2 emissions.[5,6] Typically hydrogen is produced by steam reforming methane which in turn emits CO_2.[7,8] Thus successful electrocatalytic hydrogen production would prove beneficial not just for intermittent energy storage but also for the sustainable production of industrially required hydrogen.[9]

Hydrogen evolution is often facilitated by noble metals such as platinum.[10,11] Pt is thought to be the most promising catalyst on a technical basis due to its high cathodic currents at low overpotentials and small Tafel slope.[12,13] However, Pt is expensive and scarce[14,15] thus a significant decrease on the reliance on Pt as a catalyst for hydrogen evolution is required for noteworthy global scalability to be achieved.

Across a variety of pure metal catalysts, hydrogen evolution activity has been shown to display a volcano type relationship.[14,16,17] The relationship is dependent on the hydrogen adsorption free energy, and therefore the M−H bond strength of each metal.[16] A catalyst with too high a binding energy will limit the reaction at the desorption step, and a catalyst with too weak a binding energy will limit the reaction rate at the adsorption step. Pt is located at the top of the volcano plot indicating it has the highest activity and an intermediate binding strength. Consequently, the volcano plots are used to predict suitable alternatives to Pt, often combining less adequate metals to achieve bimetallic and trimetallic catalysts.[18]

Nickel is often employed as an alternative hydrogen evolution catalyst due to its low cost and abundance.[18] It is also increasingly employed as part of nickel-based alloys,[19,20] chalcogenides,[21,22] nitrides[23,24] and phosphides[25,26] which can be found reviewed elsewhere.[27,28] A synergistic effect is often stated to occur upon the employment of Ni as part of an alloy or other mixed species catalyst.[27] The addition of a neighbouring heteroatom or heterostructure can induce a shift in the d-band centre,[29,30] a downshift lowers the energy required for H desorption whilst an increase amplifies H adsorption.[31] Thus the addition of one or more hetero-species can tailor the electronic structure of the catalyst and therefore the electrocatalytic activity.[29]

Table 4.1: Synthesis techniques, overpotential, η, and Tafel slopes of some recent Ni-containing electrocatalysts for the hydrogen evolution reaction.

Catalyst	**Synthesis Technique**	**Electrolyte**	**η at 10 mA cm^{-2}/ mV**	**Tafel slope/ mV dec^{-1}**	**Ref.**
NiCoS	2-step hydrothermal synthesis	0.5 M H_2SO_4	−232	80.17	[32]
Cu/Ni−Co	Electro-deposition	1 M NaOH	*	124	[33]
Ni−Co−Cu	Electro-deposition	6 M KOH	−288†	94	[34]
Ni−Mo−Cu	Electro-deposition	6 M KOH	−142†	56	[34]
NiMo−$NiCu_{0.06}$	Co-electro-deposition	6 M KOH	−86	42	[35]
NiMo−$NiCu_{0.12}$	Co-electro-deposition	6 M KOH	−88	46	[35]
NiCu	Precipitation and annealing	1 M KOH	−250	130	[36]
Ni−Cu	1-step Ni cone synthesis and Cu electro-deposition	1 M NaOH	‡	121.4	[37]

**log(current at 200 mV overvoltage /A cm^{-2}) = −3.92, †η at 100 mA cm^{-2}, ‡E_{ONSET} = −1.35 V vs. SCE (saturated calomel electrode) calculated from the intersection of two tangents on the LSV curve.*

Recent examples of Ni based catalyst for hydrogen evolution, particularly those where Cu has been incorporated, are shown in Table 4.1. Reporting on the activity of hydrogen evolution catalysts is highly varied with some papers including an onset potential (often not defined by a suitable current density value i.e. 0.5—2 mA cm^{-2}),[38] and most not including a key metric, the Faradaic efficiency.[39]

Following the successful synthesis of our three layer stack, NiCuAg, testing showed that hydrogen was the dominating product under CO_2 reduction conditions (pH 6.8).[40] Thus, in this chapter we set out to quantify the hydrogen evolution ability of NiCuAg and its preceding two layer (NiCu) electrode and bare Ni electrode forms for the hydrogen evolution reaction; testing in neutral, basic, and acidic conditions.

In light of those results and motivated by Chen *et al.*,[41] who showed that a monolayer of Pt is enough to enhance hydrogen evolution activity, we also synthesised NiCuPt and NiPt electrodes. This aimed to reduce the demand for high Pt loading by employing only a thin layer of Pt at the surface, thereby decreasing the cost compared to a purely Pt electrode. NiCuPt was synthesised by galvanic replacement of Cu with Pt, and NiPt by electrodeposition of Pt.

Herein we report the successful synthesis and characterisation of NiCuPt and NiPt. The hydrogen evolution performance of NiCuAg, NiCu, Ni, NiCuPt, and NiPt were assessed; ovepotentials at 10 and 100 mA cm^{-2} are reported followed by their Tafel slopes, under acidic and basic conditions. NiCuAg, NiCu and Ni were also evaluated under neutral conditions. The Faradaic efficiencies of all catalysts under acidic conditions were also calculated.

4.2 Experimental

4.2.1 Materials

Nickel foil (0.25 mm, [7440-02-0], annealed, 99.5 %), and copper (II) sulfate ([7758-98-7], anhydrous, 98%) were obtained from Alfa Aesar. Silver nitrate ([7761-88-8], ACS reagent, >99%), potassium phosphate monobasic ([7778-77-0], ACS reagent, ≥99.0%), potassium phosphate dibasic ([7758-11-4], ACS reagent, ≥98%), and potassium hydroxide ([1310-58-3], pellets, reagent grade, ≥85%) were obtained from Sigma Aldrich. Platinum (IV) chloride [13454-96-1] was supplied by Johnson Matthey. Sulfuric acid ([7664-93-9], technical grade, ≥95%) was obtained from ThermoFisher Scientific. Nitrogen (≥99.998%, Industrial Grade) and hydrogen (99.99%) were supplied by BOC Limited. All chemicals were used as received without further purification and all solutions were produced using ultrapure water (15.8 MΩ-cm).

4.2.2 Catalyst Preparation

Nickel foil was cut to a size of 2 × 1 cm and the backside covered using Sellotape. This was used as the working electrode. The Ni surface was cleaned prior to any coating by sonication for 10 minutes each in: acetone, followed by isopropyl alcohol and finally deionised water. NiCu and NiCuAg electrodes were prepared as described in Chapter 3. Platinum electrodeposition (from a 0.5% solution of $PtCl_4$ at −315 mV vs. Ag/AgCl) was completed in an open beaker for 10 minutes whilst stirring. For platinum deposition, a standard three-electrode setup was used: leak-free Ag/AgCl reference electrode (Innovative Instruments, Inc.), Ni foil working electrode, and graphite rod (Alfa Aesar) counter electrode. These electrodes are referred to as NiPt. The NiCuPt electrodes were

synthesised by copper electrodeposition, as described in Chapter 3, followed by galvanic replacement. A platinum layer was added by placing the NiCu stack in a 5 mM $PtCl_4$ solution for two minutes, without stirring, to give NiCuPt. All catalysts were prepared at room temperature and pressure.

4.2.3 Characterisation

The surface morphology of the prepared electrocatalyst plates was analysed with the help of Jim Gallagher in the School of Chemistry, University of Glasgow. The electrodes were first coated with a gold/palladium target, to enhance the image quality, using a Polaron SC7640 auto/manual high resolution sputter coater. Peaks resulting from Au and Pd were removed from the measured EDX analysis. The imaging was completed on a TESCAN CLARA Ultra High Resolution Scanning Electron Microscope (UHR-SEM). Energy Dispersive X-ray spectroscopy and mapping was completed using an Oxford Instruments UltimMax 65 with Aztec live interface.

X-ray diffraction (XRD) was undertaken using a Rigaku MiniFlex benchtop diffractometer equipped with Cu sealed tube X-ray source. The surface composition of the catalysts was analysed by X-ray photoelectron spectroscopy (XPS) at the University of Glasgow by Chris Kelly using a Kratos AXIS Supra+ with a dual Ag/Al filament X-ray source. For all measurements the Al filament was used. All data analyses and fittings were made using OriginLab software.

4.2.4 Electrochemical Characterisation

Electrochemical studies were controlled by a Gamry interface 1010E potentiostat, at room temperature and pressure. Linear sweep voltammograms, multi-step chronoamperometry and chronopotentiometry experiments were carried out in a 50 mL single-compartment standard electrochemical cell manufactured by Ossila (Figure 4.1), slight modifications were employed to ensure the cell remained air-tight. A graphite rod and leak-free Ag/AgCl electrode were used as the counter and reference electrodes respectively. The electrodes were tested under acidic, neutral and basic conditions thus 0.1 M H_2SO_4, 0.1 M potassium phosphate buffer (KH_2PO_4/K_2HPO_4), and 0.1 M KOH were used as the respective electrolytes. The cell was purged with N_2 gas for at least 20 minutes prior to testing. Linear sweep measurements were taken between +0.2 and −2.0 V vs. Ag/AgCl with a scan rate of 2 mV/s. Tafel slopes were determined using stepped chronoamperometry, the current density was allowed to stabilise for 5 minutes at each potential recorded. The resultant Tafel plots were constructed from the averages of several runs. Current-interrupt internal resistance compensation was used for all measurements.

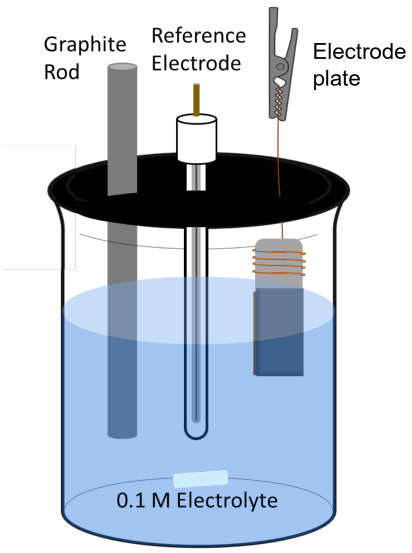

Figure 4.1: Customised Ossila single-compartment air-tight cell set-up, as used for electrochemical hydrogen evolution tests.

4.2.5 Hydrogen Analysis

Following bulk electrolysis at -100 mAcm^{-2} for 10 minutes, gas chromatography was conducted on the headspace of the airtight single-compartment cell to determine the Faradaic efficiency of hydrogen for each catalyst. A 1 mL sample was analysed was by direct injection using the Agilent 8860 GC system equipped with 2 Porapak Q columns and a MoleSieve 13X column. A thermal conductivity detector was used.

The GC was calibrated using commercially available hydrogen (99.99%), injection volumes ranged from 0.1 to 1.0 mL. This achieved a peak area range similar to that seen during headspace testing. The volume of each injection of hydrogen was then calculated and converted to the number of moles injected using the ideal gas equation. These were then plotted (Figure 4.2) as peak area against moles injected and the line of best fit determined. Thus the moles of hydrogen injected could be determined from the peak area of the post-electrolysis analysis. The total system headspace was determined by filling the cell with water at room temperature.

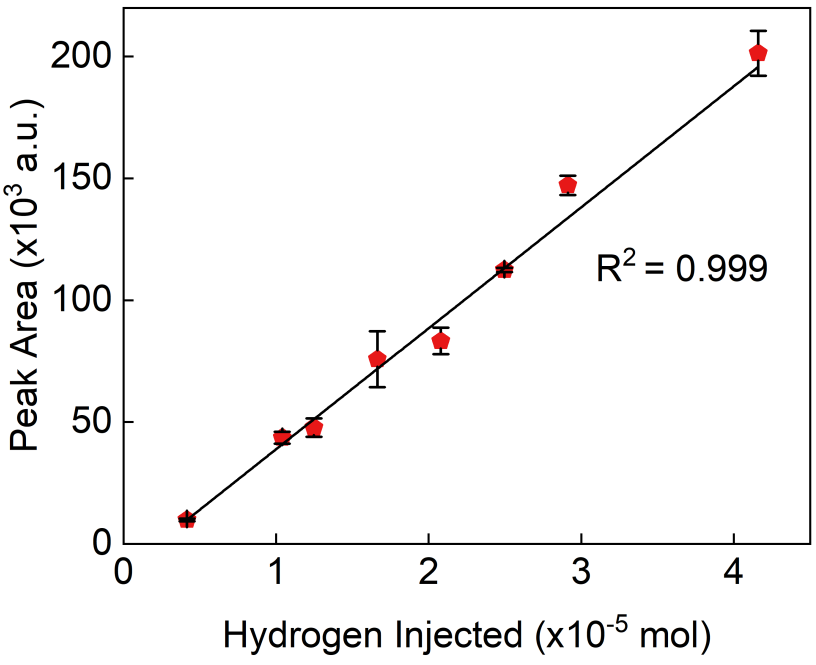

Figure 4.2: Gas chromatography calibration curve for hydrogen.

This was then used to calculate the Faradaic efficiency for hydrogen according to equation 4.1, where a is the number of transferred electrons, 2 for hydrogen evolution, n is the number of moles of a given product, F is Faraday's constant, and Q_{total} is the total charge passed, 120 C for this setup. All hydrogen analysis was perform at least twice and average Faradaic efficiencies are reported.

$$\text{Faradaic Efficiency} = \frac{a \times n \times F}{Q_{total}} \times 100 = \frac{2 \times n \times F}{120} \times 100 \tag{4.1}$$

4.3 Results and Discussion

A detailed description of the successful preparation and characterisation of NiCu and NiCuAg catalyst plates can be found in Chapter 3. Thus sections 4.3.1 and 4.3.2 refer only to the synthesis and characterisation of the newly introduced NiCuPt and NiPt layered catalysts.

4.3.1 Catalyst Preparation

The NiCuPt electrode was prepared in two steps, the first being the electrodeposition of Cu from $CuSO_4$ at $-0.2\ V_{Ag/AgCl}$ as described in the previous chapter to give NiCu, Figure 4.3a. The second step was galvanic replacement in 5 mM $PtCl_4$. As can be seen by the standard electrode potentials shown in Table 4.2, both possible pathways for the reduction of Pt ions to its solid form have a more positive electrode potential than the reduction of Cu^{2+}. Therefore Cu acts as a sacrificial template and is spontaneously replaced by Pt, upon submersion of the NiCu electrode in the $PtCl_4$ solution. Galvanic replacement from a platinum chloride solution onto Cu is a well established technique.[42–44] Therefore,

based on the findings from the previous chapter, which established that two minutes was sufficient to produce a Ag layer, galvanic replacement was completed for a period of 2 minutes. After which a black/blue coating could be seen on the catalyst surface, Figure 4.3b. Once dried the coating presented as an iridescent blue/grey colour, Figure 4.3c.

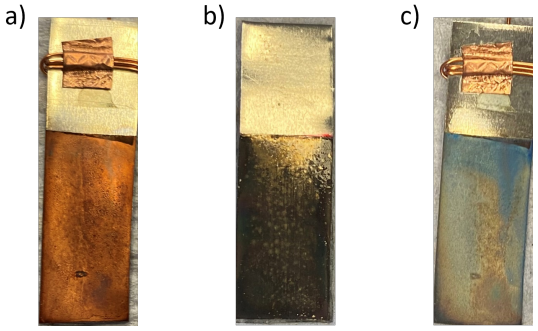

Figure 4.3: Photographs of electrodes a) as-synthesised NiCu, b) NiCuPt immediately following immersion, c) dried as-synthesised NiCuPt.

Table 4.2: Relevant standard electrode potentials for the galvanic replacement of Pt on Cu at 25°C and 1 atm.[45]

Reaction	E^0/ V
$Cu^{2+} + 2e^- \rightleftharpoons Cu$	+0.340
$PtCl_4^{2-} + 2e^- \rightleftharpoons Pt + 4Cl^-$	+0.758
$Pt^{2+} + 2e^- \rightleftharpoons Pt$	+1.188

The NiPt electrode was prepared by electrodeposition of platinum onto a clean Ni plate. The deposition potential of platinum was found by completing a cyclic voltammogram of the coating electrolyte, 0.5 m/v% $PtCl_4$ ($\approx$ 0.03 M), Figure 4.4a. This concentration was chosen so that the CV could be easily compared to work by Stanca *et al.*[46] The reduction of Pt^{4+} to metallic Pt takes place via two two-electron steps shown in equations 4.2 and 4.3.[46] In the cyclic voltammorgram, Figure 4.4a, the first reduction to Pt^{2+} can be seen by a slight change in gradient at +0.02 $V_{Ag/AgCl}$, this is clearest in the first cycle of the CV (not shown here) and suggests that the majority of Pt ions are present as Pt^{2+} by the second cycle. The key reduction peak at -0.315 $V_{Ag/AgCl}$ is assigned to equation 4.3 and thus relates to the coating of a metallic Pt layer. Beyond this, around -0.8 $V_{Ag/AgCl}$, hydrogen evolution occurs. Thus, electrodepositon was carried out at -0.315 $V_{Ag/AgCl}$ for 600 seconds, Figure 4.4b; a dull grey Pt layer was seen on the Ni surface (Figure 4.4b inset), to give NiPt. Here, the coating occurs separately to hydrogen generation, however the formation of hydrogen bubbles can be used to induced porosity into the Pt layers by coating at a more negative potential.[46]

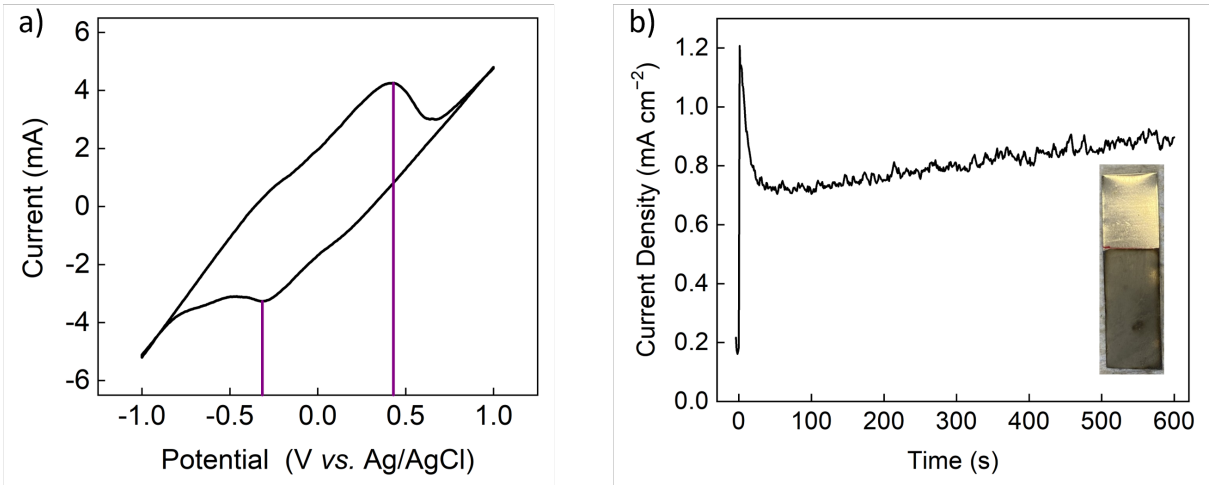

Figure 4.4: a) Cyclic voltammogram of 0.5 m/v % $PtCl_4$ in a three-electrode set-up (Ni plate as the working electrode, leak-free Ag/AgCl as the reference electrode, and graphite rod as the counter electrode), at a scan rate of 25 mV s^{-1}; purple drop lines represent the reduction (-0.315 $V_{Ag/AgCl}$) and oxidation (0.43 $V_{Ag/AgCl}$) peaks. b) Bulk electrolysis to coat a Pt layer on Ni at -0.315 $V_{Ag/AgCl}$. An inset photograph of the as-synthesised NiPt plate is also shown.

$$Pt^{4+} + 2e^- \rightleftharpoons Pt^{2+} \tag{4.2}$$

$$Pt^{2+} + 2e^- \rightleftharpoons Pt \tag{4.3}$$

4.3.2 Characterisation

Following their synthesis, the NiCuPt and NiPt films were characterised by X-ray diffraction (XRD), scanning electron microscopy (SEM) with elemental mapping, and X-ray photoelectron spectroscopy (XPS).

4.3.2.1 Morphology

SEM and elemental mapping were employed to investigate the surface of the catalysts. SEM images of NiCuPt at increasing magnifications are shown in Figure 4.5. Similarly to the NiCu electrocatalyst, bulbous florets of Cu nanoparticles can be seen on the Ni surface. The coating appears to be evenly spread across the electrode surface however some gaps in the coating can be seen at the lowest magnification. The highest magnification image, Figure 4.5c, shows that the florets consist of an agglomeration of nanocubes. This indicates the presences of many different binding sites, for example steps, terraces and edges.

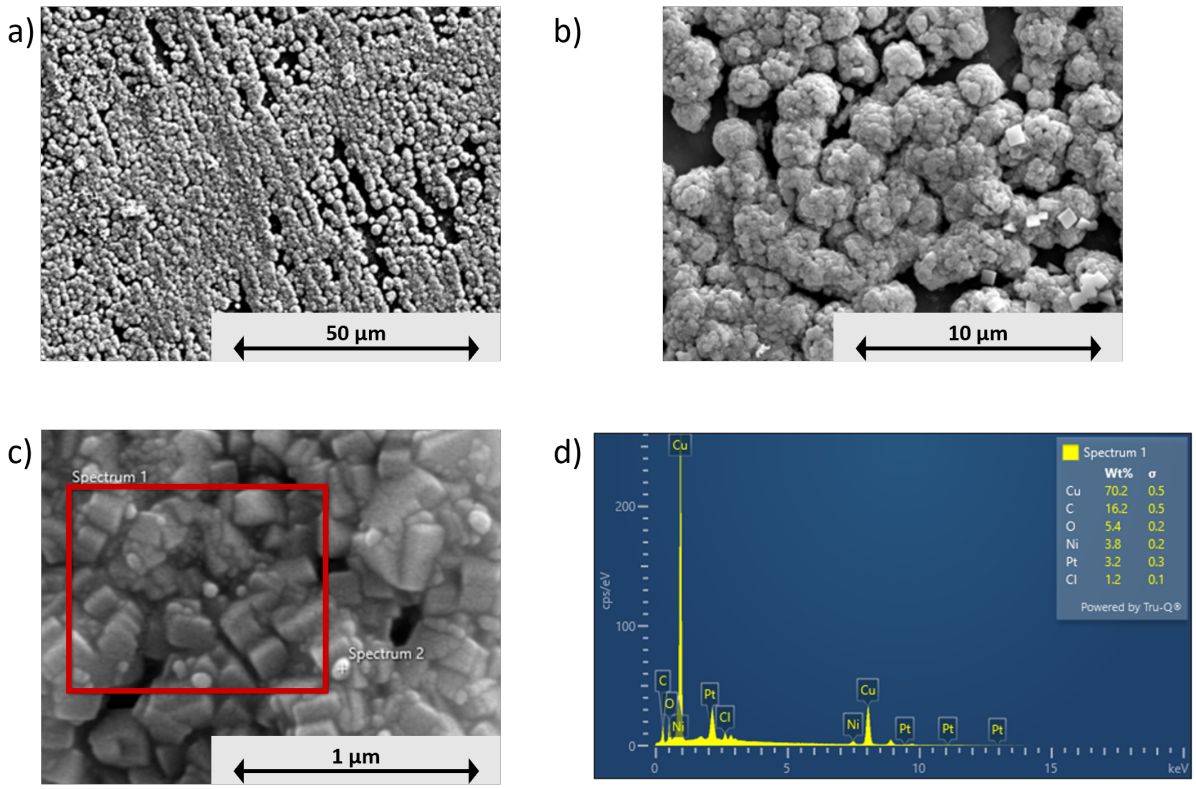

Figure 4.5: a–c) SEM images of NiCuPt at increasing magnification. d) An energy-dispersive spectroscopy spectrum of the NiCuPt electrode for the area shown in c).

The EDX analysis, Figure 4.5d, confirms the presence of disperse platinum across the surface. Platinum contributes an average of 3.1 wt.% to the composition, measured across 3 different regions of the catalyst plate. Individual elemental colour maps and an overlaid SEM colour map are shown in Figure 4.6. This confirms that no particular morphological

species can be attributed to the Pt layer. The Pt coating is present across the bulbous florets. This implies that the galvanic replacement of Pt does not significantly change the morphology of the underlying Cu layer. Any Pt coated is indistinguishable from the Cu without elemental analysis.

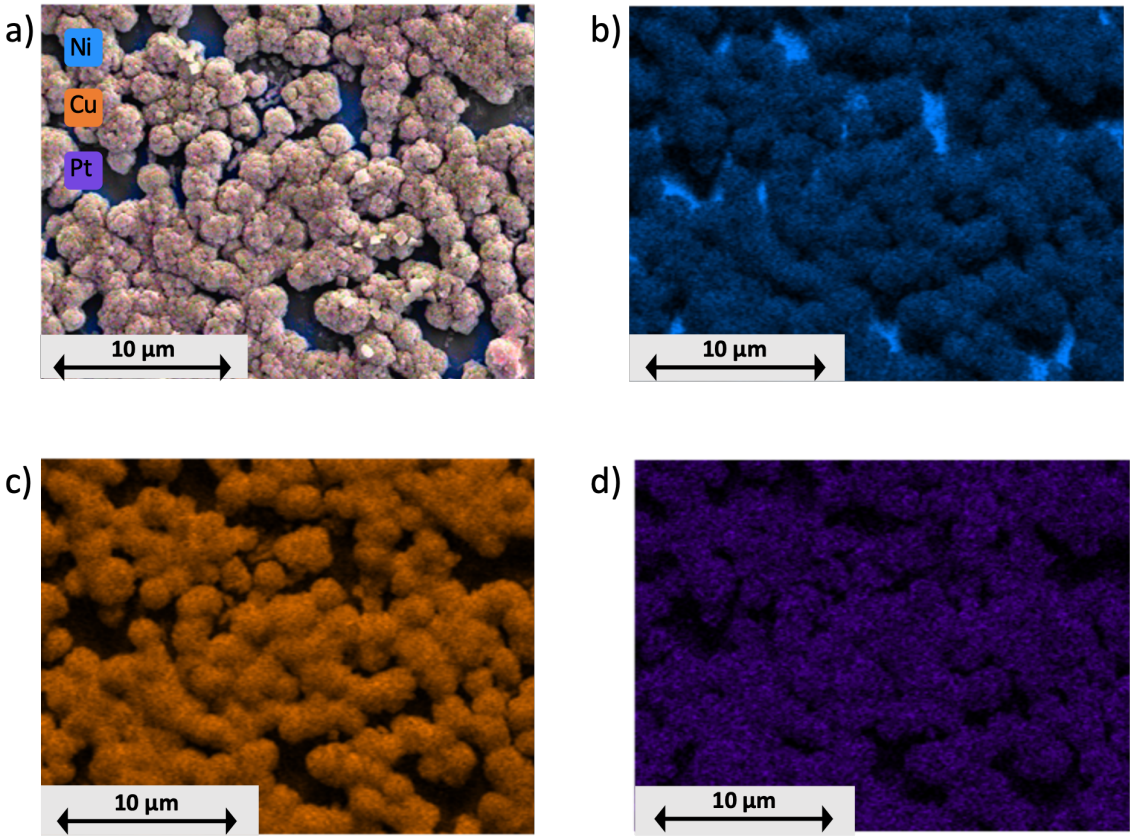

Figure 4.6: a) Combined SEM image and EDX analysis colour map of NiCuPt. Individual EDX analysis maps for b) nickel c) copper, and d) platinum. For elemental maps: blue corresponds to Ni, orange to Cu and purple to Pt.

SEM images of NiPt at increasing magnifications are shown in Figure 4.7. A layer of spherical Pt particles can be seen on the Ni surface. The coating appears to be fairly uniform across the imaged area however some areas look to be peeling away from the surface. This is especially noticeable in the top left corner of Figure 4.7b. Additionally areas of no Pt can be seen as apparent craters such as that in the bottom right quadrant of Figure 4.7a. Despite these features the Pt coating was consistent across multiple imaged spots. The EDX analysis, Figure 4.7d, confirms that the electrode if composed of primarily

Pt, 72 wt.% averaged across four sites, alongside the expected Ni, Cl, C, and O. The presence of Cl in the EDX spectrum suggests that a small amount has been coated amongst the Pt coating. For easy comparison, the Pt content and morphology of the NiCuPt and NiPt catalysts are given in Table 4.3

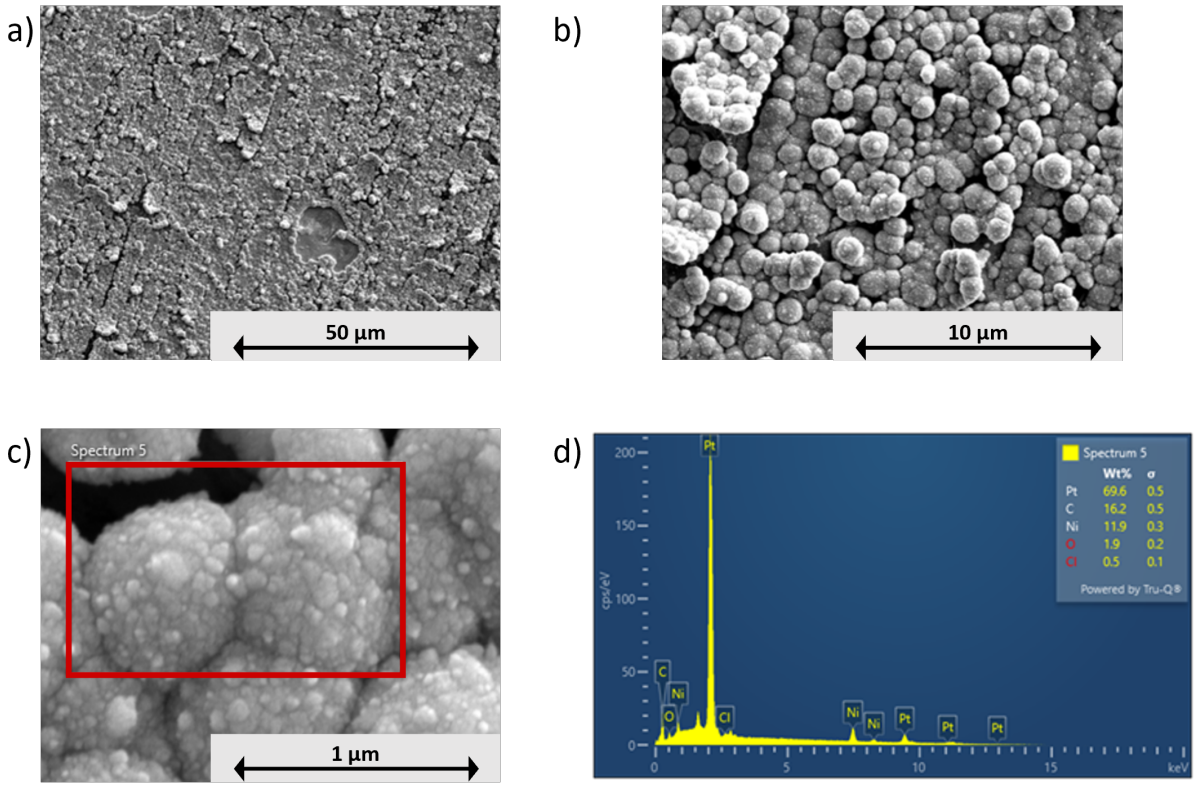

Figure 4.7: a–c) SEM images of NiPt at increasing magnification. d) Energy-dispersive spectroscopy spectrum of the NiPt electrode for the area shown in c).

Individual elemental colour maps and an overlaid SEM colour map are shown in Figure 4.8. This confirms that the spherical nanoparticles are Pt, and that some areas of Ni can be detected within or behind those spheres. Disperse Cl was also detected yet no distinct morphological features can be attributed to Cl. This further alludes to the idea that small amounts of Cl were coating during the Pt electrodeposition.

Table 4.3: Average Pt loading and morphology for the NiCuPt and NiPt catalysts as determined by SEM/EDX.

Catalyst	Pt Content/ wt.%	Pt Morphology
NiCuPt	3.1	Bulbous florets
NiPt	72	Spherical particles

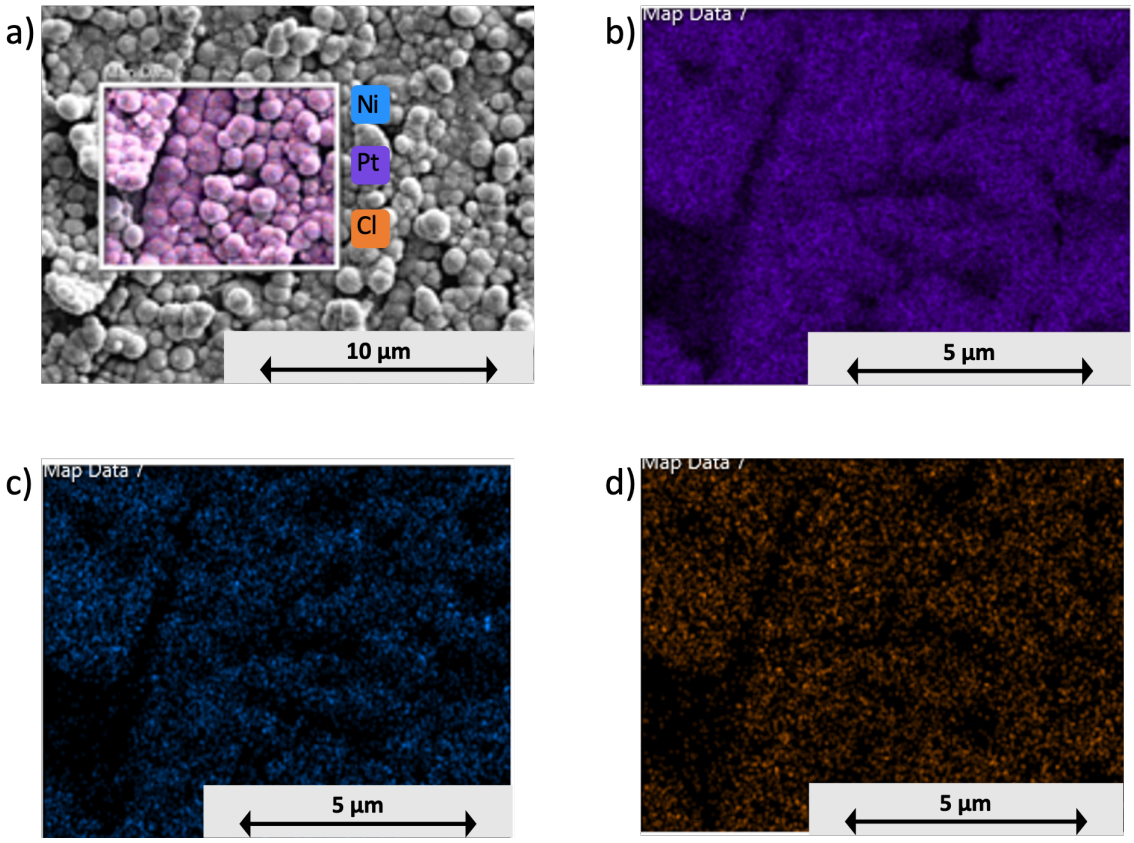

Figure 4.8: a) Combined SEM image and EDX analysis colour map for an area of NiPt. Individual EDX analysis maps for b) platinum c) nickel, and d) chlorine. For elemental maps: blue corresponds to Ni, purple to Pt, and orange to Cl.

4.3.2.2 Composition

Figure 4.9 compares the XRD patterns of the Ni plate and as-synthesised NiCuAg catalyst against the newly synthesised NiCuPt and NiPt catalysts. The peaks predominantly relate to the corresponding pure metals as defined by the PDF cards (Ni PDF no. 9013029, Cu PDF no. 9013023 and Pt PDF no. 9013023). Several peaks relating to metal oxides are also observed. For both catalysts Ni produces three key peaks at 43.7°, 51.1° and 75.7°; these can clearly be seen in the diffraction pattern as they are the highest intensity peaks. This comes as no surprise since Ni is the base of the catalysts and the thickest layer in each electrode stack. Standard Cu peaks appear at 42.6°, 49.7° and 73.5° for the NiCuPt electrode. These peaks are present in the sample at somewhat low intensity, which is consistent with the difference in layer thickness between the Cu layer and the Ni plate. No evidence of metallic Pt is seen in the NiCuPt spectrum, however two peaks relating

to Pt_3O_4 can be observed at 35.7° and 76.0°. Due to the low concentration and coating time used in the galvanic replacement of Pt to produce the NiCuPt stack there may be no metallic Pt present on the electrode or it could be highly disperse and thus undetectable by XRD. The lack of detected Pt also explains the increased Cu intensities in the NiCuPt spectrum compared to NiCuAg as the top Pt layer is not sufficiently thick enough to impede the exposure of the surface Cu.

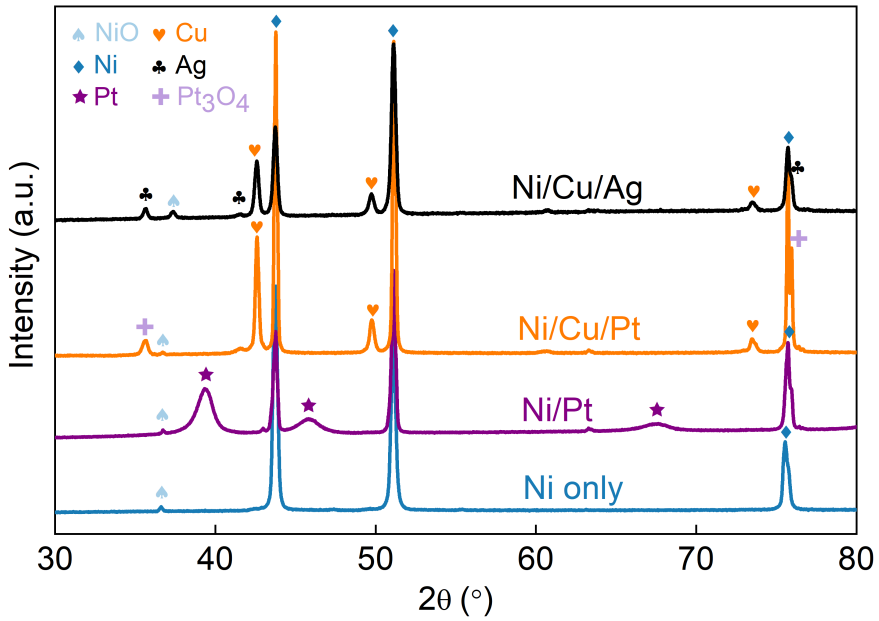

Figure 4.9: Stacked XRD patterns for NiPt and NiCuPt. The diffraction patterns for Ni and NiCuAg, measured as part of Chapter 3, are added for comparison. Blue diamonds signify peaks relating to Ni (PDF no. 9013029), pale blue spades signify NiO peaks (PDF no. 9008693), orange hearts represent Cu peaks (PDF no. 9013023), purple stars indicate Pt peaks (PDF no. 1011103), pale purple crosses represent Pt_3O_4 (PDF no. 1008965), and black clubs signify Ag peaks (PDF no. 9013047).

For the NiPt sample, peaks relating to metallic Pt are present at 39.3°, 45.9° and 67.75°. These appear as broad reflections as a result of their nanocystalline nature.[47] In general peaks become sharper as crystals become larger.[48] It is clear from the XRD that the Pt layer has been successfully coated and no major impurity peaks are present in the NiPt electrode save for some NiO.

4.3.2.3 Surface Analysis

The chemical states and surface electronic structure of the NiCuPt and NiPt plates were detected by X-ray photoelectron spectroscopy. This allowed the identification of surface oxides and other species which are present in low quantities and/or are hard to detect by other bulk techniques. Figure 4.10 shows that the survey spectra of the NiCuPt and NiPt electrodes. Both spectra indicate the presence of C (285 eV, C 1s) highlighted in red, and O (531 eV, O 1s) highlighted in green. The NiPt scan clearly shows the key peaks relating to Pt (530 eV-Pt $4p_{3/2}$, 331 eV-Pt $4d_{3/2}$, 315 eV-Pt $4d_{5/2}$, 70 eV-Pt 4f) highlighted in purple, however the NiCuPt scan only evinces the Pt 4f signal. This is logical as, in addition to the low Pt loading confirmed by EDX, the signal relating to the photoelectrons typically gives the most intense signal. Furthermore, the peak at around 70 eV in the NiCuPt sample may be enhanced due to the high Cu content of the sample, as this is also the expected region for the Cu 3p peaks.

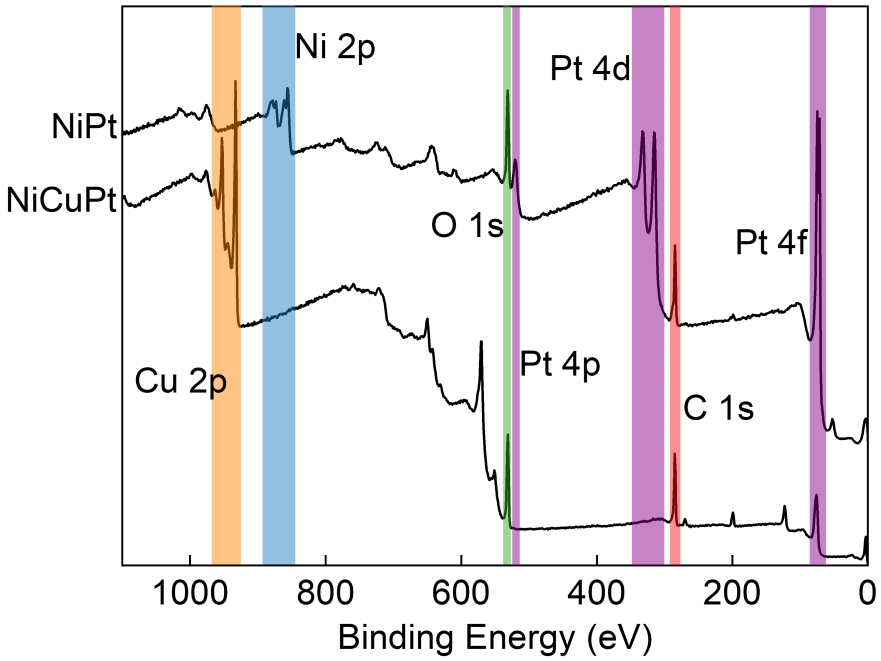

Figure 4.10: X-ray photoelectron spectroscopy survey spectra of top, NiPt and bottom, NiCuPt.Peak assignments were made using the NIST X-ray Photoelectron Spectroscopy Database,[49] and Perkin-Elmer Handbook of X-ray Photoelectron Spectroscopy.[50]

The NiPt spectrum also shows the photoelectron peaks relating to Ni (890-855 eV, Ni 2p) highlighted in blue. No Ni 2p signal can be seen in the NiCuPt spectrum, this suggests that the Cu and Pt coatings are sufficiently thick that the Ni below can no longer be detected. A similar effect was seen in the NiCuAg system. The final set of highlighted peaks, in orange, relate to the Cu (962-932 eV, Cu 2p) present in the NiCuPt sample.

The deconvoluted high-resolution spectra for Cu and Pt within the NiCuPt stack, Figure 4.11, reveal further detail about the coated species. Binding energies and peak assignments are given in Table 4.4. The Cu spectrum, Figure 4.11a, focused on the Cu 2p region, showing the peaks from both Cu $2p_{3/2}$ and Cu $2p_{1/2}$. The binding energy difference between the Cu $2p_{1/2}$ and Cu $2p_{3/2}$ peaks with the highest intensity was 19.8 eV: this is typical of metallic Cu.[50] The largest peaks at 932.9 and 952.7 eV are thus assigned to metallic Cu. This suggests the majority of the Cu coated layer consisted of metallic Cu. However, secondary peaks which can be related to CuO are also seen within the spectrum. Thus Cu oxide species were also present on the electrode; it is likely that they resulted from oxidation in the air whilst drying after the Cu electrodeposition and prior to Pt galvanic replacement.

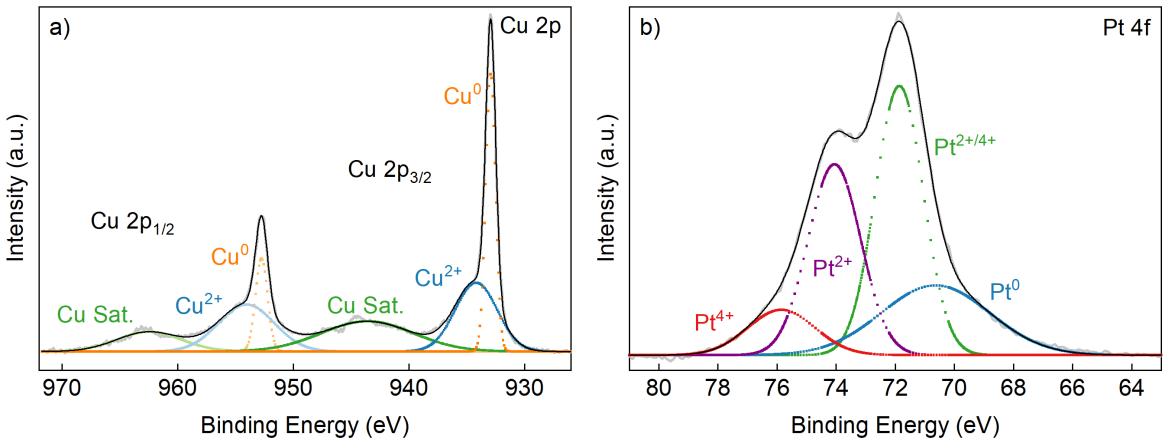

Figure 4.11: Deconvoluted high resolution XPS spectrum of the a) Cu 2p region and b) Pt 4f region for the NiCuPt catalyst. Data analysis and fittings were performed in Originlab software. Peak assignments were made using the NIST X-ray Photoelectron Spectroscopy Database,[49] and Perkin-Elmer Handbook of X-ray Photoelectron Spectroscopy.[50]

The Pt 4f spectrum, Figure 4.11b, proved difficult to deconvolute as the region overlaps with the Cu 3p region, typically found at 75 eV. Therefore the deconvolution may contain some inaccuracies.[51] The peaks are predominantly assigned to oxide species, PtO and PtO_2 alongside the galvanic replacement solution species, $PtCl_4$. The presence of oxides concurs with the results seen by XRD and EDX. It is evident that Pt exists in several common oxidation states within the coating, however a peak relating to metallic Pt was seen at 70.6 eV.

Table 4.4: XPS binding energies for the NiCuPt catalyst stack. Binding energies calculated relative to C 1s = 285.0 eV.

Element	**Binding Energy / eV**	**Assignment**	**References**
Cu $2p_{3/2}$	932.9	Cu^0	[52]
	934.2	Cu^{2+}–CuO	[53]
	943.6	Cu^{2+}–satellites	[53,54]
Cu $2p_{1/2}$	952.7	Cu^0	[55]
	954.1	Cu^{2+}–CuO	[50,56]
	962.5	Cu^{2+}–satellites	[54]
Pt $4f_{7/2}$	70.6	Pt^0–Cu/Pt	[57]
	71.9	$Pt^{2/4+}$–PtO_x	[58]
	74.1	Pt^{4+}–PtO_2	[59]
	75.9	Pt^{4+}–$PtCl_4$	[60]

The deconvoluted high-resolution spectra for Ni and Pt from the NiPt electrode are shown in Figure 4.12. Binding energies and peak assignments are given in Table 4.5. The Ni spectrum, Figure 4.12a, displays the Ni 2p region. The binding energy difference between the largest peaks in the $2p_{1/2}$ and $2p_{3/2}$ regions respectively is 17.6 eV. This spin orbit splitting is often cited as characteristic of either $Ni(OH)_2$ [61] or NiO.[62] The highest intensity peak, at 855.6 eV, is attributed to $Ni(OH)_2$, whilst the smaller peak at 857.3 eV is assigned to NiO. Small peak resulting from metallic Ni is also seen at 853.3 eV. Since the maximum XPS measurement depth is around 5 nm, it is likely that the majority of the metallic Ni present in the electrode cannot be detected. The plate itself is too thick, especially with the Pt coating on top.

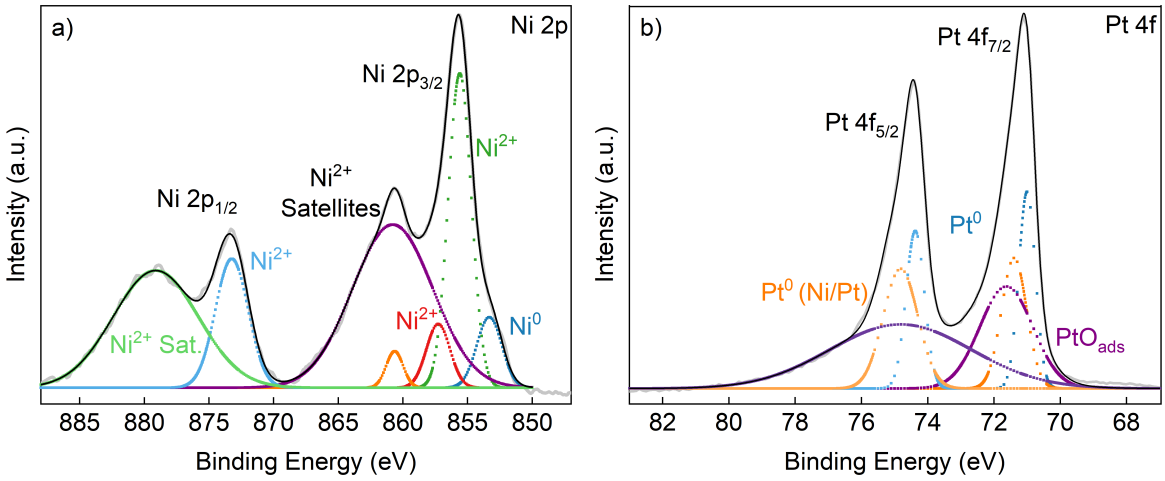

Figure 4.12: Deconvoluted high resolution XPS spectrum of the a) Ni 2p region and b) Pt 4f region for the NiPt catalyst. Data analysis and fittings were performed in Originlab software. Peak assignments were made using the NIST X-ray Photoelectron Spectroscopy Database,[49] and Perkin-Elmer Handbook of X-ray Photoelectron Spectroscopy.[50]

The Pt spectrum, Figure 4.12b, displays the Pt 4f region, compared with the Pt region of the NiCuPt plate this spectrum can easily be divided into the $4f_{5/2}$ and $4f_{7/2}$ regions. The binding energy difference between the largest peaks from each region is 3.4 eV. This is typical for metallic Pt. Secondary metallic Pt peaks at 71.4 and 74.8 eV are assigned to Pt on Ni. This likely results from the Pt directly on the Ni surface, whilst the other Pt^0 peaks result from Pt coated on top of other Pt. This suggests there is a significant coating of Pt, enough to produce two slightly different signals. The final peaks in the Pt 4f spectrum results from adsorbed PtO, which possibly formed following the Pt electrodeposition by oxidation whilst drying in air.

Table 4.5: XPS binding energies for the NiPt catalyst stack. Binding energies calculated relative to C 1s = 285.0 eV.

Element	Binding Energy / eV	Assignment	References
Ni $2p_{3/2}$	853.3	Ni^0	63
	855.6	Ni^{2+}–$Ni(OH)_2$	64
	857.3	Ni^{2+}–NiO	65
	860.6	Ni^{2+}–satellites	64
	860.8	Ni^{2+}–satellites	66
Ni $2p_{1/2}$	873.2	Ni^{2+}–NiO	67
	879.1	Ni^{2+}–satellites	67
Pt $4f_{7/2}$	71.0	Pt^0	68
	71.4	Pt^0–Ni/Pt	69
	71.6	Pt^{2+}–PtO_{ads}	70
Pt $4f_{5/2}$	74.4	Pt^0	68
	74.8	Pt^0–Ni/Pt	69
	74.8	Pt^{2+}–PtO_{ads}	70

4.3.3 Electrochemical Testing

4.3.3.1 Linear Sweep Voltammetry

The performance of the bare Ni plate as a cathode for the electrochemical hydrogen evolution reaction was probed in acidic, neutral and basic conditions. Figure 4.13 shows how the current density varied with applied potential in a) acidic, b) neutral, and c) basic conditions. As the potentials are converted to the reversible hydrogen electrode, the overpotential can be found by reading off the potential at which the sweep reaches a given current density. For all catalysts, the overpotential was calculated as an average from the linear sweep voltammograms of three individual electrodes. This approach minimized the impact of any differences in coating quality or area between the sequentially prepared catalyst plates. In acidic media the Ni plate has an average overpotential of -465 ± 19 mV at -10 mA cm^{-2} and -581 ± 30 mV at -100 mA cm^{-2}. Under neutral conditions the average overpotential was -790 ± 76 mV at -10 mA cm^{-2} and -1085 ± 123 mV at -100

mA cm^{-2}. These overpotentials are significantly larger than those in acidic or basic media because the neutral pathway for hydrogen evolution is more complicated. The pathway is not dependant on a single reactant or intermediate. At low overpotentials the low concentration of available H^+ at the electrode interface is able to maintain the reaction, however as this becomes depleted a pH gradient is created at the electrode surface and the reaction becomes diffusion controlled.[71] Therefore, at higher overpotentials the key reactant switches to H_2O from H_3O^+.[72] The Ni plate has the lowest overpotentials at both -10 mA cm^{-2} and -100 mA cm^{-2} in basic media at -415 ± 51 mV and -565 ± 29 mV respectively. Bare Ni is used as the substrate, thus we can compare the catalysts with additional layers to these values.

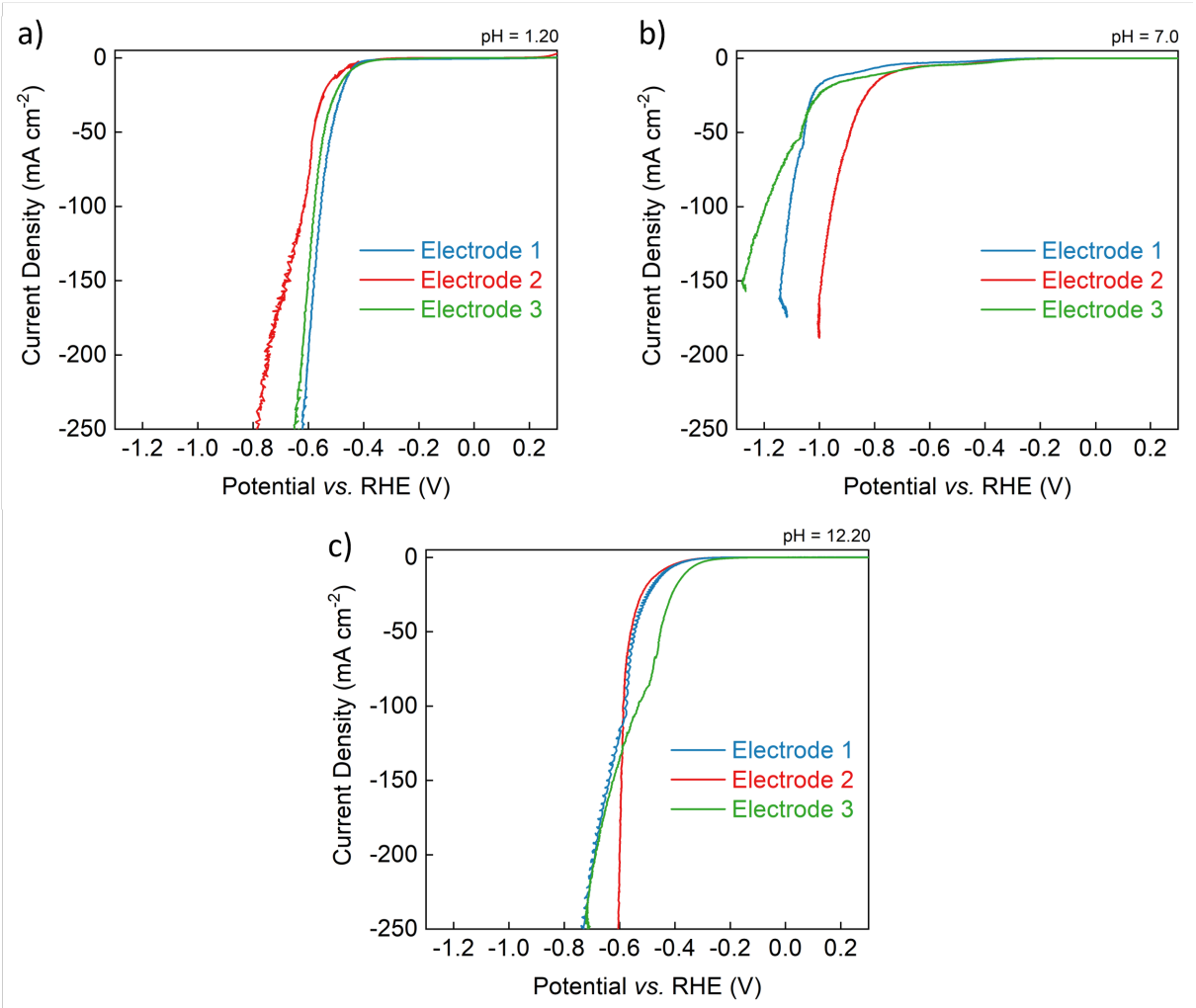

Figure 4.13: Linear sweep voltammetry at a scan rate of 2 mV s^{-1} of bare Ni in a) 0.1 M H_2SO_4, b) 0.1 M phosphate buffer, and c) 0.1 M KOH. The pH of the solutions used in each case are given at the top right of each graph.

Figure 4.14 shows the linear sweep voltammograms for the NiCu catalyst in a) acidic, b) neutral, and c) basic conditions. Under acidic conditions the NiCu catalyst has an average overpotential of -525 ± 7 mV at -10 mA cm^{-2} and -640 ± 9 mV at -100 mA cm^{-2}. This is a larger overpotential compared to the bare Ni plate under these conditions, however this is expected, considering that Ni and Cu are near neighbours on Trassati's volcano plot.[17] Thus the combination of Ni and Cu is likely to result in a lower M−H bond strength compared to Ni, further away from the optimum value. In neutral electrolyte the average overpotential was -689 ± 21 mV at -10 mA cm^{-2} and -949 ± 61 mV at -100 mA cm^{-2}. These values are lower (in absolute terms) than the bare Ni plate suggesting that NiCu could be a better catalyst for hydrogen evolution in these conditions. In basic conditions the NiCu electrode has an average overpotential of -503 ± 25 mV at -10 mA cm^{-2} and -747 ± 43 mV at -100 mA cm^{-2}. This initially suggests that NiCu has the lowest overpotential in basic electrolyte, however by increasing the current density from which the overpotential is measured to -100 mA cm^{-2} it can be seen that the overpotential is lowest in acidic conditions.

Figure 4.15 shows the linear sweep voltammograms for the NiCuAg catalyst in a) acidic, b) neutral, and c) basic conditions. Under acidic conditions the NiCuAg catalyst has an average overpotential of -507 ± 28 mV at -10 mA cm^{-2} and -616 ± 22 mV at -100 mA cm^{-2}. Under neutral conditions the average overpotential was -664 ± 39 mV at -10 mA cm^{-2} and -1070 ± 80 mV at -100 mA cm^{-2}, and in basic electrolyte the average overpotential was -454 ± 62 mV at -10 mA cm^{-2} and -656 ± 68 mV at -100 mA cm^{-2}. Thus, the lowest overpotential for the NiCuAg electrode at -10 mA cm^{-2} is in basic conditions, however at the more industrially relevant current density of -100 mA cm^{-2}, the lowest overpotential is seen in acidic media. Compared to the bare Ni electrode the three-layer NiCuAg catalyst has a lower activity for hydrogen evolution, yet the activity in acidic and basic media is increased compared to the two layer, NiCu catalyst.

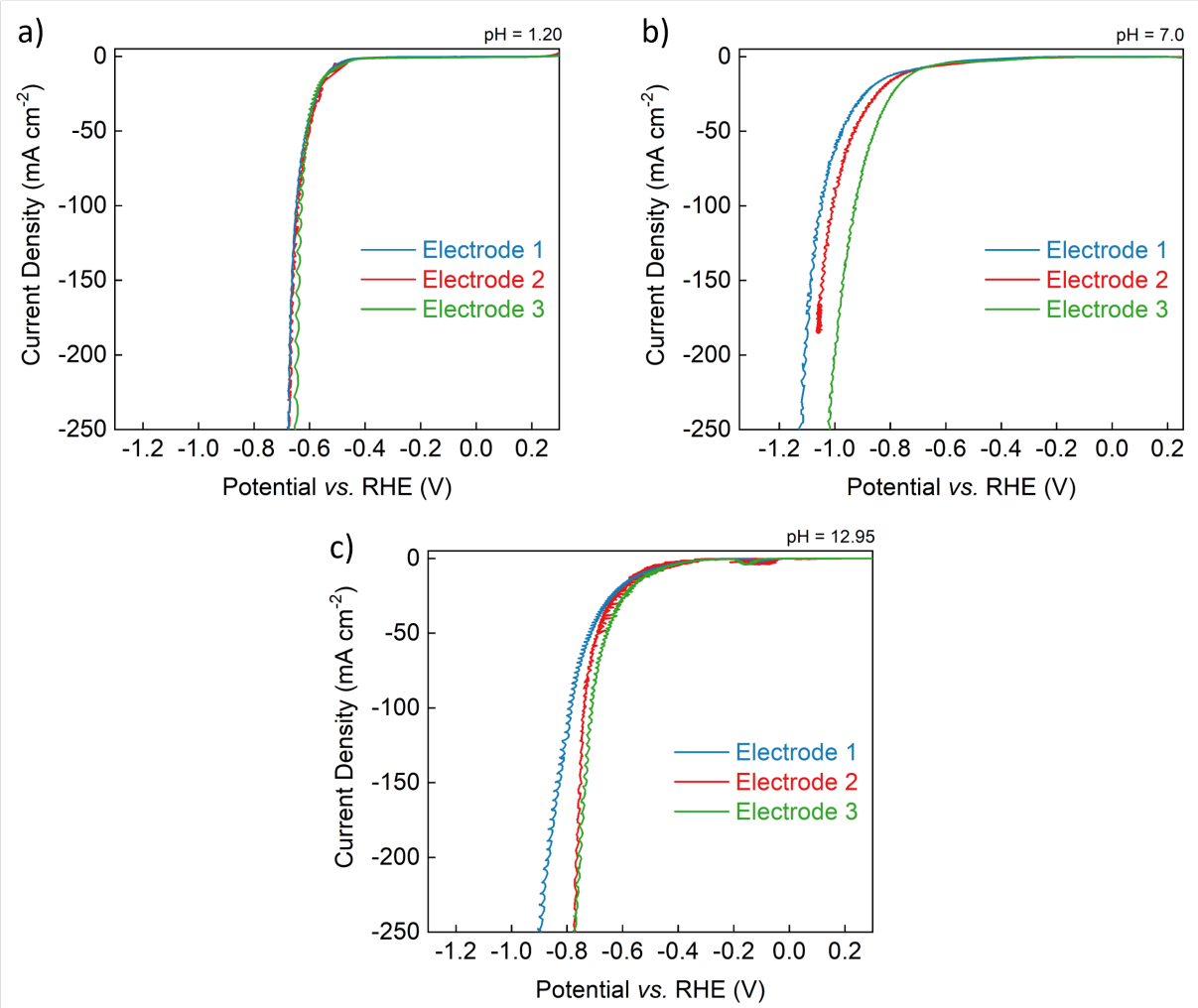

Figure 4.14: Linear sweep voltammetry at a scan rate of 2 mV s^{-1} of NiCu electrode in a) 0.1 M H_2SO_4, b) 0.1 M phosphate buffer, and c) 0.1 M KOH. The pH of the solutions used in each case are given at the top right of each graph.

Across all catalysts and electrolytes the lowest overpotential, at both current densities, for hydrogen evolution was measured on the bare Ni electrode in 0.1 M KOH. It is noteworthy that at low current densities the addition of the Cu and further Ag layers decreases the overpotential for hydrogen evolution in neutral media, compared to the bare Ni catalyst. At -100 mA cm^{-2} however the overpotential significantly decreases upon the addition of Cu to the Ni plate, whereas the overpotential increases, yet still lower than bare Ni, upon the addition of Ag to the NiCu stack.

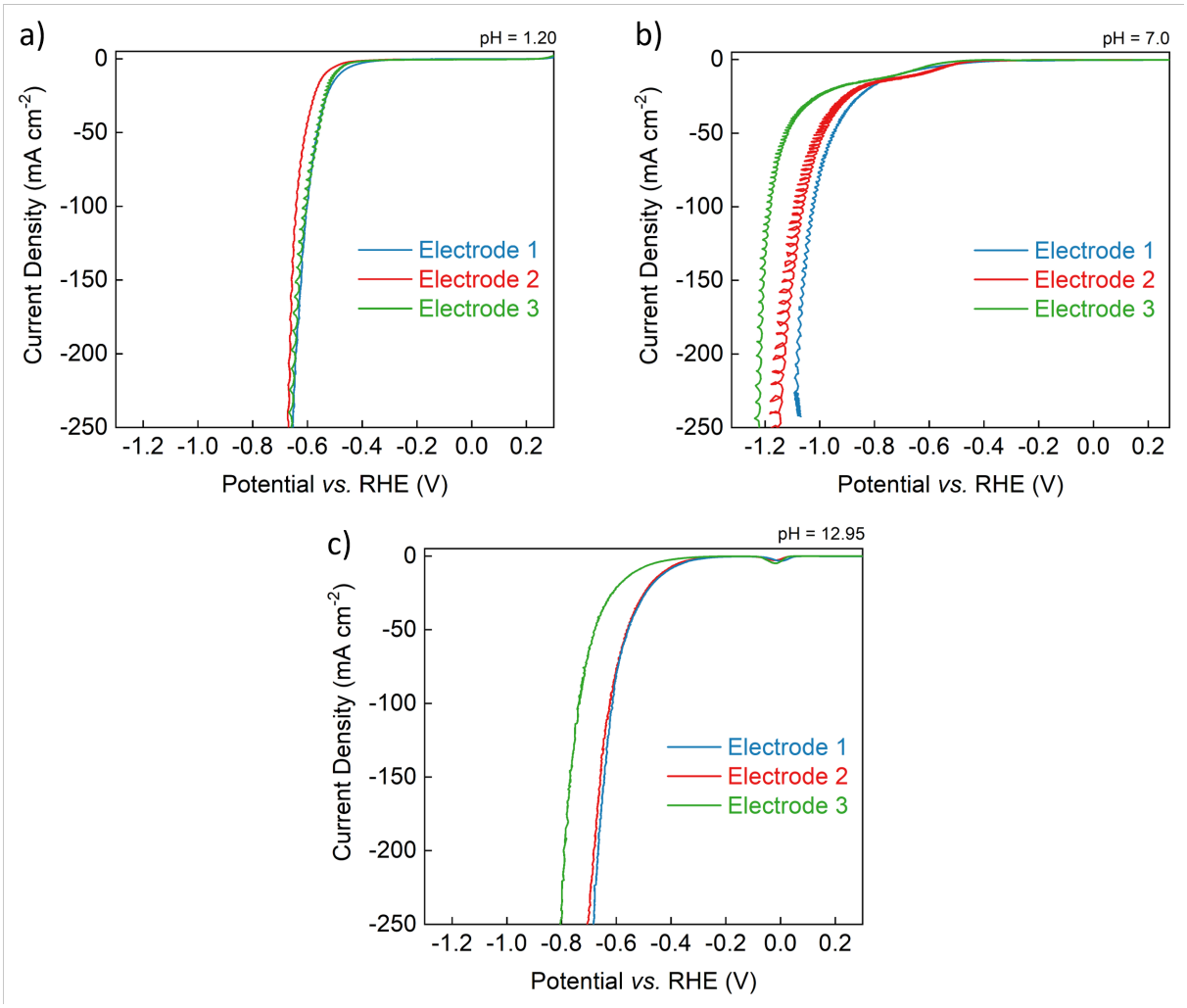

Figure 4.15: Linear sweep voltammetry at a scan rate of 2 mV s^{-1} of NiCuAg electrode in a) 0.1 M H_2SO_4, b) 0.1 M phosphate buffer, and c) 0.1 M KOH. The pH of the solutions used in each case are given at the top right of each graph.

The performance of the NiCuPt and NiPt catalyst plates were probed in acidic, and basic conditions as a cathode for the electrochemical hydrogen evolution reaction. Figure 4.16 shows how the current density varied with applied potential in a) acidic, and b) basic conditions for the NiCuPt electrode. In acidic conditions the NiCuPt catalyst has an average overpotential of -437 ± 11 mV at -10 mA cm^{-2} and -557 ± 21 mV at -100 mA cm^{-2}. As expected due to the inclusion of a thin layer of Pt, these overpotentials are lower than those measured for the bare Ni plate under the same conditions. In basic electrolyte NiCuPt has an average overpotential of -366 ± 63 mV at -10 mA cm^{-2} and -579 ± 67 mV at -100 mA cm^{-2}. Here, NiCuPt appears to be a better hydrogen

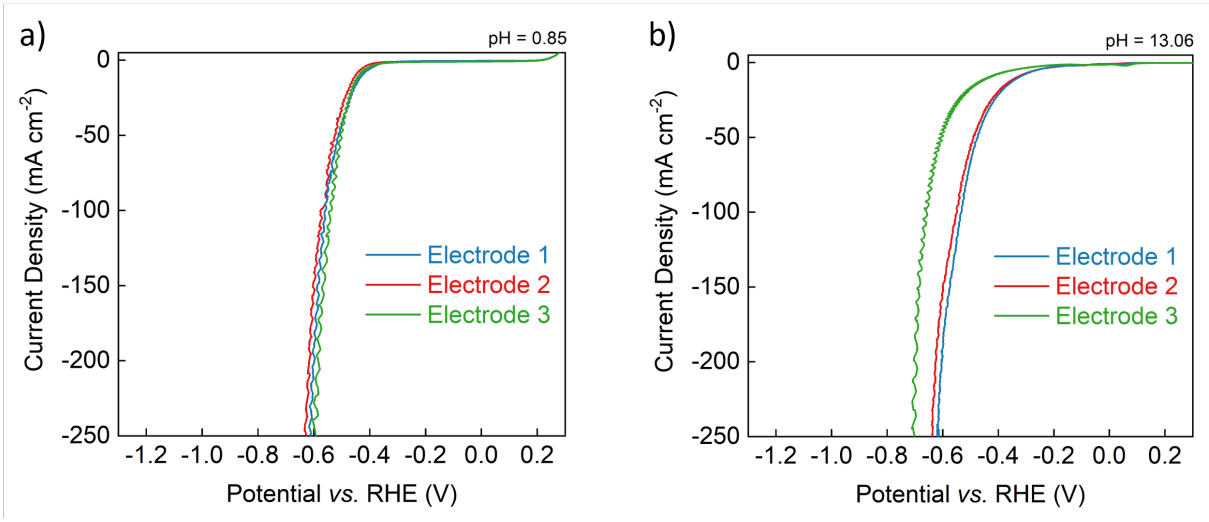

Figure 4.16: Linear sweep voltammetry at a scan rate of 2 mV s^{-1} of NiCuPt electrode in a) 0.1 M H_2SO_4, and b) 0.1 M KOH. The pH of the solutions used in each case are given at the top right of each graph.

evolution catalyst than Ni at -10 mA cm^{-2}, however at -100 mA cm^{-2} the overpotential for NiCuPt is higher (in absolute value) than bare Ni. This reinforces the importance of measuring the overpotential at various current densities, especially those which are more industrially relevant.

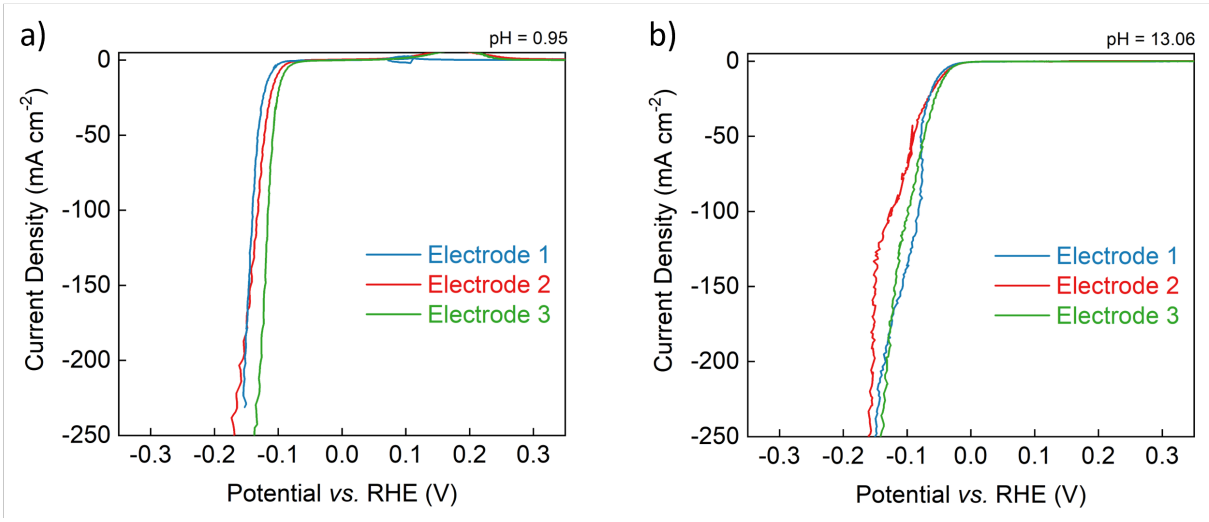

Figure 4.17: Linear sweep voltammetry at a scan rate of 2 mV s^{-1} of NiPt electrode in a) 0.1 M H_2SO_4, and b) 0.1 M KOH. The pH of the solutions used in each case are given at the top right of each graph.

Figure 4.17 shows how the current density varied with applied potential in a) acidic, and b) basic conditions for the NiPt electrode. In an acidic electrolyte the NiPt catalyst has an average overpotential of -102 ± 11 mV at -10 mA cm^{-2} and -129 ± 12 mV at -100 mA cm^{-2}. In basic conditions the average overpotential measured for NiPt was -45 ± 5

mV at -10 mA cm^{-2} and -102 ± 21 mV at -100 mA cm^{-2}. Regardless of the electrolyte, these overpotentials are significantly more promising than any of the previous catalysts tested. This concurs with work by Chen *et al.*,[41] that suggested that introducing even a monolayer of Pt can significantly benefit the hydrogen evolution activity.

4.3.3.2 Tafel Slopes

Tafel slopes were calculated from steady state current density readings extracted from stepped bulk electrolysis under potential control. Individual current densities for each overpotential measured were taken as an average of at least three stepped bulk electrolysis runs. The system was kept at each potential for 5 minutes, and the cathodic potential increased in 25 mV steps. This method is considered best practise in comparison to transient methods such as polarisation or linear sweep voltammetry.[73] This is because often Tafel analysis assumes extreme coverage of absorbed H at the electrode surface (either 0 or 1), this assumption is then embedded in the modelled Tafel slopes used to determine the rate determining step. In fact, coverage is potential-dependent,[74] thus allowing the system to reach a steady state before taking a measurement reduces inaccuracies.

Figure 4.18 shows the calculated Tafel slopes for each stage in the NiCuAg stack in acidic media. The addition of Cu to the Ni electrode increases the Tafel slope to -91.6 ± 4.1 mV dec^{-1} from -89.0 ± 4.2 mV dec^{-1}. Thus it can be inferred that the addition of Cu increases the strength of H adsorption thus preventing desorption and decreasing activity. In 0.1 M H_2SO_4 NiCuAg has the lowest Tafel slope at -50.0 ± 4.0 mV dec^{-1} suggesting that the addition of Ag encourages desorption of H and thus the activity is increased.

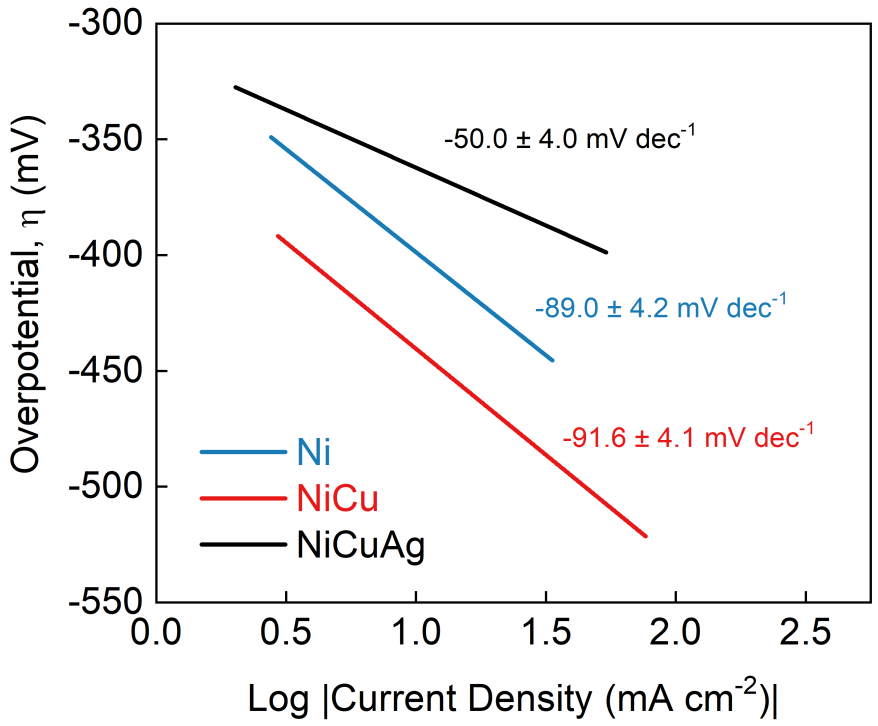

Figure 4.18: A representative Tafel plot for bare Ni (blue), NiCu (red), and NiCuAg (black) in 0.1 M H_2SO_4.

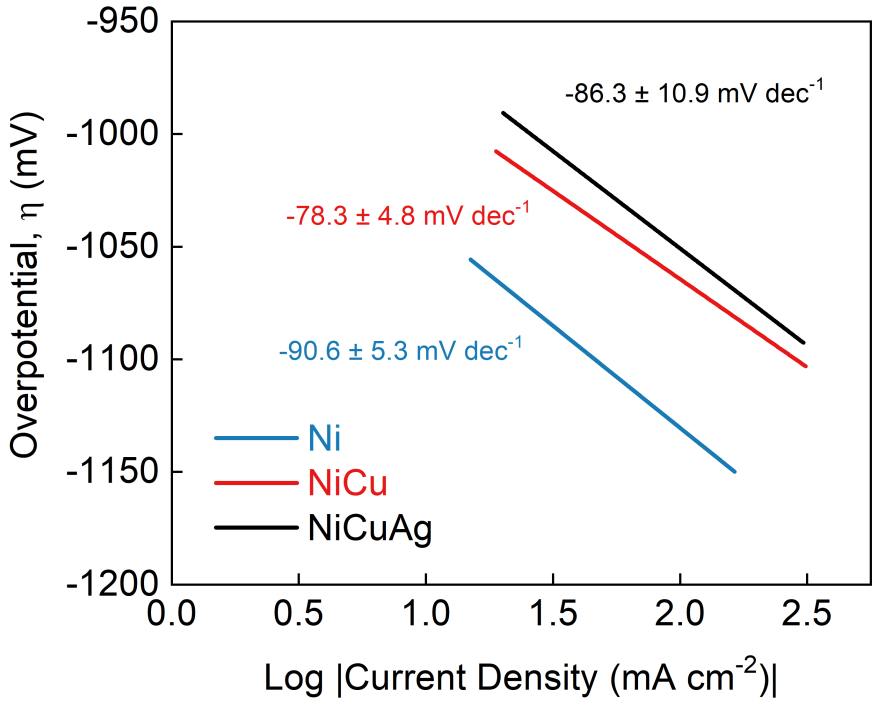

Figure 4.19: A representative Tafel plot for bare Ni (blue), NiCu (red), and NiCuAg (black) in 0.1 M KH_2PO_4/K_2HPO_4.

The calculated Tafel plots under neutral conditions for Ni, NiCu and NiCuAg are shown in Figure 4.19. Here, NiCu has the lowest Tafel slope at -78.3 ± 4.8 mV dec^{-1}, however, the addition of Cu and Ag layers still decreases the Tafel slope, -86.3 ± 10.6 mV dec^{-1} compared to bare Ni, -90.6 ± 5.3 mV dec^{-1}. Despite these values being considered average in the wider literature, the overpotential at which hydrogen evolution must take place makes these catalysts not viable under these conditions.

Figure 4.20 shows the calculated Tafel slopes for bare Ni, NiCu and NiCuAg in basic electroltye. The addition of each further layer to the catalyst increased the Tafel slope. The Tafel slopes for both the NiCu and NiCuAg electrode are over 140 mV dec^{-1}, this indicates that both catalysts have the Volmer step, equation 4.4, as the rate determining step.

$$H_2O + e^- \rightleftharpoons H_{ad} + OH^- \tag{4.4}$$

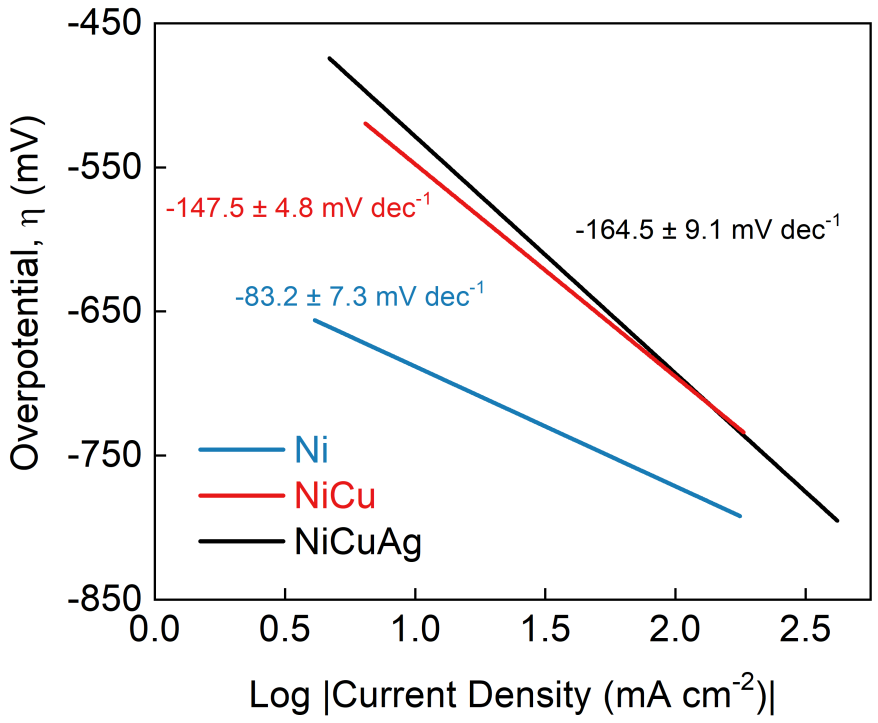

Figure 4.20: A representative Tafel plot for bare Ni (blue), NiCu (red), and NiCuAg (black) in 0.1 M KOH.

In contrast, Figure 4.21 shows the calculated Tafel slopes for the Pt containing catalysts, NiCuPt and NiPt in basic conditions. The Tafel slope values are -108.7 ± 3.4 mV dec^{-1} for NiCuPt and -51.8 ± 2.7 mV dec^{-1} for NiPt. The large difference between the values for these two catalysts suggests that their kinetics are controlled by different elemental steps of the hydrogen evolution reaction. The rate determining step for each catalyst is different. The NiPt catalyst is controlled by the Heyrovsky step, the addition of a proton to an adsorbed H, whilst the NiCuPt catalyst is dictated by the Volmer step, the adsorption of H. This difference in rate determining step suggests a difference in the active sites of the catalysts. This is contrary to the work of Chen *et al.*, who suggested that a monolayer of Pt would be enough to exhibt Pt-like behaviour.[41] Clearly the different amounts of Pt present on these two catalysts effects their activity.

The addition of Pt to the NiCu catalyst has significantly decreased its Tafel slope, as expected. However it is still higher than the Tafel slope of bare Ni under the same conditions. This indicates that the Cu containing catalysts are not significantly promising in basic conditions. The electrodepositied NiPt catalyst, however does show some promise in KOH.

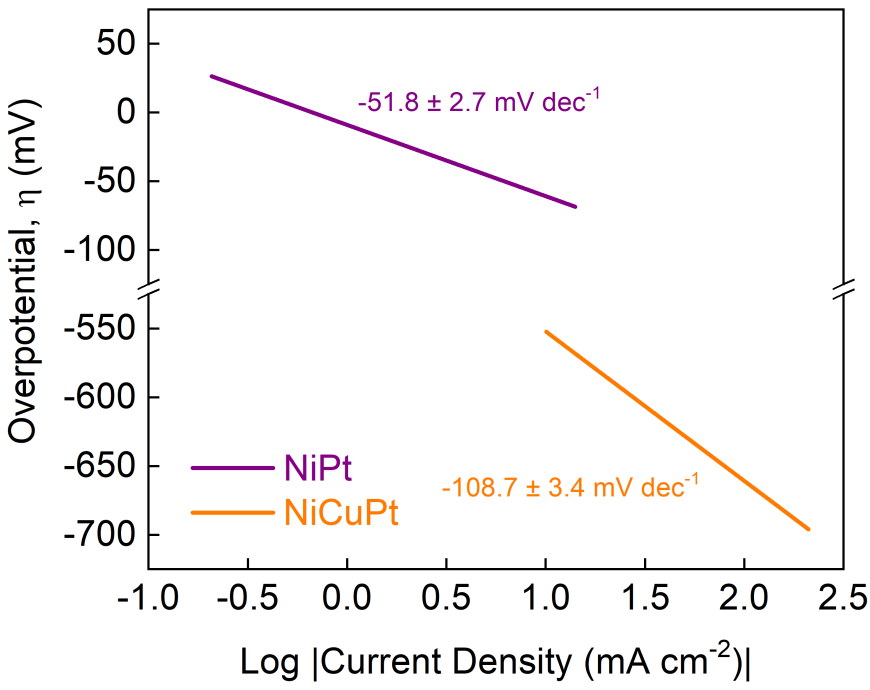

Figure 4.21: A representative Tafel plot for NiCuPt (orange), and NiPt (purple) in 0.1 M KOH.

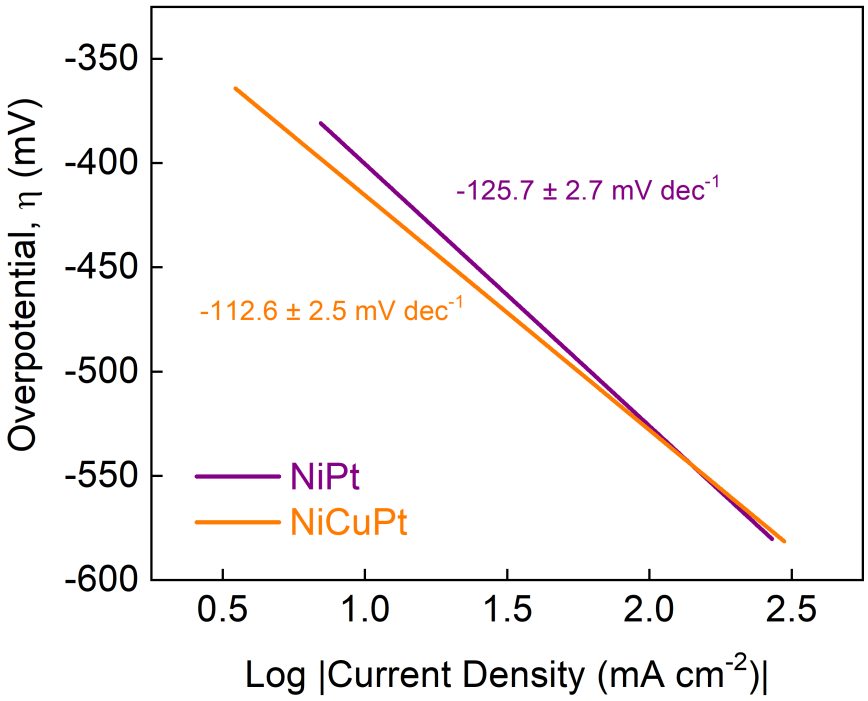

Figure 4.22: A representative Tafel plot for NiCuPt (orange), and NiPt (purple) in 0.1 M H_2SO_4.

Figure 4.22 shows the calculated Tafel slopes for the Pt containing catalysts, NiCuPt and NiPt in acidic conditions. The Tafel slope values are -112.6 ± 2.5 mV dec^{-1} for NiCuPt and -125.7 ± 2.7 mV dec^{-1} for NiPt. These values are both close to 120 mV suggesting that adsorption onto the catalysts surface is the rate determining step. This could be partially due to a lack of available protons for adsorption at the electrode/electrolyte interface.

The overpotentials measured at -10 mA cm^{-2}, η_{10} and -100 mA cm^{-2}, η_{100}, for all catalysts under all reaction conditions tested are summarised in Table 4.6; the calculated Tafel slope vales are also given for easy comparison. This confirms that NiPt displayed the best activity for hydrogen evolution in both acid and base. It can also be seen that the addition of Cu and Ag layers to Ni is more beneficial than the addition of Cu alone. Evaluation of the calculated parameters also signifies that optimising the layer loadings, particularly for NiCuPt, could increase hydrogen evolution activity, especially given that NiPt was characterised to have a considerably denser Pt coating than NiCuPt.

Table 4.6: Summary of overpotentials and Tafel slopes of all catalysts tested in a) 0.1 M H_2SO_4, b) 0.1 M KOH, and c) 0.1 M KH_2PO_4/K_2HPO_4

a) 0.1 M H_2SO_4			
Catalyst	η_{10} / **mV**	η_{100} / **mV**	**Tafel / mV dec^{-1}**
Ni	-465 ± 19	-581 ± 30	-89.0 ± 4.2
NiCu	-525 ± 7	-640 ± 9	-91.6 ± 4.1
NiCuAg	-507 ± 28	-616 ± 22	-50.0 ± 4.0
NiCuPt	-437 ± 11	-557 ± 21	-112.6 ± 2.5
NiPt	-102 ± 11	-129 ± 12	-125.7 ± 2.7

b) 0.1 M KOH			
Catalyst	η_{10} / **mV**	η_{100} / **mV**	**Tafel / mV dec^{-1}**
Ni	-415 ± 51	-565 ± 29	-83.2 ± 7.3
NiCu	-503 ± 25	-747 ± 43	-147.5 ± 4.8
NiCuAg	-454 ± 62	-656 ± 68	-164.5 ± 9.1
NiCuPt	-366 ± 63	-579 ± 67	-108.7 ± 3.4
NiPt	-45 ± 5	-102 ± 21	-51.8 ± 2.7

c) 0.1 M KH_2PO_4/K_2HPO_4			
Catalyst	η_{10} / **mV**	η_{100} / **mV**	**Tafel / mV dec^{-1}**
Ni	-790 ± 76	-1085 ± 123	-90.6 ± 5.3
NiCu	-689 ± 21	-949 ± 61	-78.3 ± 4.8
NiCuAg	-664 ± 39	-1070 ± 80	-86.3 ± 10.9

4.3.3.3 Faradaic Efficiency

Based on the low, and therefore promising Tafel values for the NiCuAg system in acidic media, the Faradaic efficiency for hydrogen for each of the catalysts in 0.1 M H_2SO_4 was measured. Often the faradaic efficiency is not precisely measured with bubbles on the surface instead being cited.[32] For the Faradaic efficiency calculations each catalyst was subjected to bulk electrolysis for 10 minutes at a current density of -100 mA cm^{-2}. Gas chromoatography was then used to asses the amount of hydrogen produced. The Faradaic efficiencies are shown in Table 4.7

Table 4.7: Faradaic efficiencies for H_2 for all catalysts in 0.1 M H_2SO_4.

Catalyst	Faradaic Efficiency for H_2/%
Ni	90 ± 5.1
NiCu	91 ± 5.1
NiCuAg	85 ± 10.7
NiCuPt	92 ± 2.9
NiPt	93 ± 0.3

It is no surprise that the Pt-containing catalysts gave the highest Faradaic efficiencies. Yet all the catalysts produced adequate Faradaic efficiencies considering that the testing was completed in a single compartment set-up, and the electrolyte was at a fairly low concentration, 0.1 M, compared to those used in industry. Although the Faradaic efficiencies measured here do not significantly differ between the catalysts, the apparent trends are as follows. The Faradaic efficiency is improved upon the addition of the Cu layer to the bare Ni electrode. However, the addition of a Ag layer thereafter does not seem to be beneficial for improving hydrogen evolution activity. The addition of the Pt by galvanic replacement does, however, increase the Faradaic efficiency compared to bare Ni.

4.4 Conclusion

In summary, a 3-layer NiCuPt stack and a 2-layer NiPt stack have been synthesised, characterised and tested as catalysts for the electrochemical evolution of hydrogen in a variety of electrolytes at different pH values. For the 3-layer stack the additional metal layers of copper and platinum were added by electrodeposition and galvanic replacement respectively. For the NiPt catalyst, platinum was added by electrodeposition. Bare Ni, NiCu and NiCuAg were also tested as hydrogen evolution catalysts at a range of pH values.

Analysis of the results of hydrogen evolution testing showed that the NiPt catalyst is the most promising in 0.1 M KOH, with an overpotential at -100 mA cm^{-2} of -102 ± 21 mV and a Tafel slope of -51.8 ± 2.7 mV dec^{-1}. This is understandable as this is the catalyst which contains the highest amount of Pt. Further experimentation would allow for the optimisation of the galvanic replacement of Pt to achieve a higher loading, which would likely improve the performance of the NiCuPt catalyst, whilst reducing the cost compared to pure Pt.

4.5 References

[1] N. S. Lewis and D. G. Nocera, *Proceedings of the National Academy of Sciences*, 2006, **103**, 15729–15735.

[2] N. Dubouis and A. Grimaud, *Chemical Science*, 2019, **10**, 9165–9181.

[3] A. Saeedmanesh, M. A. M. Kinnon and J. Brouwer, *Current Opinion in Electrochemistry*, 2018, **12**, 166–181.

[4] IEA -International Energy Agency, *The Future of Hydrogen*, 2019, `https://www.iea.org/reports/the-future-of-hydrogen`.

[5] IPCC (Core Writing Team), *IPCC, 2023: Climate Change 2023: Synthesis Report. Contribution of Working Groups I, II and III to the Sixth Assessment Report of the Intergovernmental Panel on Climate Change*, 2023.

[6] D. Hauglustaine, F. Paulot, W. Collins, R. Derwent, M. Sand and O. Boucher, *Communications Earth & Environment*, 2022, **3**, 295.

[7] N. Armaroli and V. Balzani, *ChemSusChem*, 2011, **4**, 21–36.

[8] P. Sun, B. Young, A. Elgowainy, Z. Lu, M. Wang, B. Morelli and T. Hawkins, *Environmental Science & Technology*, 2019, **53**, 7103–7113.

[9] G. Kakoulaki, I. Kougias, N. Taylor, F. Dolci, J. Moya and A. Jäger-Waldau, *Energy Conversion and Management*, 2021, **228**, 113649.

[10] E. J. Popczun, J. R. McKone, C. G. Read, A. J. Biacchi, A. M. Wiltrout, N. S. Lewis and R. E. Schaak, *Journal of the American Chemical Society*, 2013, **135**, 9267–9270.

[11] Y. Zheng, Y. Jiao, M. Jaroniec and S. Z. Qiao, *Angewandte Chemie International Edition*, 2015, **54**, 52–65.

[12] B. Conway and B. Tilak, *Electrochimica Acta*, 2002, **47**, 3571–3594.

[13] J. N. Hansen, H. Prats, K. K. Toudahl, N. M. Secher, K. Chan, J. Kibsgaard and I. Chorkendorff, *ACS Energy Letters*, 2021, **6**, 1175–1180.

[14] Z. W. Seh, J. Kibsgaard, C. F. Dickens, I. Chorkendorff, J. K. Nørskov and T. F. Jaramillo, *Science*, 2017, **355**, eaad4998.

[15] J. Verma and S. Goel, *International Journal of Hydrogen Energy*, 2022, **47**, 38964–38982.

[16] J. K. Nørskov, T. Bligaard, A. Logadottir, J. R. Kitchin, J. G. Chen, S. Pandelov and U. Stimming, *Journal of The Electrochemical Society*, 2005, **152**, J23.

[17] S. Trasatti, *Journal of Electroanalytical Chemistry and Interfacial Electrochemistry*, 1972, **39**, 163–184.

[18] S. Anwar, F. Khan, Y. Zhang and A. Djire, *International Journal of Hydrogen Energy*, 2021, **46**, 32284–32317.

[19] Z. Jia, T. Yang, L. Sun, Y. Zhao, W. Li, J. Luan, F. Lyu, L. Zhang, J. J. Kruzic, J. Kai, J. C. Huang, J. Lu and C. T. Liu, *Advanced Materials*, 2020, **32**, 2000385.

[20] N. Lotfi and G. B. Darband, *International Journal of Hydrogen Energy*, 2024, **70**, 301–314.

[21] D. A. Rakov, *Energy Advances*, 2023, **2**, 235–251.

[22] S. Anantharaj, S. Kundu and S. Noda, *Journal of Materials Chemistry A*, 2020, **8**, 4174–4192.

[23] Y. Wang, L. Chen, X. Yu, Y. Wang and G. Zheng, *Advanced Energy Materials*, 2017, **7**, 1601390.

[24] S. Niu, Y. Fang, J. Zhou, J. Cai, Y. Zang, Y. Wu, J. Ye, Y. Xie, Y. Liu, X. Zheng, W. Qu, X. Liu, G. Wang and Y. Qian, *Journal of Materials Chemistry A*, 2019, **7**, 10924–10929.

[25] C. Hu, C. Lv, S. Liu, Y. Shi, J. Song, Z. Zhang, J. Cai and A. Watanabe, *Catalysts*, 2020, **10**, 188.

[26] H. H. Do, N. T. Tran, H. B. Truong and S. Y. Kim, *Journal of The Electrochemical Society*, 2024, **171**, 026501.

[27] V. Vij, S. Sultan, A. M. Harzandi, A. Meena, J. N. Tiwari, W.-G. Lee, T. Yoon and K. S. Kim, *ACS Catalysis*, 2017, **7**, 7196–7225.

[28] L. Huo, C. Jin, K. Jiang, Q. Bao, Z. Hu and J. Chu, *Advanced Energy and Sustainability Research*, 2022, **3**, 2100189.

[29] J. Qi, T. Wu, M. Xu, D. Zhou and Z. Xiao, *Nanomaterials*, 2021, **11**, 1595.

[30] F. Tang, L. Wang, M. D. Walle, A. Mustapha and Y.-N. Liu, *Journal of Catalysis*, 2020, **383**, 172–180.

[31] S. Geng, F. Tian, M. Li, X. Guo, Y. Yu, W. Yang and Y. Hou, *Journal of Materials Chemistry A*, 2021, **9**, 8561–8567.

[32] Y. Ali, V.-T. Nguyen, N.-A. Nguyen, S. Shin and H.-S. Choi, *International Journal of Hydrogen Energy*, 2019, **44**, 8214–8222.

[33] N. Wang, T. Hang, D. Chu and M. Li, *Nano-Micro Letters*, 2015, **7**, 347–352.

[34] D. Goranova, E. Lefterova and R. Rashkov, *International Journal of Hydrogen Energy*, 2017, **42**, 28777–28785.

[35] H. L. S. Santos, P. G. Corradini, M. Medina, J. A. Dias and L. H. Mascaro, *ACS Applied Materials & Interfaces*, 2020, **12**, 17492–17501.

[36] A. Y. Faid, A. O. Barnett, F. Seland and S. Sunde, *Electrochimica Acta*, 2021, **371**, 137837.

[37] K. Skibińska, S. Elsharkawy, D. Kutyła, B. Boryczko, M. M. Marzec and P. Żabiński, *Archives of Civil and Mechanical Engineering*, 2024, **24**, 138.

[38] X. Zou and Y. Zhang, *Chemical Society Reviews*, 2015, **44**, 5148–5180.

[39] I. Roger, M. A. Shipman and M. D. Symes, *Nature Reviews Chemistry*, 2017, **1**, 0003.

[40] H. L. A. Dickinson and M. D. Symes, *Electrochimica Acta*, 2024, **493**, 144355.

[41] D. V. Esposito and J. G. Chen, *Energy & Environmental Science*, 2011, **4**, 3900.

[42] S. Papadimitriou, S. Armyanov, E. Valova, A. Hubin, O. Steenhaut, E. Pavlidou, G. Kokkinidis and S. Sotiropoulos, *The Journal of Physical Chemistry C*, 2010, **114**, 5217–5223.

[43] N. Dimitrova, M. Dhifallah, T. Mineva, T. Boiadjieva-Scherzer, H. Guesmi and J. Georgieva, *RSC Adv.*, 2019, **9**, 2073–2080.

[44] M. Hamze, M. Rezaei and S. H. Tabaian, *Colloids and Surfaces A: Physicochemical and Engineering Aspects*, 2023, **656**, 130422.

[45] A. J. Bard, L. R. Faulkner and H. S. P. o. c. White, *Electrochemical methods: fundamentals and applications*, John Wiley & Sons, Ltd, Hoboken, NJ, USA, Third / Allen J. Bard, Larry R. Faulkner, Henry S. White. edn., 2022.

[46] S.-E. Stanca, O. Vogt, G. Zieger, A. Ihring, J. Dellith, A. Undisz, M. Rettenmayr and H. Schmidt, *Communications Chemistry*, 2021, **4**, 98.

[47] M. Shah, *Scientia Iranica*, 2012, **19**, 964–966.

[48] C. F. Holder and R. E. Schaak, *ACS Nano*, 2019, **13**, 7359–7365.

[49] A. V. Naumkin, A. Kraut-Vass, S. W. Gaarenstroom and C. J. Powell, *NIST X-ray Photoelectron Spectroscopy Database*, `http://dx.doi.org/10.18434/T4T88K`.

[50] C. Wagner, W. Riggs, L. Davis and J. Moulder, *Handbook of X-ray Photoelectron Spectroscopy*, Perkin-Elmer Corporation, 1979.

[51] I. Khalakhan, M. Vorokhta, X. Xie, L. Piliai and I. Matolínová, *Journal of Electron Spectroscopy and Related Phenomena*, 2021, **246**, 147027.

[52] K. Kishi and M. Sasanuma, *Journal of Electron Spectroscopy and Related Phenomena*, 1989, **48**, 421–434.

[53] F. Capece, V. Castro, C. Furlani, G. Mattogno, C. Fragale, M. Gargano and M. Rossi, *Journal of Electron Spectroscopy and Related Phenomena*, 1982, **27**, 119–128.

[54] B. V. Crist, *The XPS Library: Copper Chemical Compounds*, `https://xpsdatabase.net/copper-cu-z29-chemicals/`.

[55] A. N. Mansour, *Surface Science Spectra*, 1994, **3**, 202–210.

[56] H. Xue, Y. Shao, X. Shi, Y. Shao, W. Zhang and Y. Zhu, *Water, Air, & Soil Pollution*, 2022, **233**, 515.

[57] N. Barrett, R. Belkhou, J. Thiele and C. Guillot, *Surface Science*, 1995, **331-333**, 776–781.

[58] H. Li, J.-I. J. Choi, W. Mayr-Schmölzer, C. Weilach, C. Rameshan, F. Mittendorfer, J. Redinger, M. Schmid and G. Rupprechter, *The Journal of Physical Chemistry C*, 2015, **119**, 2462–2470.

[59] G. M. Bancroft, I. Adams, L. L. Coatsworth, C. D. Bennewitz, J. D. Brown and W. D. Westwood, *Analytical Chemistry*, 1975, **47**, 586–588.

[60] S. Jackson, J. Willis, G. Mclellan, G. Webb, M. Keegan, R. Moyes, S. Simpson, P. Wells and R. Whyman, *Journal of Catalysis*, 1993, **139**, 191–206.

[61] Y.-Z. Su, K. Xiao, N. Li, Z.-Q. Liu and S.-Z. Qiao, *Journal of Materials Chemistry A*, 2014, **2**, 13845–13853.

[62] S. Gerhold, M. Riva, Z. Wang, R. Bliem, M. Wagner, J. Osiecki, K. Schulte, M. Schmid and U. Diebold, *The Journal of Physical Chemistry C*, 2015, **119**, 20481–20487.

[63] G. R. Conner, *Journal of Vacuum Science and Technology*, 1978, **15**, 343–347.

[64] K. K. Lian, D. W. Kirk and S. J. Thorpe, *Journal of The Electrochemical Society*, 1995, **142**, 3704–3712.

[65] B. V. Crist, *The XPS Library: Nickel Chemical Compounds*, `https://xpsdatabase.net/nickel-ni-z28-chemicals/`.

[66] J. R. Manders, S. Tsang, M. J. Hartel, T. Lai, S. Chen, C. M. Amb, J. R. Reynolds and F. So, *Advanced Functional Materials*, 2013, **23**, 2993–3001.

[67] A. N. Mansour, *Surface Science Spectra*, 1994, **3**, 221–230.

[68] G. Johansson, J. Hedman, A. Berndtsson, M. Klasson and R. Nilsson, *Journal of Electron Spectroscopy and Related Phenomena*, 1973, **2**, 295–317.

[69] M. Romeo, J. Majerus, P. Legare, N. Castellani and D. Leroy, *Surface Science*, 1990, **238**, 163–168.

[70] K. S. Kim, N. Winograd and R. E. Davis, *Journal of the American Chemical Society*, 1971, **93**, 6296–6297.

[71] Z. Zhou, Z. Pei, L. Wei, S. Zhao, X. Jian and Y. Chen, *Energy & Environmental Science*, 2020, **13**, 3185–3206.

[72] T. Shinagawa and K. Takanabe, *Physical Chemistry Chemical Physics*, 2015, **17**, 15111–15114.

[73] S. Anantharaj and S. Noda, *Materials Today Energy*, 2022, **29**, 101123.

[74] T. Shinagawa, A. T. Garcia-Esparza and K. Takanabe, *Scientific Reports*, 2015, **5**, 13801.

Chapter 5

Conclusions and Future Work

5.1 Conclusions

This thesis investigates the use of layered metal catalysts, referred to as stacks, for sustainable transformations, namely, the electrochemical reduction of carbon dioxide, and hydrogen evolution. Each catalyst developed was thoroughly characterised and tested according to the appropriate performance metrics for each reaction.

The key catalyst stack, NiCuAg, was developed in order to overcome the linear scaling relations typically observed in electrochemical CO_2 reduction. It has been suggested that the fabrication of neighbouring active sites of differing metals could create a synergistic effect, wherein the activity of the metals together is improved compared to the individual metals. The NiCuAg catalyst aimed to take advantage of this as well as a spill-over effect, wherein further reductions can be achieved by passing the reaction intermediates onto different metal active sites, to reduce CO_2 by more than two electrons. It was also thought that optimising an electrochemically synthesised layered system could reduce the strain and reliance on particular precious metals by decreasing the loading required.

A series of layered metal catalysts, bare Ni, NiCu and NiCuAg, were successfully synthesised, characterised, and tested under CO_2 reduction conditions in Chapter 3. The additional metal layers of copper and silver were added by electrodeposition and galvanic replacement, respectively. The results of CO_2 reduction experiments with these stacks showed that bimetallic NiCu and bare Ni both gave higher Faradaic efficiencies towards methanol and ethanol than the synthesised trimetallic NiCuAg stack. Thus, the combination of Ni, Cu and Ag did not show improved activity towards CO_2 reduction by more than two electrons. The coalescence of three individually promising materials does not necessarily lead to improved performance in the resulting ensemble.

One likely reason behind the decreased activity of NiCuAg could be due to the blockage of relevant active sites. Since Ag is known to produce CO at high Faradaic efficiencies, it was expected as a product for this catalyst. However, CO could be blocking the various active sites on the NiCuAg catalyst, this would prevent deeper reduction and limit the amount of CO detected. Site blockage or oxidation state changes could also occur due to contaminants in the electrolyte such as Fe. Another reason for the low activities could be limited access of CO_2 to the electrode, CO_2 is not very soluble in water and thus may not be able to diffuse to the catalyst-electrolyte interface very easily.

Upon testing under CO_2 reduction conditions, a high Faradaic efficiency towards hydrogen was achieved. This led to the characterisation of NiCuAg, and its preceding layered catalysts, as catalysts for hydrogen evolution in Chapter 4. The idea of layered catalysts, and decreasing the metal loading was also expanded to develop NiCuPt, and NiPt. Pt is arguably the best available hydrogen evolution catalyst however its scarcity and price have led to research focused on combining Pt with other metals, thereby decreasing its use. Ni, NiCu, NiCuAg, NiCuPt and NiPt were all tested as catalysts for the electrochemical evolution of hydrogen in a variety of electrolytes at different pH values.

Unsurprisingly, NiPt showed the most promising activity under basic conditions; this is likely because it was the catalyst with the highest Pt loading. Interestingly, a difference in rate determining step was observed between the NiPt and NiCuPt catalysts in 0.1 M KOH. This result was unanticipated as a monolayer of Pt was expected to exhibit Pt-like activity regardless of its synthesis method. However, the difference in Tafel slope was significant enough to suggest a difference in reaction mechanism.

5.2 Future Work

Research into catalysts for sustainable electrochemical transformations remains far from complete. Metallic stacks could yet prove a beneficial structural basis given the correct metal choices and layer thicknesses. Targeted CO_2 reduction by more than two electrons has thus far proven difficult to achieve; development of a high-throughput screening system for tri-metallic combinations could provide a faster way of determining the suitability of certain metal combinations. It could also be worthwhile to test different layering and patterning techniques, perhaps a stepped structure would better aid the spill-over effect. Overall, it is important to focus on the development of optimal active site conditions, whether that be due to beneficial neighbouring atoms or site architectures. The idea of tandem electrocatalysis for transformations with multiple reaction steps appears promising but much research still remains to be done.

The combination of these three metals could be taken onwards and investigated under different forms, for example, the development of a nanoparticle based catalyst using these metals could be beneficial. The use of a nanoparticle system, or perhaps a core-shell design with one layer being bimetallic and the other a single metal, could lead to an increase in suitable active sites for CO_2 reduction. If these metals were to be taken forward, there should be a greater emphasis on which metal facets are exposed to the electrolyte for optimal catalyst-electrolyte interface interactions.

It could be worthwhile to work backwards from the suggested mechanism for a given CO_2 reduction target product. Investigation of the mechanism of a known catalyst by in-situ methods such as Differential Electrochemical Mass Spectrometry or X-ray absorption spectroscopy would allow for catalyst and active site tuning. In this way, beneficial neighbouring site connections could be made and enhanced.

The impact of contaminants from the cell setup and electrolyte would also be worth studying. For the catalysts tested, post-electrolysis catalyst and electrolyte analysis would be worthwhile. The use of Inductively Coupled Plasma Optical Emission spectroscopy before and after the reduction on both the catalysts and electrolyte would enable the investigation into surface degradation and catalyst poisoning. It could also help to identify the merits of electrolyte purification and any pre-electrolysis steps that could benefit the system.

Any further developed catalysts would ideally be tested in a flow cell to eliminate any activity losses due to mass transport or poor CO_2 solubility effects. The detection limits for CO and CH_4 could also be decreased by using a gas chromatograph with He as the carrier gas. This would allow the detector to measure a greater discrepancy in thermal conductivity between the product and carrier gas. The use of an in-line continuous flow GC would also be beneficial for catalyst testing and remove some of the assumptions and error caused by the batch testing method used in this work.

For the hydrogen evolution catalysts in Chapter 4, further optimisation of the Pt coatings is required. Alternative strategies for the galvanic replacement of Pt could be attempted, including the use of an additive or an ultrasonic bath; the submersion time should also be investigated. The idea of adding a small amount of Pt to high activity catalysts should be explored further, in order to determine the extent to which a small amount can benefit the overall system. The apparent changes in rate-determining step, and at what loading of Pt this change occurs in basic conditions should be probed further.

For both of these reactions, it is important to note that all parts of the experimental set-up, including cell design, electrolyte choice, and the catalysts used, should be optimised to reach an industrially viable technology. It is also crucial to assess the long-term stability and cost of these catalysts. Nevertheless, considering the fast-paced developments in this field, it is likely that these sustainable electrochemical transformation technologies will be ready for implementation soon.